



University
of Glasgow

Goura, Germaine Stanislasse Laure (2001) Time marching analysis of flutter using computational fluid dynamics. PhD thesis

<http://theses.gla.ac.uk/6934/>

Copyright and moral rights for this thesis are retained by the author

A copy can be downloaded for personal non-commercial research or study, without prior permission or charge

This thesis cannot be reproduced or quoted extensively from without first obtaining permission in writing from the Author

The content must not be changed in any way or sold commercially in any format or medium without the formal permission of the Author

When referring to this work, full bibliographic details including the author, title, awarding institution and date of the thesis must be given

Time Marching Analysis of Flutter Using Computational Fluid Dynamics

A Dissertation Submitted in Partial Fulfillment of the Requirements for the
Degree of Doctor of Philosophy at the University of Glasgow

by

Germaine Stanislasse Laure Goura
B.A. Mathematiques, Jussieu University, Paris 1996
B.A. Fundamental Physics, Orsay University, Paris 1996
MSc, Dynamics of Fluids and Transfers, Orsay University, Paris 1997.

Computational Fluid Dynamics Group,
Department of Aerospace Engineering

September 2001

Abstract

The maturity of simulation codes for aerodynamics (CFD) and structures (CSD) now leads to high fidelity computations of single discipline problems. The problem of aircraft flutter involves the coupling of aerodynamics and structures and has led to an interest in coupling CFD and CSD codes. There is strong motivation to couple existing codes to simulate this problem to avoid developing new methods since current single discipline methods are both well established and differ in their formulation (Eulerian fluids descriptions based on finite volume methods and Lagrangian finite element methods for structures). Recent work on the sequencing of codes has addressed the time sequencing issue which can be resolved by an iterative scheme to make sure that both simulations advance simultaneously in time. The regeneration of volume grids around a deforming geometry has also received attention.

A third problem involves the passing of loads and displacement information between the fluid and structural surface grids. These grids will not in general coincide and it is likely that they will not even lie on the same surface. This thesis considers this problem and evaluates several existing and proposed solutions from the point of view of geometrical considerations and time marching flutter analysis. The test cases considered are for the AGARD 445.6 wing and the MDO wing. A boundary element formulation is also considered both for the elimination of the transfer problem and also as a transformation method.

A successful evaluation of the influence of the transformation method on the time marching response of a wing in a transonic flow is given and is based on the decomposition of the transformation into two components inwards and outwards of the plane of the structural model's plane.

.....to my family who supported and motivated me.

Acknowledgments

I would like first to thank Professor Richards and Dr Badcock for having enabled me to come to work within their group. Secondly, I am indebted to Mr Mark Woodgate and Dr Badcock for their extreme patience whilst helping with this work as well as the former group members for having laid the foundations for this work. I sincerely thank Prof. Richards, Dr. Badcock, Dr. Barakos and Mr. Woodgate for suggestions on the thesis draft. I thank the faculty for having offered me this scholarship and supporting my applications for several successful travel grants, especially from the Royal Aeronautical Society and the Scottish International Education Trust.

I gratefully acknowledge the assistance of Dr Ray Kolonay for advice on the 445.6 structural model. Dr Reid Melville and Dr Scott Morton provided details of the AGARD 445.6 static case along with data to compare with. Dr Trevor Davies provided insight into the Boundary Element Method. Dr P.C. Chen and Dr Goa Wei advised me on their implementation of the Boundary Element based interpolation method. Anders Karlsson of Saab and Dr Michael Henshaw of BAE SYSTEMS provided the structural model and comparative data for the MDO wing case. Above all, Dr Jonathan Smith (formerly of BAE SYSTEMS and now at FFA) made several valuable contributions for the analysis of the CVT method. I am indebted to them all.

Table of Contents

	Page
Abstract	i
List of Tables	viii
List of Figures	ix
List of Symbols	xii
1 Introduction	1
1.1 Historical Review of Flutter	1
1.2 Linear Analysis Methods	5
1.3 Requirement for Non-linear Methods	7
1.4 Time Marching Analysis of Flutter using a Coupled Simulation	8
1.5 Thesis Originality and Plan	9
2 Formulation	11
2.1 Fluid Model	11
2.1.1 Overview	11
2.1.2 Choice of Model	11
2.1.3 Numerical Method	15
2.1.4 Example of Flow Solutions	17
2.2 Structural Model	19
2.2.1 Linear Elasticity Review	19
2.2.2 Finite Element Model (FEM)	22
2.2.3 Modal Model	23
2.2.4 Boundary Element Method (BEM)	24
2.2.5 Discussion	24
2.3 Time Sequencing of the Models	25
2.3.1 Formulation	25
2.3.2 Results	29
2.4 Conclusions	31
3 Direct Solution by BEM	38
3.1 Overview	38
3.2 Formulation and Implementation	39
3.2.1 Origins	39
3.2.2 The Problem	39
3.2.3 Weighted Residual	40
3.2.4 Fundamental Solution	41
3.3 Implementation	42
3.3.1 Matrix Notation	42
3.3.2 Matrix Form after discretising the boundary	42

3.3.3	Results at Internal Points	44
3.3.4	Integral Calculations	44
3.4	Validation	45
3.4.1	2D Circular Cavity Test	45
3.4.2	Cantilever Beam	46
3.4.3	Conclusion	47
3.5	BEM as a Direct Solver	48
3.6	Conclusion	51
4	Review of interpolation Methods	54
4.1	Overview	54
4.2	Spline Type Methods	55
4.2.1	Infinite Plate Spline	56
4.2.2	Other Spline Based Methods	59
4.3	Weighted Residual Based Methods	64
4.3.1	Method of Chen	64
4.3.2	Methods of Lohner and Cebal	67
5	Analysis of Transfer Methods	70
5.1	Transformation Methods	70
5.1.1	The Constant Volume Tetrahedron Transformation	70
5.1.2	Spline Based Transformation Methods	74
5.2	Translational and Rotational Shape Preservation	75
5.2.1	Translation	76
5.2.2	Rotation	76
5.3	Forces	79
5.4	Representation of Structural Behaviour	80
5.5	Evaluation of CVT and IPS	81
5.6	Evaluation of CVT and BEM-based Transformation	85
5.7	Conclusions	91
6	Time Marching Analysis	94
6.1	Overview	94
6.2	Description and Review of Wing Flutter Test Cases	95
6.2.1	AGARD 445.6 Wing	95
6.2.2	MDO Wing	101
6.3	445.6 Results	105
6.3.1	Grids and Numerical Tests	105
6.3.2	Interpolated Mode Shapes	106
6.3.3	Static Case	110
6.3.4	Numerical Tests for Dynamic Cases	115
6.4	MDO Wing	124
6.4.1	Grids and Numerical Tests	124
6.4.2	Interpolated Mode Shapes	126
6.4.3	Static Cases	129
6.4.4	Dynamic Cases	134
6.5	Conclusions	141
7	Conclusion	143
7.1	Objectives	143
7.2	Lessons Learned	144
7.3	Future Work	146
A	Summary of BEM Theory	147

A.1	Summary of the Weighted residual method	147
A.2	Boundary integral from weighted residual statement	148
A.3	Fundamental Solutions	148
	Bibliography	150

List of Tables

Table	Page
2.1 summary of time step refinement	31
3.1 Circular cavity internal point displacements. All distances are in inches. 46	
6.1 Transformation Methods Evaluated in this chapter together with plotting colours used	95
6.2 Summary of numerical details for single flutter calculation. N/A indicates that the information was not included in the reference. Here, steps per cycle refers to the first bending mode and the time step is non-dimensionalised with respect to the freestream velocity and the root chord.	101
6.3 Summary of flutter speed predictions and measurements for AGARD 445.6 wing. N/A indicates that the information was not included in the reference.	101
6.4 Measured [61] and computed modal frequencies in Hertz for AGARD 445.6 wing.	102
6.5 Conditions for MDO test case. The lift coefficient quoted here is scaled in terms of the wing surface area,	105
6.6 Tip Deflection in inches for static aeroelastic deformation of AGARD 445.6 wing at a Mach number of 0.8 and an incidence of 1 degree. . .	111
6.7 Trimmed conditions for MDO wing. Note that the lift coefficient is based on an area given by the root chord squared and the angle of attack α is given in degrees.	130
A.1 Fundamental solutions of elasticity.	149

List of Figures

Figure	Page
2.1 C-O grid for F5 test case.	18
2.2 F5 test case convergence history. $M_\infty = 0.896$, $\alpha = 0.497^\circ$	19
2.3 F5 test case pressure distributions. $M_\infty = 0.896$, $\alpha = 0.497^\circ$. The solid dots are the experimental measurements on the lower surface and the unfilled dots are from the upper surface.	20
2.4 F5 test case pressure contours. $M_\infty = 0.896$, $\alpha = 0.497^\circ$	21
2.5 Comparison between computed and experimental data for mean, real and imaginary pressure coefficients for the rigid pitching F5 wing case.	32
2.6 Convergence of maximum moment coefficient for forced pitching.	33
2.7 Behaviour for varying \bar{U}	34
2.8 Time Convergence for $\bar{U} = 1.9$	35
2.9 Time Convergence for $\bar{U} = 1.9$	36
2.10 Comparison of aerofoil response using a constant time step $\Delta t = 0.02$ and a variable time step with $\Delta t_{max} = 0.16$	36
2.11 Coupling comparison for $\bar{U} = 1.9$	37
3.1 Cantilevered Beam Using Constant Elements	46
3.2 Cantilevered Beam Using Linear Elements	47
3.3 Grid for NACA4412 aerofoil.	51
3.4 Pressure contours for NACA4412 aerofoil at $M_\infty = 0.6$ and $\alpha = 6^\circ$	52
3.5 Normal deflections for NACA4412 aerofoil on the fine (i.e. derived from CFD) and coarse meshes.	53
4.1 Inverse Isoparametric Element	62
4.2 Structural BEM problem	65
4.3 Virtual BEM method	67
4.4 Pressure interpolation	68
5.1 Interpolation from structural mesh to fluid mesh.	71
5.2 Rigidly rotated circle - solid line is interpolated fluid grid points by IPS, crosses are structural grid used for transformation, circles are exactly rotated fluid points.	82
5.3 Rigidly rotated circle - L2 norm of the difference between the rigidly rotated fluid positions and the interpolated positions by IPS for different rotation angles	83

5.4	Rigidly rotated aerofoil - solid line is interpolated fluid grid by IPS, crosses are structural grid used for transformation, circles are exactly rotated fluid points.	84
5.5	Rigidly rotated aerofoil - L2 norm of the difference between the rigidly rotated fluid positions and the interpolated positions by IPS for different rotation angles	85
5.6	Bending beam - solid line is interpolated fluid grid, crosses are structural grid used for interpolation, circles are FE solution from MSC/NASTRAN.	86
5.7	Upper half of stretching beam - solid line is interpolated fluid grid, crosses are structural grid used for interpolation, circles are FE solution from MSC/NASTRAN.	87
5.8	Initial Solid and Fluid Surfaces	88
5.9	Torsion Node Line Pattern Comparisons for Curved Surface	89
5.10	Aerofoil rigid motion original BEM method	90
5.11	Aerofoil rigid motion with Modified BEM method	90
5.12	Circle rigid motion with Virtual BEM	91
5.13	Circle rigid motion with Virtual BEM	92
5.14	Beam under large bending	93
6.1	445.6 wing planform. The dark shaded area indicates the extent of the grid for a reduced plate structural model used for some tests. . .	96
6.2	First four modes from FE model of 445.6 wing.	100
6.3	MDO wing planform. The dark shaded region indicates the extent of the structural model.	103
6.4	MDO mode shapes.	104
6.5	445.6 rigid wing steady test case convergence history. $M_\infty = 1.141$, $\alpha = 0^\circ$	107
6.6	445.6 rigid steady test case pressure distributions compared with the results from [68]. $M_\infty = 1.141$, $\alpha = 0^\circ$	108
6.7	445.6 rigid steady test case pressure contours. $M_\infty = 1.141$, $\alpha = 0^\circ$	109
6.8	Transformed mode shapes at 75 % span	111
6.9	Transformed mode shapes for the 445.6 wing in the region of the leading edge at 75 % span. The profile marked with squares is obtained using IPS on the full span grid and is almost indistinguishable from that obtained using the linear transformation on both the full span and reduced span grids. The profile which is unmarked with squares is obtained using IPS on the reduced span grid.	112
6.10	Aerofoil profile for first grid point inboard of tip for aerostatic 445.6 wing test case. $M_\infty = 0.8$, $\alpha = 1^\circ$	113
6.11	445.6 aerostatic test case convergence history. $M_\infty = 0.8$, $\alpha = 1^\circ$	114
6.12	Time convergence for aeroelastic dynamic case at $M_\infty = 0.96$, $\rho_\infty = 0.08\text{kg}/\text{m}^3$, $U_\infty = 308.20\text{m}/\text{s}$	118
6.13	Grid convergence for aeroelastic dynamic response at $M_\infty = 0.96$, $\rho_\infty = 0.08\text{kg}/\text{m}^3$, $U_\infty = 308.20\text{m}/\text{s}$	119
6.14	Time marching responses at Mach 0.678 for two values of density.	120

6.15	Time marching responses at Mach 0.901 for two values of density. . .	121
6.16	Time marching responses at Mach 0.960 for two values of density. . .	122
6.17	Time marching responses at Mach 1.141 for two values of density. . .	123
6.18	Comparison of predictions and measurements of 445.6 flutter boundary.	125
6.19	Comparison of pressure coefficient difference for flow around the rigid 445.6 wing at $M_\infty = 0.96$ and $\alpha = 1.0^\circ$ computed from the Euler and potential models.	126
6.20	Comparison of pressure coefficient at 20, 40, 60 and 80 % span for the MDO wing with $M_\infty = 0.88$ and $\alpha = 1^\circ$. The lines are the coarse grid result and the symbols the fine grid result.	127
6.21	Comparison of transformed mode 5 for MDO wing.	129
6.22	Aerostatic comparisons for case 1 for trimmed conditions.	131
6.23	Aerostatic comparisons for case 2 for trimmed conditions.	132
6.24	Aerostatic comparisons for case 3 for trimmed conditions.	133
6.25	Convergence history for case 1 using linear transformation.	135
6.26	Comparisons of modal time histories for case 3 using linear transfor- mation and various time stepping parameters.	136
6.27	Comparisons of modal time histories for cases 2 and 3 using regener- ated CVT and EURANUS results.	138
6.28	Comparisons of modal time histories for cases 2 and 3 using different transformation methods.	139
6.29	Comparisons of modal time histories for 445.6 wing at $M=0.901$, $\rho =$ $0.1kg/m^3$, using a full and reduced plate structural model. Note that the standard colour coding has not been used in this figure.	140

List of Symbols

Notation for grid points

- $\mathbf{x}_{\xi,i}$ $\mathbf{x}_{\xi,i} = [x_{\xi,i}, y_{\xi,i}, z_{\xi,i}]^T$ is the location of the i th grid point on the grid ξ where
- $\xi = a$ is the aerodynamic grid
 - $\xi = s$ is the structural grid
 - $\xi = p$ is the projected grid
 - $\xi = v$ is the virtual grid
- $\tilde{\mathbf{x}}_{\xi}$ $\tilde{\mathbf{x}}_{\xi} = [x_{\xi,1}, x_{\xi,2}, \dots, x_{\xi,N}]^T$ is the vector containing x-coordinates of grid points of type ξ
- $\tilde{\mathbf{y}}_{\xi}$ $\tilde{\mathbf{y}}_{\xi} = [y_{\xi,1}, y_{\xi,2}, \dots, y_{\xi,N}]^T$ is the vector containing y-coordinates of grid points of type ξ
- $\tilde{\mathbf{z}}_{\xi}$ $\tilde{\mathbf{z}}_{\xi} = [z_{\xi,1}, z_{\xi,2}, \dots, z_{\xi,N}]^T$ is the vector containing z-coordinates of grid points of type ξ
- $\hat{\mathbf{x}}_{\xi}$ $\hat{\mathbf{x}}_{\xi} = [x_{\xi,1}, y_{\xi,1}, z_{\xi,1}, \dots, x_{\xi,N}, y_{\xi,N}, z_{\xi,N}]^T$ is the vector containing x,y and z coordinates of grid points of type ξ

General Notation

- a speed of sound
- \mathbf{A} coefficient matrix of $\mathbf{x}_{s,i}$ in the linearised CVT
- α_i i th modal generalised coordinates
- α angle of attack
- \mathbf{b} $\mathbf{b} = [b_x, b_y, b_z]^T$ is the body force vector
- \mathbf{B} coefficient matrix of $\mathbf{x}_{s,j}$ in the linearised CVT
- \mathcal{B} matrix relating points on the fluid and virtual BEM meshes
- \mathbf{c}^i BEM coefficient matrix
- \mathbf{C} coefficient matrix of $\mathbf{x}_{s,k}$ in the linearised CVT
- \mathcal{C} matrix relating points on the structural and virtual BEM meshes
- C_L Lift coefficient
- C_M Moment coefficient

C_p	pressure coefficient
\mathbf{d}, \mathbf{d}_0	out-of-plane component of an aerodynamic point, the subscript 0 indicates this is constant
\mathcal{D}	matrix used to prove rotational invariance for CVT
D	coefficient of plate flexibility
D	damping matrix
D_{hh}	modal damping matrix
\mathcal{D}_r	rigidity coefficient matrix
E	specific energy of fluid
\mathcal{E}	strain energy
ϵ	strain tensor
ϵ	BEM error
F	objective function for Chen method minimisation
\mathbf{F}^i	convective flux vector in the x-direction
$\mathbf{f}_{i,\xi}$	forces at <i>ith</i> grid point of type ξ
$\hat{\mathbf{f}}_\xi$	forces at $\hat{\mathbf{x}}_\xi$
\mathcal{F}_i	coefficient scaling thin plate fundamental solution centred on a structural point \mathbf{x}_i
Γ_1	part of boundary to domain Γ on which the displacement is known
Γ_2	part of boundary to domain Γ on which the traction is known
$\Gamma, \partial\Gamma$	flow domain and its boundary
g	structural damping
\mathbf{G}^i	convective flux vector in the y-direction
\mathbf{G}	BEM matrix
$\bar{\mathbf{G}}$	BEM matrix
\mathbf{G}_{bi}	BEM matrix
\mathcal{G}	function denoting updated solution by Runge-Kutta method

h	plunge, scaled by the semi-chord
\mathbf{H}^i	convective flux vector in the z -direction
\mathbf{H}	BEM matrix
\mathbf{H}_{bi}	BEM matrix
$\bar{\mathbf{H}}$	BEM matrix
\mathbf{I}	Identity matrix
k	reduced frequency
κ	shape parameter for Multiquadratic Biharmonic spline
K_i	thin plate fundamental solution centred on a structural point \mathbf{x}_i
$K_{i,j}^\xi$	K_j evaluated at the i th point on the grid ξ
\mathbf{K}	stiffness matrix
\mathbf{K}_{hh}	modal stiffness matrix
λ	vector of Lagrange multipliers
\mathbf{m}	aerodynamic moment about a structural point
M_∞	freestream Mach number
\mathbf{M}	mass matrix
\mathbf{M}_{hh}	modal mass, damping, stiffness and aerodynamic matrices
μ	ratio of the aerofoil mass to the fluid mass
\mathbf{n}	outward normal vector on the boundary
$\mathcal{N}_1, \mathcal{N}_2$	Linear shape functions
ω	rotation vector
ω_α	natural frequency of pitching
ω_h	natural frequency of plunging
ω_R	$\omega_R = \omega_h / \omega_\alpha$
Φ	flow potential function
ϕ_i	i th mode shape
p	pressure

\mathbf{p}	traction vector $\mathbf{p} = [p_x, p_y, p_z]^T$
$\bar{\mathbf{p}}$	known traction vector on boundary
\mathbf{p}^*	fundamental traction vector
\mathbf{P}^*	fundamental solution traction vector gradient matrix
\mathbf{p}_{approx}	approximate traction vector
Ψ_a, Ψ_s	matrices relating aerodynamic and structural points to virtual surface points for finite plate spline
q_l	distributed load on plate
\mathbf{q}	$\mathbf{q} = [\alpha, h, \dot{\alpha}, \dot{h}]^T$ is the vector of unknowns for pitch-plunge aerofoil
\mathbf{Q}_{hh}	modal aerodynamic matrix
r_α	radius of gyration
r_i	radial distance from i th grid point
ρ_∞	freestream density
$\mathbf{S}, \tilde{\mathbf{S}}, \hat{\mathbf{S}}$	spline matrices
\mathbf{S}	matrix used to prove rotational invariance for CVT
σ	stress tensor
θ	rotation angle
Θ	angle of rotation axis to y axis
\mathbf{T}	skew symmetric transformation matrix
\mathbf{u}	structural displacement $\mathbf{u} = [u_x, u_y, u_z]^T$
$\bar{\mathbf{u}}$	known structural displacement on boundary
\mathbf{u}^*	fundamental solution for structural displacement
\mathbf{U}^*	fundamental solution displacement gradient matrix
U^*	Cartesian velocity x-component relative to a moving frame
\mathbf{u}_{approx}	approximate solution for structural displacement
\mathcal{U}	matrix used to prove rotational invariance for CVT

\bar{U}	$\bar{U} = 4b/(V_\infty \omega_R)$
\mathbf{v}	$\mathbf{v} = [u, v, w]^T$ is the velocity vector in a Cartesian frame of reference
\mathcal{V}	matrix used to prove rotational invariance for CVT
V_i	volume in <i>ith</i> cell
V_∞	freestream speed
V^*	Cartesian velocity x-component relative to a moving frame
\mathbf{w}	conserved fluid variables
$\bar{\mathbf{w}}_i$	conserved fluid variables in <i>ith</i> cell multiplied by V_i
W^*	Cartesian velocity x-component relative to a moving frame
x_α	offset between centre of gravity and the elastic axis for an aerofoil
Ξ	angle of rotation axis to z axis
x_t	x-velocity components of a moving frame
y_t	y-velocity components of a moving frame
z_t	z-velocity components of a moving frame
ζ	complex variable

Chapter 1 : Introduction

... Could we not solve all our aeroelastic problems in one fell swoop by treating the dynamics of a deformable aircraft ? In theory this was certainly possible, but the complexity of the problem ruled this out in practice. There was, however, a ray of hope that automatic calculating machines and electronic devices were being studied and offered the possibility of enormous advances on the capabilities of the machines of today

A.R. COLLAR, *Aeroelasticity- Retrospect and Prospect.*

The Journal of the Royal Aeronautical Society, Jan. 1959, Vol.63, number 557, p.4

1.1 Historical Review of Flutter

Collar[1] foresaw, 42 years ago, that computers would make a significant impact on the study of aeroelastic problems. No flying vehicle is perfectly rigid, and its flexibility can interact with the flow around it to create self-sustaining vibrations. Flutter is a self-excited oscillation in which energy is absorbed by the body from the airstream. The simulation of this problem is the subject of this thesis. An historical review of flutter is presented in the following paragraphs.

The first major study on flutter, according to Garrick and Reed's historical review on aircraft flutter [3], was made by F. W. Lanchester during World War I for the Handley Page 0/400 biplane bomber which experienced violent antisymmetric

oscillations of the fuselage and tail. It was said that Lanchester's report[4] recognised two important points :

- that the oscillations were not the result of resonance induced by vibratory sources but were self-excited
- and that an increase in the structural stiffness could eliminate the problem.

Tail flutter resulting in pilot fatalities was experienced only one year later by the de Havilland DH-9 airplane, as mentioned by Garrick and Reed[3] .

In the review [3], the period from 1918 to the 1930's featured a systematic study of the van Berkel monoplane, a seaplane for reconnaissance(Baumhauer and Koning[5]). The flutter problem consisted of a vertical bending of the wing combined with the motion of the ailerons. It was argued that a mass balance of the aileron could eliminate the problem, and thus the idea of decoupling interacting modes was introduced. The same kind of flutter origin was also investigated in the UK for the Gloster Grebe and Gloster Gamecock biplanes. It was found that moving the aileron to balance the wing mass solved the problem.

The review then asserts that due to the increase in aircraft speed and the use of new structures, the importance of flutter increased during the World War II. In 1945 in Germany, 146 flutter incidents took place of which 24 resulted in crashes [3]. All of these incidents involved flutter of the control surfaces or of the auxiliary controls. During the 10 years following the second war there was a major drop in the number of flutter incidents. A total of 54 flutter incidents were recorded and documented. As foreseen by Collar[1] this was made possible by computational methods which complemented improvements in experimental techniques for flutter models, ground resonance testing and flight flutter testing. These computational methods were all based on linear aerodynamic and structural models. The equations of motion for

the structure can then be transformed to the frequency domain and the analysis then examines the damping characteristics there. By contrast, the full nonlinear equations, with the nonlinearity resulting from the flow or the structure, must currently be integrated forward in time to examine stability properties. Theodor Theodorsen's work [6] on two-dimensional flutter theory led in the 1950's to the vg flutter analysis method. The decline in the number of flutter incidents continued between 1960 and 1972 when seven mild flutter incidents are recorded. But as explained by Kaynes [7], an exception to the reduction of accidents arose in the UK in 1990 when the Shorts Tucano aircraft experienced vibrations in a flight test. This was due to the presence of stores on the wing which modified the flutter characteristics of the aircraft, and which were not predicted by linear aeroelastic methods[7].

Most flutter problems arising with modern aircraft are of the Limit Cycle Oscillation (LCO) type. Usually for a classical flutter there is a value of a system parameter such as air speed or altitude at which the stability of the system changes to an oscillation with growing amplitude until structural failure. In the case of an LCO, above the onset of flutter the oscillations remain limited and sustained, and might not be destructive. However, from a practical point of view, these oscillations can be extremely uncomfortable for the pilot, and in the case of fighter aircraft, the precision of the air-to-air missile systems can be reduced. In addition they can increase fatigue. Much of the recent work on flutter attempts to characterise the limit cycle oscillation (LCO) within the flight envelope and to modify the flight control systems to minimize the effect on aircraft such as F16 and F/A 18.

Most of the recent incidents concerning LCO's have been associated with externally mounted stores, although this behaviour is still to be explained. According to the review given in reference [7], unexpected instability arose for the Mitsubishi

F-2A/B fighter in 1999. These vibrations delayed the program for at 9 months¹. The problem was linked to the presence of stores. Stores integration was also responsible for a 30% reduction in the flight envelope for RAAF F-18². In 1998, the American military aircraft F/A-18E/F Super Hornet showed vibrations during flight tests. At stake was the production of 222 aircraft with a value of 40 billion dollars. The US navy was confident that the problem could be overcome by modifying the wing structure. However, this solution led to the appearance of other aeroelastic phenomena. The money was ready to be released as long as the vibration problems were solved. In June 2000, it was said that the US General Accounting Office (GAO) would like to delay the full-rate production due to the discovery of potentially damaging noise and vibration problems. The vibration problems can cause damage to air-to-air and air-to-ground weapons carried aboard the aircraft. The GAO reported that Congress should tell the Navy to defer production in order to avoid costly retrofitting. The Northrop Grumman USAF B-2 Bomber was designed using a linear aeroelastic code. However, during flight testing at higher subsonic Mach numbers, nonlinear aeroelastic pitch oscillations arose that were not predicted by linear models. Using a Navier-Stokes code it was shown that these phenomena were predictable [8], and that they arose from strong shock induced oscillations.

Today there are few catastrophic flutter incidents due to modern testing techniques and regulatory safety margins. However, theoretical prediction methods are unsatisfactory in a number of respects which will be discussed below. As illustrated by the examples cited above, there are still regularly arising flutter problems which, although rarely fatal, can delay projects and incur substantial additional costs to fix. In addition, flight testing is still done with heightened caution due to the lack of confi-

¹Flight magazine, 16th June 1999, p.27

²Flight magazine, 10th October 2000, p 23

dence in theoretical predictions in the transonic range. This again causes substantial additional cost. Therefore, there is considerable motivation of a practical, scientific and monetary kind to advance the understanding and prediction of aeroelastic effects.

1.2 Linear Analysis Methods

The most widely used method for flutter certification is linear, and is available in the commercial package in MSC/NASTRAN among others. This method relies on a potential flow solver which is based on linearized aerodynamic potential theory where the undisturbed flow is supposed uniform or varying harmonically. The wing is modelled by panels, and the lifting surfaces are supposed to be nearly parallel to the flow. For the supersonic range, supersonic lifting surface theory is usually employed. The structure is modelled as modes, and the spatial interfacing uses spline methods such as the Infinite Plate Spline described in detail later.

For the classical approach the problem can be written as

$$\mathbf{M}\delta\ddot{\mathbf{x}}_s + \mathbf{D}\delta\dot{\mathbf{x}}_s + \mathbf{K}\delta\mathbf{x}_s = \mathbf{L}(\delta\mathbf{x}_s, \delta\dot{\mathbf{x}}_s) \quad (1.1)$$

where \mathbf{M} , \mathbf{D} and \mathbf{K} are the structural mass, damping and stiffness matrices, $\delta\mathbf{x}_s$ is the wing deflection on a grid of points \mathbf{x}_s and \mathbf{L} indicates the aerodynamic loads. The flutter analysis is done in the frequency domain. The first hypothesis is that the damping is proportional to the stiffness

$$\mathbf{M}\delta\mathbf{x}_s + \mathbf{K}(1 + ig)\delta\mathbf{x}_s = \mathbf{L}(\delta\mathbf{x}_s, \delta\dot{\mathbf{x}}_s) \quad (1.2)$$

and then that the structural motion is supposed harmonic

$$\delta\mathbf{x}_s = \delta\mathbf{x}_{sk}e^{st} \quad (1.3)$$

where the real part of s determines the stability (positive is unstable, negative is stable). The aerodynamic loads \mathbf{L} are computed using linear aerodynamics and are

linearly related to the deflections through the so called Aerodynamic Influence Coefficient matrix.

Usually equation (1.2) is expressed in modal coordinates as

$$[-\mathbf{M}_{hh}s^2 + i\mathbf{D}_{hh}s + (1 + ig)\mathbf{K}_{hh} - (\frac{1}{2}\rho V_\infty^2)L_{kk}(M_\infty, k)]\delta\mathbf{x}_{sk} = \mathbf{0}. \quad (1.4)$$

where \mathbf{M}_{hh} , \mathbf{D}_{hh} , \mathbf{K}_{hh} and \mathbf{L}_{hh} refer to the modal mass matrix, damping matrix, stiffness matrix and aerodynamic matrix respectively. To solve the system, the unsteady aerodynamic forces are supposed to be oscillatory with a reduced frequency of k at Mach number M_∞ . Here ρ refers to the fluid density, g to an artificial damping and V_∞ the fluid velocity.

From this last equation, several types of method have been developed to solve the system, including the Vg, pk and determinant based methods[9]. For the Vg method, also called the k method in MSC/NASTRAN, s is supposed to be purely imaginary. This leads to an eigenvalue problem for (M_∞, k, ρ) . The flutter velocity is calculated where no additional damping is required to force the motion to be oscillatory ($g = 0$).

The pk method does not make the hypothesis that s is purely imaginary and is also implemented in MSC/NASTRAN [71]. The methodology used to determine the flutter boundary is also based on a complex eigenvalue analysis. This supposes that the structure is at the flutter boundary or is varying harmonically on one of its modes. The modal equation leads to the problem of finding the frequency at which the system flutters, and corresponds in practice to determining (M_∞, k, ρ) for which the structural frequency s corresponds to the reduced frequency k . This method requires special iteration techniques.

The determinant based method, or P method, assumes that the aerodynamic matrix is a rational function of the displacements. The determinant of the system is then calculated for increased frequencies at constant altitudes and velocities. The

real part of the determinant is plotted against its imaginary part. These graphs are then interpreted to determine the stability position.

1.3 Requirement for Non-linear Methods

Due to the development of new types of aircraft, flutter studies based on classic methods fail to predict accurately the aeroelastic behaviour. There are a number of examples and reasons for this.

There has been a growing interest in High Altitude, Long Endurance (HALE) aircraft in recent years. These aircraft are being considered for unmanned reconnaissance missions, long term surveillance, environmental sensing and also for communication relay. Such aircraft have slender wings (aspect ratio or the order of 35), which are highly flexible. Large deflections can result, reaching about 25 percent of wing semispan. Linear theory fails to accurately analyse such aeroelastic deformations. An example of this is the aircraft called strato2C [10]. This high altitude aircraft is intended for manned stratospheric research missions up to 80000 ft. Aeroelastic investigations are important and a critical requirement is low empty weight. Linear theory failed to give accurate estimates of the speeds at which aeroelastic instabilities occur due to the large scale deflections experienced.

A number of examples of limit cycle oscillation (LCO) were cited above. There is ongoing debate about the origins of these but current thinking is that they are due to either shock wave motions or flow separation. In either case the linear aerodynamic theory can not predict these effects. Also, in the transonic range the linear aerodynamic theory is clearly not adequate. The techniques currently used to overcome this problem involve crude attempts at scaling the Aerodynamic Influence Coefficient matrix which relates the fluid forces to the structural displacements. Safety margins

have been sufficient to avoid problems with this approach but this is clearly not satisfactory. Given that computational techniques now allow the realistic representation of aerodynamics over complete aircraft, settling for linear aerodynamics as the basis of aeroelastic analysis seems unnecessarily restrictive and risky.

This having been said, it is noted that the limitations of current techniques are well understood, even if only at an intuitive level, by aircraft designers. The development of new tools is at an early stage and has a large problem in gaining enough credibility to be used in practice. The current work should be seen in this context.

1.4 Time Marching Analysis of Flutter using a Coupled Simulation

Because of the maturity of flow and structural solvers, it makes sense to bring together these two areas in order to simulate aeroelastic problems. The characteristics of fluid and structural systems make developing a single monolithic code difficult, with the exception of the approach developed in reference [2] which however places numerical restrictions on the efficiency of the solver arising from numerical stability. With the advances in numerical methods for CFD which permit accurate aerodynamic predictions on rigid wing geometries, and the availability of a well established finite element method, for the prediction of structure deformations, it appears natural to couple the two well established methods in order to simulate fluid-structure interactions. In this approach the coupling between the two codes is crucial, because the aeroelastic solver accuracy will be limited by the coupling accuracy.

So the problem we consider is, having two accurate codes, how can they be put together to create an accurate aeroelastic simulation? The question of time coupling has been extensively investigated in the literature. The issue of spatial coupling is less well researched and forms the major problem investigated in this thesis.

It is clear that solutions to the Euler equations depend on the aerodynamic shape. Calculations were made using different wing tips in reference [11]. The first study was on the influence of geometric modifications of a wing in steady flow. It was shown that static structural deformations could significantly change the values of the pressure coefficient distribution. Comparisons of wing tip effects on a flexible aircraft show that shock positions vary depending on the wing tip model. It is therefore essential not to introduce distortions into the aerodynamic profile due to the way that information on the deformation is passed from the structural model.

Various methods have been proposed for the spatial coupling. The first were based on panel structural and aerodynamic models, and so consist mainly of in-plane interpolation as in the infinite plane spline. However, with the necessity to use accurate aerodynamic solvers such as the Euler equations, the extrapolation of the structural displacements to the fluid interface, which now is no longer a simple panel, becomes important. There has been very little systematic study of this problem in the literature. A review of coupling methods is given in a separate chapter below.

1.5 Thesis Originality and Plan

The original aim of this work was to couple the Glasgow University flow code PMB with a modal structural solver for aeroelastic simulations. Initial effort focussed on the time sequencing for aerofoil problems and is described in section 2.3. The focus for three dimensional problems then shifted to the spatial coupling and two approaches were considered. First, the use of a BEM solver to eliminate the coupling problem by forcing the fluid and structural surface meshes to co-incide was considered and put under doubts for wing aeroelasticity (section 3.5). Secondly, after consideration of the performance of other coupling methods a new method, the Constant Volume Trans-

formation(CVT) was proposed to transform data between the fluid and structural grids. This technique is considered and critically reviewed for two wing test cases and a good understanding of the influence of the coupling method on the response obtained is built up. Hence, the original objectives of the work have been met.

Several publications have arisen from the work: journal papers on geometrical aspects of the spatial coupling [13] and time marching flutter test cases [12]; conference papers on the time sequencing [33], CVT transformation [34] and analysis of the CVT transformation[58].

The thesis is organised as follows. The general formulation is first described in Chapter 2. In the same chapter, the flow solver, structural solver and time sequencing are described together with indicative results for rigid wings and moving aerofoils.

Next the boundary element method is described in Chapter 3 as a possible direct structural solver and also as the basis for a coupling method.

Coupling methods are reviewed in Chapter 4 and their deficiencies are highlighted.

The CVT transformation for coupling is proposed in Chapter 5 and its theoretical and geometrical performance are considered.

The influence of the coupling method is illustrated in Chapter 6 where several coupling methods are compared for static and dynamic aeroelastic response for two wings.

Finally, conclusions are presented in Chapter 7.

Chapter 2 : Formulation

2.1 Fluid Model

2.1.1 Overview

With the advent of computational methods, it became possible to predict flow behaviour using nonlinear flow models in complex geometries. It is tempting for an aeroelastic calculation to use the highest aerodynamic model, the Navier-Stokes model. However, the effort needed to obtain a solution might not be justified if a computationally cheaper model could give realistic results. A summary of the available aerodynamic models is first presented before justifying why the Euler equations are chosen as part of our aeroelastic simulations.

2.1.2 Choice of Model

The Potential Models

The potential flow model is an inviscid flow description which starts by supposing that the flow is irrotational, so that a velocity potential function can be defined.

The full potential equation makes the hypothesis that the flow is irrotational and inviscid, but takes into account compressibility. If the potential function is denoted Φ , the density by ρ and the velocity by \mathbf{v} , with $\mathbf{v} = \nabla\Phi$, ensuring mass continuity leads to the equation

$$\frac{\partial\rho}{\partial t} + \frac{\partial(\rho\Phi_x)}{\partial x} + \frac{\partial(\rho\Phi_y)}{\partial y} + \frac{\partial(\rho\Phi_z)}{\partial z} = 0. \quad (2.1)$$

This is an equation with two unknowns Φ and ρ . Another relation between these two variables is needed to close the problem.

In order to obtain an equation for the density the momentum equation is used along with the hypothesis that the fluid is barotropic (eg the density is only a function of the pressure). This leads to the unsteady Bernoulli's equation

$$\frac{\partial \Phi}{\partial t} + \int \frac{dp}{\rho} + \frac{v^2}{2} = C(t) \quad (2.2)$$

Using the hypothesis that the flow is isentropic $p \propto \rho^\gamma$ and the definition of the speed of sound $a^2 = \gamma p / \rho$, the Bernoulli equation becomes

$$\frac{\partial \Phi}{\partial t} + \frac{a^2}{\gamma - 1} + \frac{v^2}{2} = \frac{a_\infty^2}{\gamma - 1} + \frac{V_\infty^2}{2}. \quad (2.3)$$

Finally, using the isentropic pressure density relation and the speed of sound, one obtains

$$\rho = [1 + \frac{\gamma - 1}{2}(M_\infty^2 - 2\Phi_t - \Phi_x^2 - \Phi_y^2 - \Phi_z^2)]^{\frac{1}{\gamma - 1}}. \quad (2.4)$$

Equations (2.1) and (2.4) form a closed system. This model is only realistic if the flow contains weak shocks which produce a small change in entropy.

By supposing that the products of the time varying contributions to Φ and ρ are small compared to mean terms, one can obtain the transonic small disturbance (TSD) equation. Define $\Phi = \Phi_0 + \Phi'$ and then

$$(1 - M_\infty^2 - M_\infty^2[(\gamma + 1)\frac{\Phi'_x}{U_\infty} + (\gamma - 1)\frac{\Phi'_t}{U_\infty^2}])\Phi'_{xx} + \Phi'_{yy} + \Phi'_{zz} = \frac{1}{a_\infty^2}[\Phi'_{tt} + 2U_\infty\Phi'_{xt}] \quad (2.5)$$

We drop the prime from now on and assume that we are calculating the perturbed part of the potential. The density equation is given by

$$\rho = \rho_\infty[1 - M_\infty^2(\frac{1}{U_\infty^2} + \frac{\Phi_t}{U_\infty^2})]. \quad (2.6)$$

In the subsonic or supersonic range the TSD equation can be further simplified by neglecting the nonlinear terms to give

$$(1 - M_\infty^2)\Phi_{xx} + \Phi_{yy} + \Phi_{zz} = \frac{1}{a_\infty^2}[\Phi_{tt} + 2U_\infty\Phi_{xt}] \quad (2.7)$$

Considering the steady condition leads to the Prandtl-Glauert equation

$$(1 - M_\infty^2)\Phi_{xx} + \Phi_{yy} + \Phi_{zz} = 0. \quad (2.8)$$

The equations can be further simplified if the flow solved is incompressible, when we obtain Laplace's equation

$$\nabla^2\Phi = 0. \quad (2.9)$$

Navier-Stokes and Euler

The Navier-Stokes equations describe the flow of air (a Newtonian fluid) with good realism. These were formulated in 1847 by Navier and later Stokes obtained the same equations independently. However, the solution of its full form is still an ongoing area of research. If the Reynolds' number of the flow is sufficiently high then the influence of viscous terms can be neglected and the Euler equations are obtained. The three-dimensional Euler equations can be written in conservative form and Cartesian coordinates as

$$\mathbf{w}_t + \mathbf{F}_x^i + \mathbf{G}_y^i + \mathbf{H}_z^i = 0 \quad (2.10)$$

where $\mathbf{w} = (\rho, \rho u, \rho v, \rho w, \rho E)^T$ denotes the vector of conservative variables. The flux vectors \mathbf{F}^i , \mathbf{G}^i and \mathbf{H}^i are,

$$\mathbf{F}^i = \begin{pmatrix} \rho U^* \\ \rho u U^* + p \\ \rho v U^* \\ \rho w U^* \\ U^*(\rho E + p) + x_i p \end{pmatrix}, \quad (2.11)$$

$$\mathbf{G}^i = \begin{pmatrix} \rho V^* \\ \rho u V^* \\ \rho v V^* + p \\ \rho w V^* \\ V^*(\rho E + p) + y_t p \end{pmatrix}, \quad (2.12)$$

$$\mathbf{H}^i = \begin{pmatrix} \rho W^* \\ \rho u W^* + p \\ \rho v W^* \\ \rho w W^* + p \\ W^*(\rho E + p) + z_t p \end{pmatrix}. \quad (2.13)$$

In the above ρ , u , v , w , p and E denote the density, the three Cartesian components of the velocity, the pressure and the specific total energy respectively, and U^* , V^* , W^* the three Cartesian components of the velocity relative to the moving coordinate system which has local velocity components x_t , y_t and z_t , i.e.

$$U^* = u - x_t \quad (2.14)$$

$$V^* = v - y_t \quad (2.15)$$

$$W^* = w - z_t. \quad (2.16)$$

The Euler equations can be solved using numerical methods. Since the equations permit rotational flow and entropy changes (eg through shock waves), they are very useful in solving transonic flow problems, and flows with vortical structures already in the field. They cannot predict the influence of the boundary layer, including separation and the displacement effect, which would in general require the Navier-Stokes equations. A simpler approach to including boundary layer effects is to couple an inviscid solution of the Euler equations with a boundary layer solver.

Choice of Model for Aeroelastic Simulation

The solution of the linearised potential flow model leads to a linear relationship between the deflections of the body and the forces introduced. This is very useful for

developing a matrix based analysis of aeroelastic stability. However, as discussed, the ability to describe shock waves and viscous effects is lost. Traditionally the potential model has been used almost exclusively for aeroelastic design calculations of aircraft. Research effort has been put into scaling the linear relationship to force agreement with higher fidelity models or measurements [14]. This approach cannot be expected to allow good prediction of nonlinear flow effects. The presence of shock waves in the flowfield leads to several nonlinear aeroelastic effects, including the transonic dip and limit cycle oscillations. To investigate these phenomena, a flow model able to realistically predict the shock waves is required. The TSD or full potential models are therefore candidates for the flow description, within their limitations on the shock strength. However, modern CFD techniques have tended to focus on solutions of the Euler equations, which treat the shock wave without simplifying assumptions. In addition, methods established for the Euler equations can easily be extended to the Navier-Stokes equations, and hence incorporate viscous effects. Hence, for establishing a nonlinear aeroelasticity prediction code for transonic wing flutter, the Euler equations capture the essential physics whilst being easily generalised. This is therefore the approach used in the current work.

2.1.3 Numerical Method

The flow solution in the current work is obtained using the Glasgow University code PMB(parallel multi-block). A summary of the applications examined using the code can be found in reference [15]. A fully implicit solution of the Euler equations is obtained by advancing the solution forward in time by solving the discrete nonlinear system of equations

$$\frac{\partial \mathbf{w}^{n+1}}{\partial \tau} = \frac{3\bar{\mathbf{w}}^{n+1} - 4\bar{\mathbf{w}}^n + \bar{\mathbf{w}}^{n-1}}{2\Delta t} + R(\mathbf{w}^{n+1}). \quad (2.17)$$

In the above, the first term on the right hand side is the discretisation of the time derivative of the unknown vector ($\bar{\mathbf{w}} = \bar{\rho}_i, \bar{\rho}_i u_i, \bar{\rho}_i v_i, \bar{\rho}_i w_i, \bar{\rho}_i E_i, \dots$) where the subscript i denotes the i th cell in the grid and $\bar{\rho} = V_i \rho_i$ where V_i is the volume of the cell. The second term on the right hand side, called the residual, is the discretisation of the convective terms, given here by Osher's approximate Riemann solver [16], MUSCL interpolation [17] and Van Albada's limiter. The right hand side is iterated to the updated flow solution \mathbf{w}^{n+1} by the introduction of the pseudo time derivative on the left hand side. This term is discretised by

$$\frac{\partial \mathbf{w}^{n+1}}{\partial \tau} = \frac{\mathbf{w}^{n+1,k+1} - \mathbf{w}^{n+1,k}}{\Delta \tau} \quad (2.18)$$

to create the iteration through τ . If the first term on the right hand side is neglected then this iteration is to the usual (non real time varying) steady state. At convergence, the updated flow solution is second order accurate in the real time step, Δt . The convergence level is monitored by the pseudo time tolerance (PTT) given by

$$\text{PTT} = \frac{\|\mathbf{w}^{n+1,k+1} - \mathbf{w}^{n+1,k}\|_2}{\|\mathbf{w}^{n+1,k+1} - \mathbf{w}^n\|_2} \quad (2.19)$$

which compares the size of the latest pseudo update with the latest best estimate of the real time update. The pseudo time problem is a nonlinear system of algebraic equations. These are solved in the current work by an implicit method which has been found to be efficient for calculating flow steady states [18]. The main features of the method involve an approximate linearisation to reduce the size and condition number of the linear system, and the use of a preconditioned Krylov subspace method to calculate the updates. The method has been tested on a number of unsteady flow problems including cavity flow [19], pulsed spiked body flow [20], buffeting [21] and moving wings [22].

For aeroelastic applications the flow domain is deforming. A moving grid treatment is therefore required. The grids used in the current work are block structured,

although the flow solution methodology is suitable for unstructured grids as well. The grids are deformed by interpolating boundary displacements to interior points [23]. The approach is independent of the method used to generate the initial grid. Grid speeds and transformation Jacobians are calculated by finite differences. Cell volumes are recalculated using a global conservation law by considering volume fluxes through cell sides. In the present calculations the geometric conservation law (GCL) was used.

2.1.4 Example of Flow Solutions

Results are first presented to validate and verify the flow solver. The F5 wing is a fighter type wing with small aspect ratio, a high leading edge sweep and about 5% thickness. Experimental data for a range of steady and pitching cases is available in [24] [25]. Previous results with the present method have been documented in [22] for cases involving rigid pitch and in [26] for steady flows around the wing with a tip launcher and missile. The results we present here are for the clean stationary wing with the freestream flow at Mach 0.896 and an incidence of 0.497 degrees. The grid, shown in figure 2.1, is of the C-O type with 125 points in the streamwise direction, 25 points normal to the wing and 25 points in the spanwise direction. The time for one evaluation of the residual on this grid is 4.56 seconds on a Pentium Pro 200 processor. The convergence history is shown in figure 2.2. The magnitude of the residual (in the L2 norm) is reduced by 6 orders of magnitude in the equivalent time for 1560 work units¹ which takes 120 minutes on a single Pentium Pro 200 processor. The pressure coefficient at 8 spanwise slices is shown in figure 2.3. Good agreement is obtained except for a discrepancy in the shock location due to the absence of the boundary layer displacement effect in the inviscid results. Finally, a plot of the pressure contours on

¹1 work unit is the time for one residual evaluation

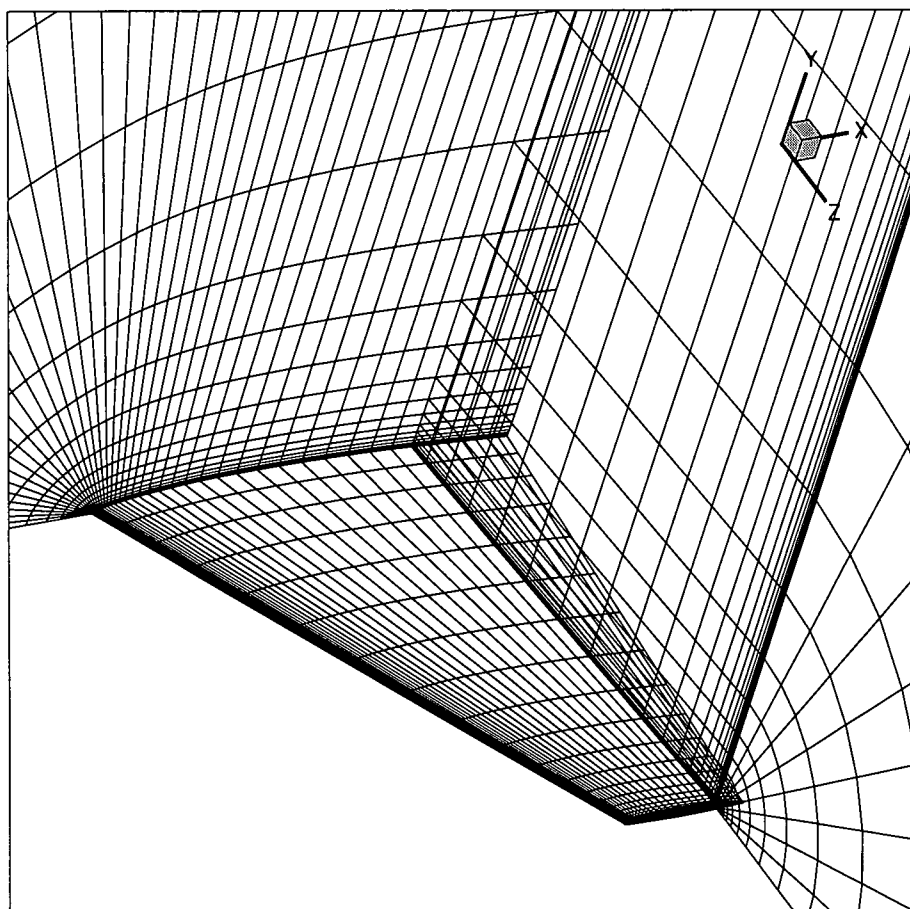


Figure 2.1: C-O grid for F5 test case.

the upper surface of the wing is shown in figure 2.4. The shock wave strengthens as the tip is approached.

We next look at a rigid pitching case on the same grid. The freestream Mach number is 0.947 and the mean incidence is -0.006° . The amplitude of the sinusoidal pitching is 0.132° and the reduced frequency is 0.264. Twenty real time steps were used to resolve each period, leading to a total CPU time of 3681 work units to compute one cycle. On average 19.6 pseudo time iterations were required to drive the residual down four orders of magnitude at each real time step. The Fourier analysed pressure

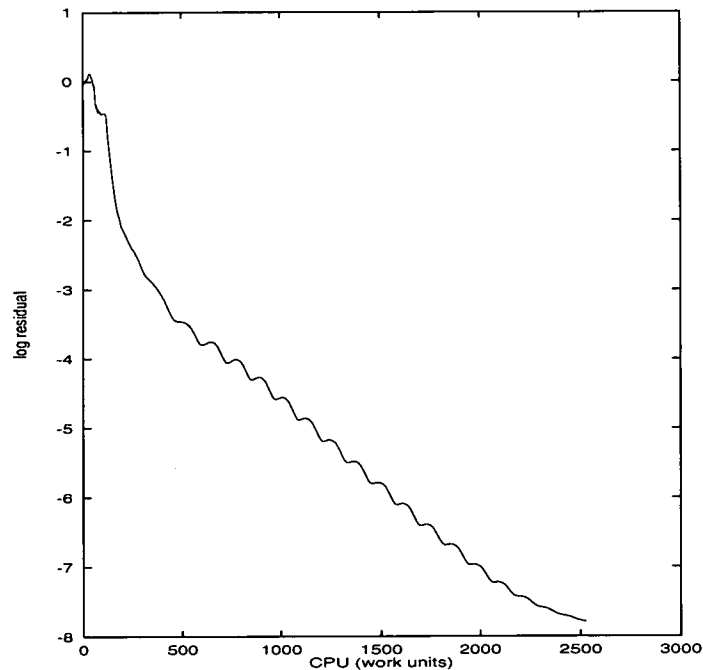


Figure 2.2: F5 test case convergence history. $M_\infty = 0.896$, $\alpha = 0.497^\circ$.

coefficients are shown in figures 2.5 and there is good agreement with experiment. Note that the pressure coefficient is defined by

$$C_p = 2(p - p_\infty)/(\rho_\infty U_\infty^2). \quad (2.20)$$

The main flow feature is a shock wave towards the trailing edge. The computation of similar cases for Mach numbers in the range 0.597 to 1.336 shows a similar level of numerical performance and agreement with measurements [22].

2.2 Structural Model

2.2.1 Linear Elasticity Review

We start with the two dimensional static linear case. The state of the strains at a point is defined in terms of stress components. Stress specifies how forces are transmitted

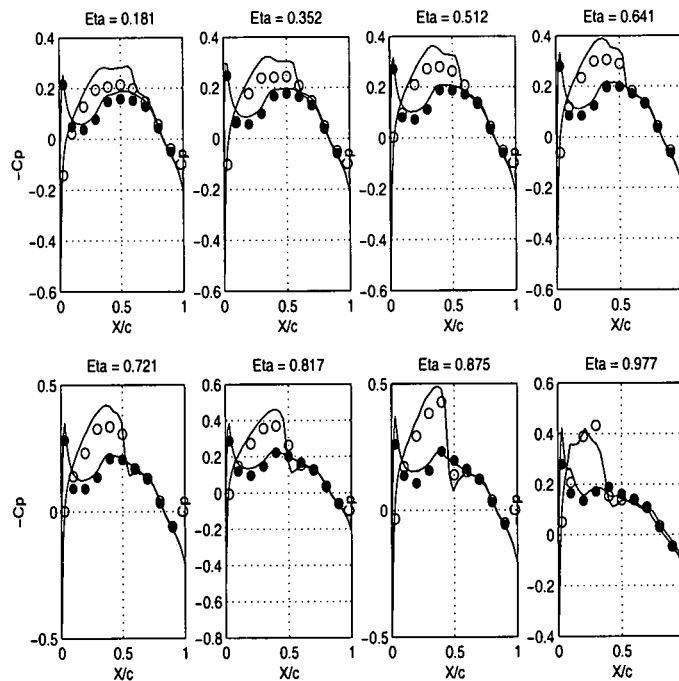


Figure 2.3: F5 test case pressure distributions. $M_\infty = 0.896$, $\alpha = 0.497^\circ$. The solid dots are the experimental measurements on the lower surface and the unfilled dots are from the upper surface.

to a continuous body. The stress is defined as force divided by area. The planes normal and parallel to the coordinates help to define the 3×3 stress tensor σ which is a symmetric matrix.

The force equilibrium equations in three dimensions on a small element can be written as

$$\begin{aligned}
 \frac{\partial \sigma_{xx}}{\partial x} + \frac{\partial \sigma_{yx}}{\partial y} + \frac{\partial \sigma_{zx}}{\partial z} + b_x &= 0. \\
 \frac{\partial \sigma_{yx}}{\partial x} + \frac{\partial \sigma_{yy}}{\partial y} + \frac{\partial \sigma_{zy}}{\partial z} + b_y &= 0. \\
 \frac{\partial \sigma_{zx}}{\partial x} + \frac{\partial \sigma_{yz}}{\partial y} + \frac{\partial \sigma_{zz}}{\partial z} + b_z &= 0.
 \end{aligned}
 \tag{2.21}$$

The indicial form of this can be written as

$$\sigma_{ij,j} + b_i = 0, i, j = 1, 2, 3.
 \tag{2.22}$$

Here the subscripts 1, 2, 3 refer to x, y, z and \mathbf{b} refers to the body force vector which

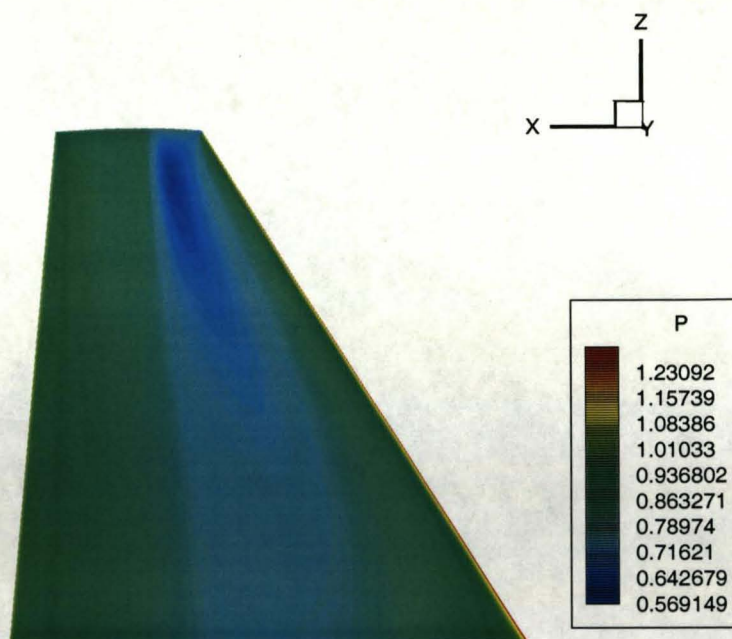


Figure 2.4: F5 test case pressure contours. $M_\infty = 0.896$, $\alpha = 0.497^\circ$.

has components b_1 , b_2 and b_3 .

Stress boundary conditions are associated with the equilibrium equation. The tractions on the boundary of the domain are denoted \bar{p}_x , \bar{p}_y and \bar{p}_z . Equilibrium at the boundary requires the tractions on the boundary

$$p_i = \sigma_{ij}n_j = \bar{p}_i \quad (2.23)$$

to be satisfied where n_i are the direction cosines of the outward normal \mathbf{n} with respect to the x,y,z axes.

The 3×3 strain tensor ϵ is linked to the displacements for the linear theory as

$$\epsilon_{ij} = \frac{1}{2}(u_{i,j} + u_{j,i}). \quad (2.24)$$

The state of stress and strain are related by $\sigma = \mathcal{D}_r \epsilon$, where \mathcal{D}_r is called the rigidity coefficients matrix, which depends on the elasticity coefficients (Young's modulus, Poisson's ratio and modulus of elasticity).

The basic structural model equations are not simplified unlike the fluid case but there are two different solution approaches which we consider, namely the finite element method (FEM) and the boundary element method (BEM). These are reviewed briefly in the next section.

2.2.2 Finite Element Model (FEM)

With advances in computational methods, finite element methods matured to allow the static and dynamic response of a structure to be determined. Stiffness (\mathbf{K}) and mass (\mathbf{M}) matrices are used to determine the equation of motion of an elastic structure subjected to an external force \mathbf{f}_s :

$$\mathbf{M}\delta\ddot{\mathbf{x}}_s + \mathbf{K}\delta\mathbf{x}_s = \mathbf{f}_s \quad (2.25)$$

where $\delta\mathbf{x}_s$ is a vector of displacements on a grid of points \mathbf{x}_s . The structural matrices can be regarded as fixed at values calculated for the initial structure or can be updated as a function of \mathbf{x}_s . Because the system we are considering is linear it is assumed that the structure characteristics are determined once and for all before the flutter calculations, so that \mathbf{M} and \mathbf{K} are constant matrices generated by, for example, the commercial package NASTRAN.

It is possible to directly couple a flow solver such as pmb with a structural solver, such as NASTRAN. An approach used by the current author consisted of communicating between the two packages through files. From pmb, the unix command system

was used to run NASTRAN and to produce the NASTRAN files which contained the required surface force data. Then pmb read the data from the NASTRAN output files to obtain the structural displacements. However, this method proved to be very slow, and a better approach would be to have the finite element source code and include it with pmb to communicate through memory, or to interface through buffers, using the DMAP capability of Nastran.

Another approach is to print the mass and stiffness matrices from the finite element package and then to use a Runge-Kutta ODE solver which is coupled with the flow solver. However, if the structure is linear and the stiffness and mass matrices do not change during calculations, the structural model can be reduced to a modal model, resulting in a very efficient structural solution.

2.2.3 Modal Model

In many cases the full finite element model can be simplified by neglecting all but a few dominant modes. The wing deflections $\delta \mathbf{x}_s$ are defined at a set of grid points \mathbf{x}_s by

$$\delta \mathbf{x}_s = \sum \alpha_i \phi_i \quad (2.26)$$

where ϕ_i are the mode shapes and α_i the generalised displacements. Here the α_i depend on time but the mode shapes are fixed. The values of ϕ_i and ω_i are calculated by solving the eigenvalue problem

$$[\mathbf{M} - \omega_i^2 \mathbf{K}] \phi_i = \mathbf{0} \quad (2.27)$$

where \mathbf{M} and \mathbf{K} are the mass and stiffness matrices from the finite element model of the structure. The eigenvectors are scaled so that

$$[\phi_i]^T M [\phi_i] = 1. \quad (2.28)$$

Projecting the finite element equations onto the mode shapes results in the equations

$$\frac{d^2\alpha_i}{dt^2} + \omega_i^2\alpha_i = \phi_i^T \mathbf{f}_s \quad (2.29)$$

where \mathbf{f}_s is the vector of external forces at the structural grid points. This equation can be solved by a two stage Runge-Kutta method, which requires a knowledge of \mathbf{f}_s^n and \mathbf{f}_s^{n+1} . The accuracy of the modal model depends on enough modes being used.

2.2.4 Boundary Element Method (BEM)

An alternative solution method for the structural equations is called the BEM. Here, the structural equation can be solved through an integration over the structural surface only. This is in contrast to the finite element method which is discretised in three dimensional space. The potential advantages of the BEM over the FEM are that only a surface mesh is required and that the dimensions of the matrices are reduced. From an aeroelastic point of view the treatment of the structural model only using surface information offers potential benefits. This is considered in detail in chapter 3.

2.2.5 Discussion

Computational Structural Dynamics (CSD) is more mature than CFD because of a longer history of development. Several commercial FEM packages are in routine use. For linear structural analysis the structural simulation is much cheaper than a typical CFD simulation, and involves the solution of an ODE. The use of the modal simplification further improves this situation. The main problem arising from the structural model for an aeroelastic simulation is associated with the transfer of the fluid forces from the aerodynamic solver. This is the topic considered in chapter 4, 5 and 6. This problem also motivates an interest in the BEM, as discussed in chapter 3.

2.3 Time Sequencing of the Models

2.3.1 Formulation

The flow solver passes the required force information to the structure which returns the structural motion to the flow solver. This coupled problem is typically solved using the structural and flow solvers in sequence. The sequencing, which is used for numerical convenience, introduces an additional source of error into the calculation. This error is potentially serious since the energy exchange between the fluid and structure is altered. The consequence is a reduction in the time step which can be used to accurately calculate a response compared with the flow or structural solvers used separately, hence making an already expensive calculation more costly. This was shown in Djayapertapa's Thesis [27] where such an approach, called weak coupling, was compared with a strong coupling. The rate of decay of a pitch-plunge NACA64A10 airfoil was considered at Mach 0.85, and the strongly coupled method, which avoided sequencing errors, was found to yield advantages in the size of time step allowed, and hence in the computational efficiency.

The main cost in a fluid-structure interaction simulation is normally incurred during the flow solution. It is therefore very important to optimise the flow solver. A basic design criterion for a numerical method for unsteady flows is that the time step used should be chosen only on the basis of requirements for accurately following the evolution of the flow without considerations from other numerical factors like stability. The framework introduced by Jameson [28] allows this to be achieved by reformulating the problem of updating the flow as the solution of a modified steady state problem, which can be calculated using the most successful methods for steady state flow analysis.

Within this formulation an iteration is used to update the flow solution. This

raises the possibility of building the structural solution into this iteration with the converged flow and structural solutions progressing forward in time together. The main question is whether the coupled solution behaves (in terms of time accuracy) as well as the two components of the simulation when used separately.

The Euler equations are solved in a time varying domain $\Gamma = \Gamma(t)$. The boundaries of this domain $\partial\Gamma$ consist of the structural surface and the truncated far field. The structural model is used to compute the response of the structure, and hence the evolution of Γ . To illustrate the influence of the time sequencing for the full problem, a test problem consisting of the response of an aerofoil free to move in pitch and plunge is considered in the current section. This problem includes the influence of time coupling but avoids the effect of transferring data between the fluid and structural grids.

Following the formulation of Kousen and Bendiksen[29], the equations describing this are

$$\frac{d\mathbf{q}}{dt} = \mathcal{F}(\mathbf{q}, \mathbf{w}) \quad (2.30)$$

where $\mathbf{q} = (\alpha, h, d\alpha/dt, dh/dt)^T$, α is the aerofoil incidence and h is the vertical displacement non dimensionalised by the semi-chord, measured positive downwards. The vector on the right hand side is $\mathcal{F}(\mathbf{q}, \mathbf{w}) = (q_3, q_4, F_3, F_4)^T$ where, denoting $\tilde{\mathbf{q}} = (q_1, q_2)^T$, $\tilde{\mathbf{F}} = (F_3, F_4)^T$ is given by

$$\tilde{\mathbf{F}} = \mathbf{f}(\mathbf{w}) - M^{-1}K\tilde{\mathbf{q}} \quad (2.31)$$

where

$$\mathbf{M} = \begin{bmatrix} 1 & x_\alpha \\ x_\alpha & r_\alpha^2 \end{bmatrix}$$

$$\mathbf{K} = \begin{bmatrix} \omega_R^2 & 0 \\ 0 & r_\alpha^2 \end{bmatrix}, \mathbf{f} = \begin{bmatrix} -C_L/\beta \\ 2C_M/\beta \end{bmatrix}$$

and $\beta = 4/(\pi\mu\omega_\alpha^R)$. The notation and values used here are

- C_L and C_M are the lift and moment coefficients obtained from the flow solution
- M and K are the mass and stiffness matrices respectively
- $x_\alpha = -0.2$ is the offset between the centre of gravity and the point about which the pitching motion takes place (called the elastic axis) , measured negatively for the centre of gravity aft of the elastic axis
- $r_\alpha^2 = 0.29$ is the radius of gyration, representing the effect of the moment of inertia about the elastic axis
- $\omega_R^2 = 0.11789$ is the square of the ratio of the natural frequencies of plunging ω_h to pitching ω_α
- $\mu = 10$ is the ratio of the aerofoil to fluid mass
- $\bar{U} = 4b/(U_\infty\omega_\alpha)$ is called the reduced velocity of the problem where U_∞ is the freestream fluid velocity and b is the aerofoil chord length. Increasing values of the reduced velocity indicate an increasingly flexible structure.

Using the solution of equation (2.29), the geometry for the flow problem can now be denoted $\Gamma = \Gamma(\mathbf{q})$, and hence depends on the structural solution. In return, the structural solution depends on the flow solution through the surface forces \mathbf{f} . Following the pseudo-time approach of Jameson for the flow solution and using a Runge Kutta solution for the structural solution, the updated flow and structural solutions at time $n+1$ are calculated from the nonlinear system of algebraic equations

$$\mathbf{R}_{i,j}^* = \frac{3\bar{\mathbf{w}}_{i,j}^{n+1} - 4\bar{\mathbf{w}}_{i,j}^n + \bar{\mathbf{w}}_{i,j}^{n-1}}{2\Delta t} + \mathbf{R}_{i,j}(\mathbf{w}_{i,j}^{n+1}) = 0 \quad (2.32)$$

for $\Gamma = \Gamma(\mathbf{q}^{n+1})$ and

$$\mathbf{q}^{n+1} = \mathcal{G}(\mathbf{q}^n, \mathbf{f}^n, \mathbf{f}^{n+1}) \quad (2.33)$$

where \mathcal{G} indicates the Runge-Kutta solution. If an uncoupled solution is used then force values at time levels $n-1$ and n are used to extrapolate for the values at $n+1$. The updated structural solution is then used to update the flow solution. However, the mismatch between the force values associated with the flow solution and the extrapolated values used to update the flow solution introduces a source of error into the calculation which is potentially serious since it is associated with the transfer of energy between the fluid and structure which is the crucial feature of the problem. We refer to this method as being sequenced in real time.

This phasing error was removed in reference [30] by using the same Runge Kutta method to update the flow instead of equation (2.32). However, using an explicit method to update the flow values incurs a stability restriction on the size of the time step. Using equation (2.32) is preferable from this point of view since the time step can be chosen on the basis of time accuracy alone. Equation (2.32) is solved by introducing an iteration $\mathbf{w}_{i,j}^{n+1,m}$ through pseudo time which converges to the updated flow solution. An iteration for the structural solution can be introduced so that the latest approximation to the updated lift and moment values is used to calculate a better approximation to the updated pitch and plunge, eg

$$\mathbf{q}^{n+1,m+1} = \mathcal{G}(\mathbf{q}^n, \mathbf{f}^n, \mathbf{f}^{n+1,m}). \quad (2.34)$$

The $m + 1$ th flow iterate is calculated for the geometry $\Gamma = \Gamma(\alpha^{n+1})$. The mesh velocities required for the transformation are calculated from the mesh locations at time n and pseudo time iterate $n+1,m$. At convergence, the structural solution has been updated using the the correct moment and lift values. The solution is sequenced in pseudo time, with the solution being coupled in real time.

The next section uses a test problem involving limit cycle oscillations due to shock motions to evaluate the influence of using coupled or sequenced solutions in

real time on the computed responses and the efficiency of the method. The test case considered involves delicate dynamics and is more difficult than the target wing flutter simulations. It can therefore be seen as a severe test of the approach.

2.3.2 Results

To provide a reference for the coupled solution we first look at the performance of the flow solver alone when applied to calculate the flow over a NACA64A006 aerofoil following a pitching motion at similar conditions to the free response examined later (sinusoidal pitching with an amplitude of 3.3 degrees and a reduced frequency of 0.31). The convergence of the maximum moment coefficient during the cycle is shown in figure 2.6.

Results are shown for the second order flow solver using equation (2.32) and for a first order method given by

$$\mathbf{R}_{i,j}^* = \frac{\bar{\mathbf{w}}_{i,j}^{n+1} - \bar{\mathbf{w}}_{i,j}^n}{\Delta t} + \mathbf{R}_{i,j}(\mathbf{w}_{i,j}^{n+1}) = 0. \quad (2.35)$$

The superior convergence of the second order method is clear and a good solution is obtained using a time step of 0.32 (20 steps per cycle) for which the maximum lift is within 0.5% of the fully converged value. The first order solution does not reach this accuracy with 320 steps per cycle and exhibits linear convergence.

To isolate the time sequencing influence we consider the response of an aerofoil section moving in two degrees of freedom. To examine these issues we use a test problem involving the pitch-plunge response of the NACA64A006 in a freestream at $M_\infty = 0.85$. This problem has been previously studied in references [29] and [32]. The bifurcation behaviour is shown in figure 2.7 and shows the response changing from a stable zero position to divergence followed by a finite amplitude limit cycle. The particular example we use here is at $\bar{U} = 1.9$ which features flutter-divergence

interaction. The nonlinear nature of the behaviour presents the numerical scheme with a significant test.

A time step refinement was carried out to test time accuracy using the solution which is sequenced in real time, the results of which are shown in figures 2.8 and 2.9. The first point to notice is that the solution appears to be converging to a solution with negative divergence when the traces with $\Delta t = 0.64, 0.32, 0.16$ and 0.08 are examined. However, when the time step is reduced to $\Delta t = 0.04, 0.02$ and 0.01 there appears to be a step change to positive divergence. Initial conditions used here are $\alpha_0 = 1.0$ degrees and $h_0 = 0$. This behaviour is explained by the need to resolve the fast initial transient accurately, which is not done for the larger time steps. To test this, a method with varying time step given by

$$\Delta t^{n+1} = \min(1.1\Delta t^n, \Delta t_{max}) \quad (2.36)$$

was used with $\Delta t^1 = 0.02$. This ensures that a small time step is used initially which is increased to some maximum value as the calculation proceeds. Compared with using a constant time step $\Delta t = 0.02$ throughout the calculation, this approach gives identical results for $\Delta t_{max} = 0.16$ when using sequencing in pseudo time, as shown in figure 2.10.

The traces obtained using sequencing in real and pseudo time are compared in figure 2.11 for the limit cycle phase of the motion. The sequenced solution in real time obtained using $\Delta t = 0.08$ is comparable in terms of quality with the solution obtained using $\Delta t = 0.32$ for sequencing in pseudo time, as shown in table 2.1. Hence, the solution which is sequenced in pseudo time gives some benefit in avoiding temporal errors introduced by the sequencing. From the table it is evident that introducing the structural solver into the pseudo time iterations does not increase the number of steps required to attain a converged flow solution. However, the method which is

Sequencing	Time Step	α_{min}	α_{max}	iterations/real time step	CPU/unit time
real time	0.64	-4.00	3.05	11.2	5.59
	0.32	-3.48	2.74	10.1	9.98
	0.16	-3.38	2.68	9.2	17.56
	0.08	-3.34	2.65	8.3	29.63
	0.04	-2.56	3.18	7.2	49.94
	0.02	-2.45	3.11	-	-
pseudo time	0.64	-3.05	1.91	11.3	8.06
	0.32	-3.32	2.50	10.1	13.81
	0.16	-3.35	2.63	9.3	24.50
	0.08	-3.33	2.64	8.3	42.63

Table 2.1: summary of time step refinement

sequenced in pseudo time requires the solution of the structural equations and the movement of the mesh at each pseudo time step rather than just once per real time step. This increases the cost of each pseudo step by about 40 % in the current case.

2.4 Conclusions

The three dimensional flow solver, modal structural solver and the time sequencing have been described. For single discipline simulations the flow and modal solvers work well. The use of time sequencing in pseudo time allows sequencing errors between the two simulations to be removed in a straight-forward fashion. Satisfactory results were obtained for the pitch-plunge test case whose dynamics is more difficult than the target wing flutter simulations. The approach of sequencing in pseudo time will be therefore be considered satisfactory.

The final problem to be overcome before time marching wing flutter simulations can be carried out is that of transferring information between the fluid and structural grids. This is investigated in the coming chapters.

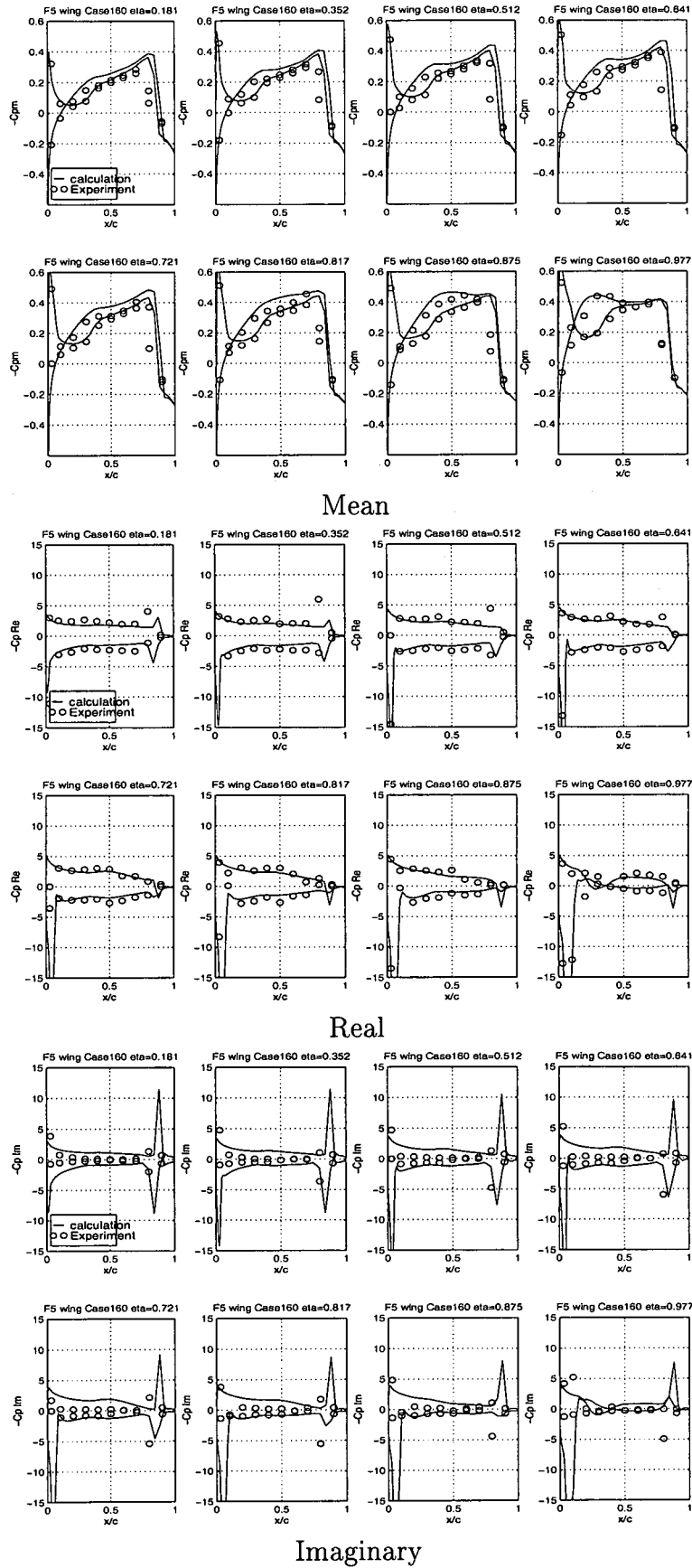


Figure 2.5: Comparison between computed and experimental data for mean, real and imaginary pressure coefficients for the rigid pitching F5 wing case.

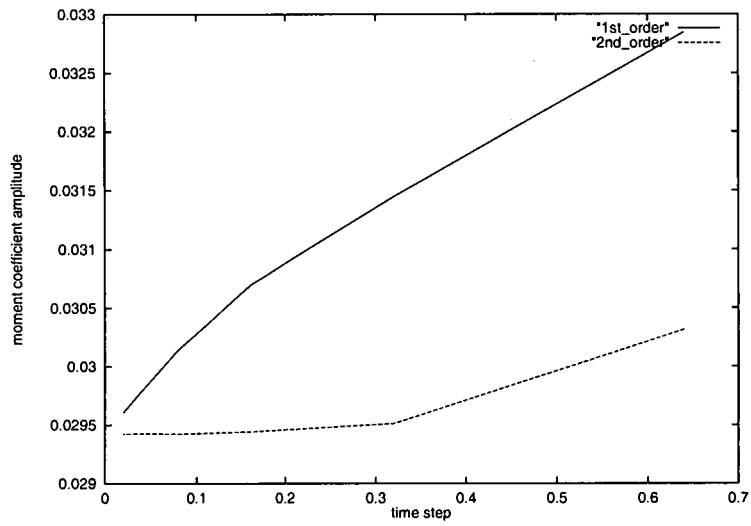


Figure 2.6: Convergence of maximum moment coefficient for forced pitching.

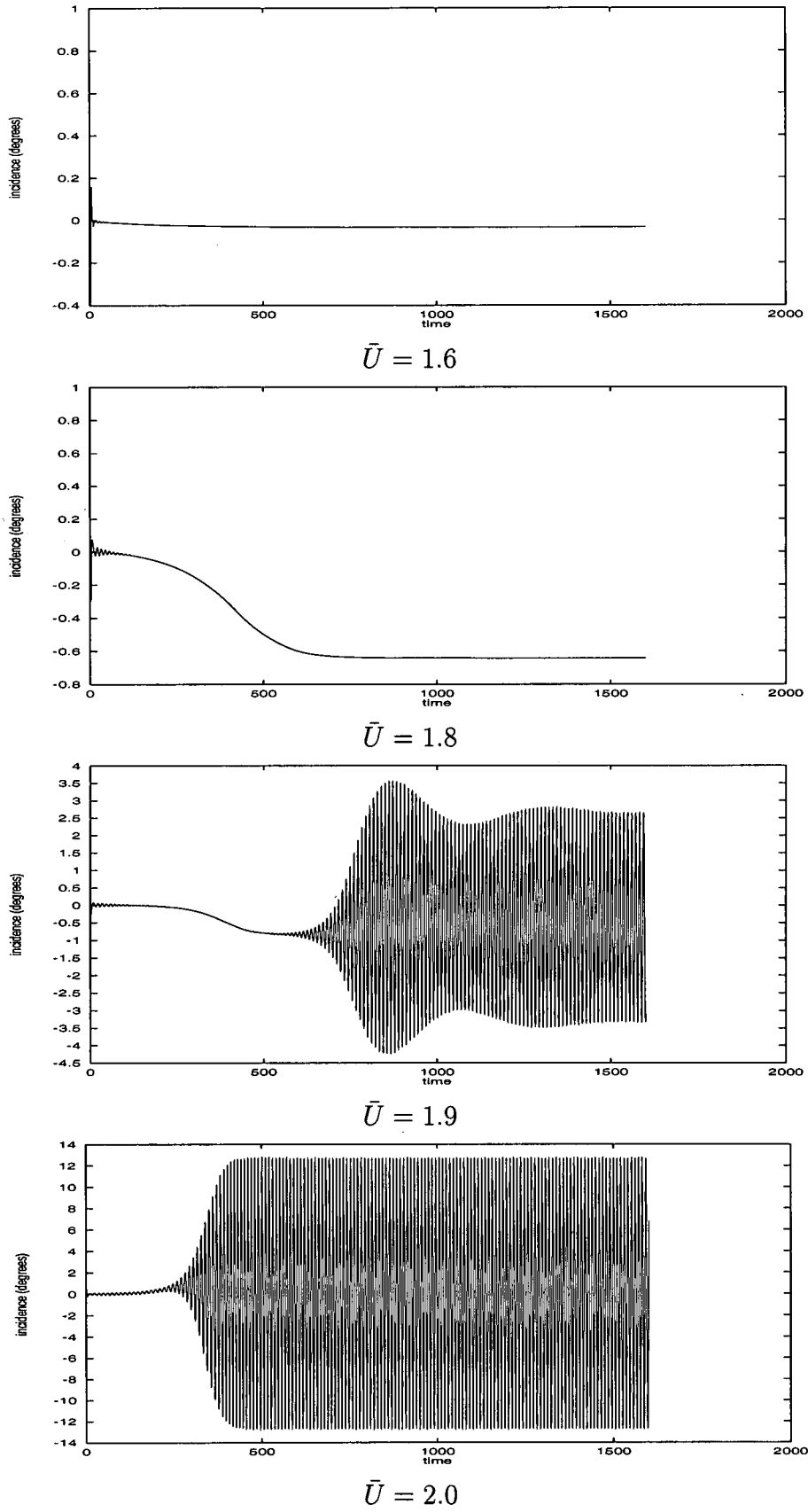


Figure 2.7: Behaviour for varying \bar{U} .

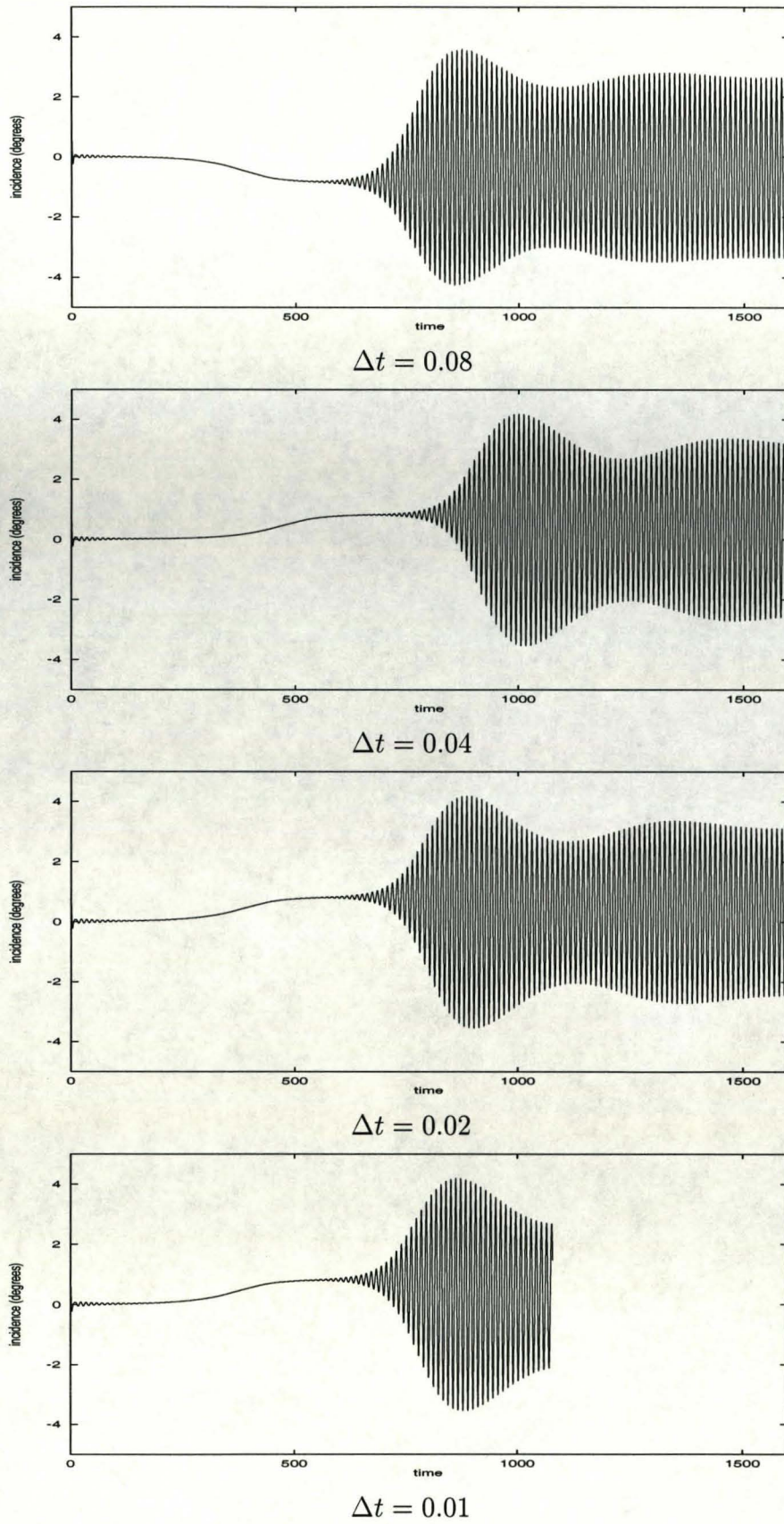


Figure 2.8: Time Convergence for $\bar{U} = 1.9$.

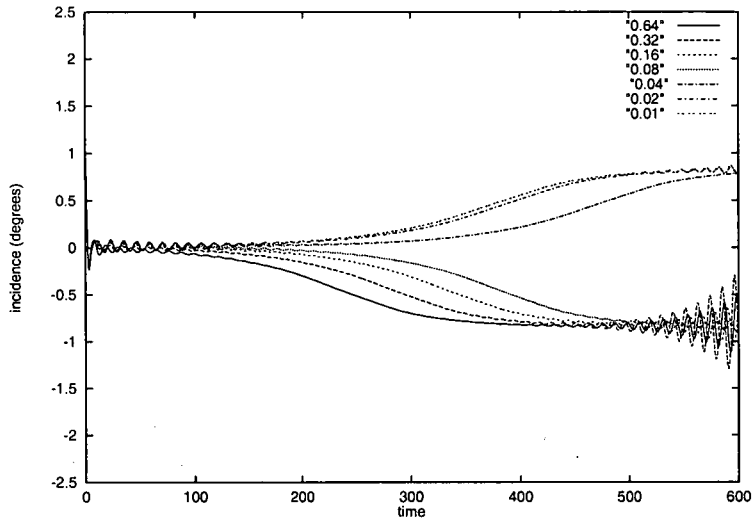


Figure 2.9: Time Convergence for $\bar{U} = 1.9$.

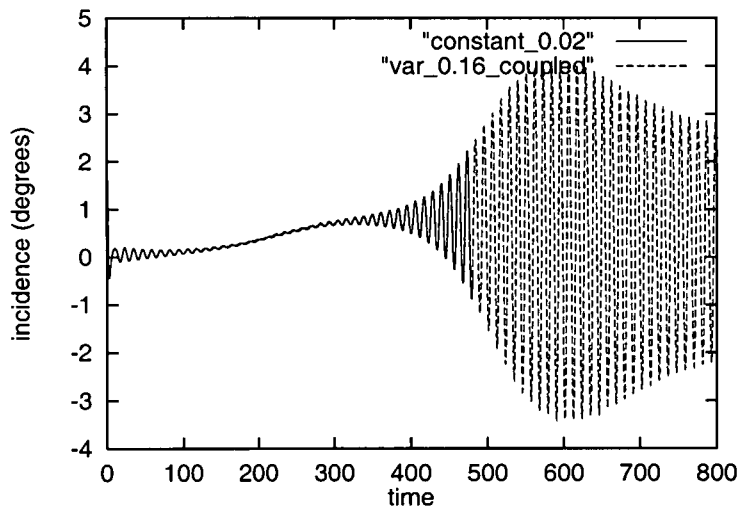
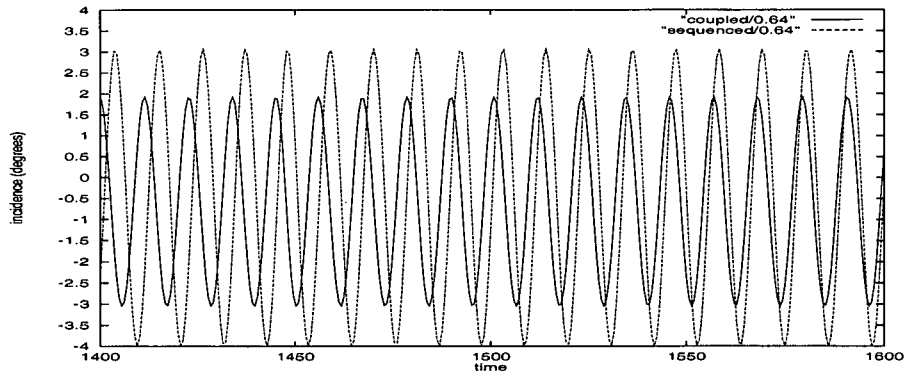
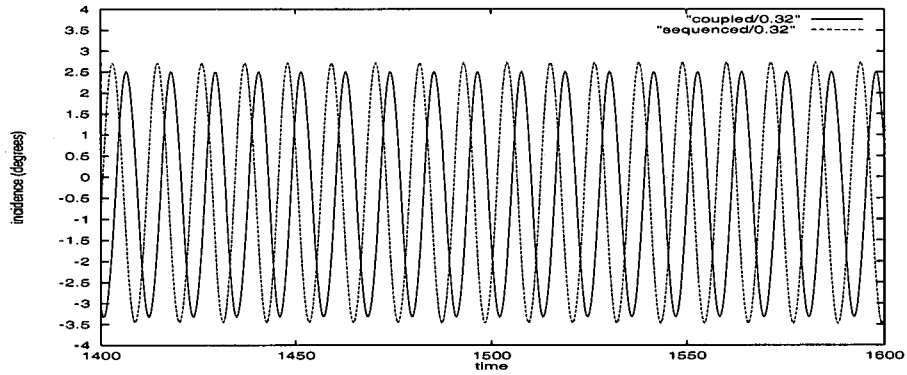


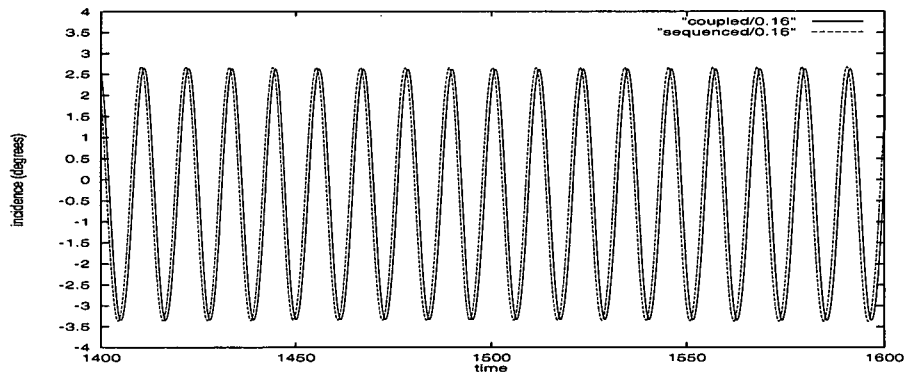
Figure 2.10: Comparison of aerofoil response using a constant time step $\Delta t = 0.02$ and a variable time step with $\Delta t_{max} = 0.16$.



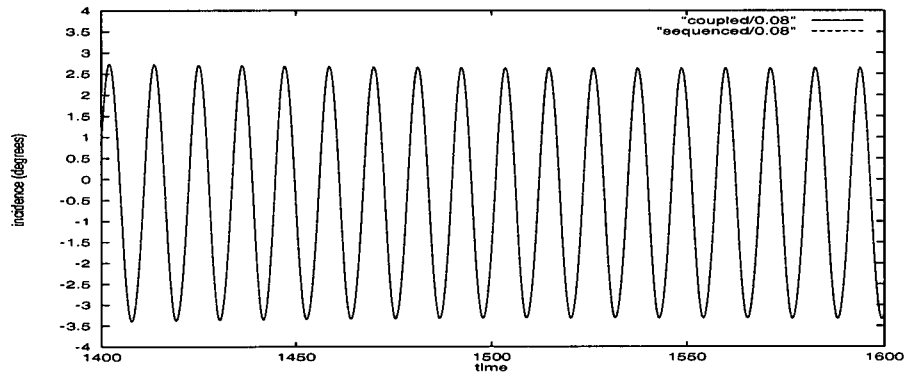
$$\Delta t = 0.64$$



$$\Delta t = 0.32$$



$$\Delta t = 0.16$$



$$\Delta t = 0.08$$

Figure 2.11: Coupling comparison for $\bar{U} = 1.9$.

Chapter 3 : Direct Solution by BEM

3.1 Overview

For aeroelastic simulations the finite element method (FEM) is almost always used to obtain the structural solution. Using FEM normally introduces the necessity of interpolating the structural displacements to the fluid mesh, and the fluid forces to the structural nodes. It is worth considering if an approach could be found to remove the interfacing problem altogether by, for instance, changing the type of structural solver. The interpolation problem is exacerbated when the surface of the structural model does not coincide with the fluid surface. By using the boundary element method (BEM) as the structural solver, the fluid and structural meshes can be defined on the same surface, and by using the fluid surface mesh as the BEM grid, the fluid and structural meshes can be made to coincide easily, and in fact mesh generation for the structural model is then completely avoided. In this chapter we consider the practicality of such an approach.

First, the formulation for the BEM method is presented (following [36] [37] [38]) and its implementation is described and validated. Finally the practicality of the proposed approach for aeroelasticity simulation is discussed.

3.2 Formulation and Implementation

3.2.1 Origins

The development of the boundary element is reviewed in the recent thesis of Gao [39]. A boundary element formulation was developed in the 1960's to study torsion problems in regular shafts [40] [41]. Constant elements were applied for the direct integral formulation for 2d problems in reference [42] and in 3d in [43]. The boundary element method gained in popularity with the research community after a conference in 1978 at Southampton University. In civil engineering the boundary element method is being developed to study increasingly complex problems, including non-linear structural effects as in reference [39]. However, the BEM has hardly penetrated aeronautical engineering as a tool for structural analysis. The formulation used in this chapter reflects this situation in that basic methods, which have been incorporated into a simple research code written in the C programming language, are used to gain insight into whether the BEM could be considered as a means to remove the interfacing problem between FEM and aerodynamics models for aeroelastic simulation. No new developments on the BEM formulation have been undertaken as they are beyond the scope of this thesis.

3.2.2 The Problem

Following [36] [37] consider a homogeneous body that occupies a volume Γ enclosed by the boundary $\partial\Gamma$ which is composed of Γ_1 and Γ_2 . Let \mathbf{u} , $\boldsymbol{\epsilon}$ and $\boldsymbol{\sigma}$ be the displacement, strain and stress fields in Γ and let \mathbf{p} be the traction vector. We assume that the body is restrained on Γ_1 and loaded on the free boundary Γ_2 .¹ If the body has linear

¹The application of boundary conditions is usually more general than this with, for example, mixed traction and displacement conditions at the same point. However, in the current work this situation does not arise.

elastic behaviour and the small displacement theory is assumed then

$$\boldsymbol{\sigma} = \mathcal{D}_r \boldsymbol{\epsilon} \quad (3.1)$$

in Γ . Here \mathcal{D}_r is the rigidity coefficients matrix.

The steady state differential equations of motion of a medium Γ enclosed by a boundary $\delta\Gamma$ are expressed in tensor notation as

$$\sigma_{ij,j} + b_i = 0 \quad (3.2)$$

with the boundary conditions

$$\begin{aligned} u_i &= \bar{u}_i, \text{ on } \Gamma_1 \\ p_i &= \bar{p}_i, \text{ on } \Gamma_2. \end{aligned} \quad (3.3)$$

Here \mathbf{b} represents the body forces on the volume Γ , $\boldsymbol{\sigma}$ the Cartesian stress tensor, \mathbf{u} the vector displacement field, Γ_1 the part of the boundary where kinematic conditions are imposed, Γ_2 the part of the boundary where traction conditions are imposed, $\bar{\mathbf{u}}$ the known displacements on Γ_1 and $\bar{\mathbf{p}}$ the known tractions on Γ_2 . The tractions on the boundary are related to the stress tensor by the expression $p_i = \sigma_{ij}n_j$, where n_j are the components of the outward normal to the boundary.

3.2.3 Weighted Residual

As in [36], the numerical solution, \mathbf{u} is approximated and the error can be minimised, by weighting the governing equation by a new function \mathbf{u}^* . Taking into account the equilibrium equation (3.2) and the boundary conditions (3.3) a weighted residual statement can be written as

$$\int_{\Gamma} (\sigma_{kj,j} + b_k) u_k^* d\Gamma = \int_{\Gamma_2} (p_k - \bar{p}_k) u_k^* d\Gamma + \int_{\Gamma_1} (u_k - \bar{u}_k) p_k^* d\Gamma \quad (3.4)$$

where \mathbf{u}^* , \mathbf{p}^* are the displacements and tractions corresponding to the weighting field. The strain-displacement relationship and the constitutive equation are assumed to apply to both the approximating and the weighting field. Here u_k^* are the virtual displacements which satisfy the homogeneous boundary conditions $\bar{u}_k^* = 0$. We interpret u_k^* as a weighting function and $p_k^* = n_j \sigma_{jk}^*$ as the surface tractions corresponding to the u_k^* system. It is assumed that the strain-displacement relationships are linear, i.e.

$$\begin{aligned} \epsilon_{ij} &= \frac{1}{2}(u_{i,j} + u_{j,i}) \\ \epsilon_{ij}^* &= \frac{1}{2}(u_{i,j}^* + u_{j,i}^*) \end{aligned} \quad (3.5)$$

and that the material properties are also linear.

Integrating twice by parts in equation (3.4), the boundary integral formulation of the problem is written (see Appendix A) as

$$\int_{\Gamma} \sigma_{kj,j}^* u_k d\Gamma + \int_{\Gamma} b_k u_k^* d\Gamma = - \int_{\Gamma_2} \bar{p}_k u_k^* d\Gamma - \int_{\Gamma_1} p_k u_k^* d\Gamma - \int_{\Gamma_2} u_k p_k^* d\Gamma + \int_{\Gamma_1} \bar{u}_k p_k^* d\Gamma \quad (3.6)$$

3.2.4 Fundamental Solution

The weighting field chosen is the fundamental solution (given in Appendix A) for the elasticity problem, i.e. the solution corresponding to the equation

$$\sigma_{kj,j}^* + \delta_k^i = 0 \quad (3.7)$$

with δ_k^i representing a unit load acting at point i in the direction k . With this weighting field, the displacements at any point inside the solid are given by

$$c^i u_l^i + \int_{\Gamma_1} \bar{u}_k p_{l,k}^* d\Gamma + \int_{\Gamma_2} u_k p_{l,k}^* d\Gamma = \int_{\Gamma} b_k u_{k,l}^* d\Gamma + \int_{\Gamma_1} p_k u_{l,k}^* d\Gamma - \int_{\Gamma_2} \bar{p}_k u_{l,k}^* d\Gamma \quad (3.8)$$

with $c^i = 1$.

As the point i approaches a smooth boundary the integrals on the left hand side yield a jump term. Then equation (3.8) holds but with $c^i = 1/2$.

3.3 Implementation

3.3.1 Matrix Notation

Following the formulation in [38], the implementation is presented for two dimensional problems. Equation (3.8) can be written in matrix form by defining some arrays. The fundamental solution terms in the integrals can be written, in two dimensions, as matrices with elements \mathbf{P}^* and \mathbf{U}^*

$$\mathbf{U}^* = \begin{bmatrix} u_{xx}^* & u_{xy}^* \\ u_{yx}^* & u_{yy}^* \end{bmatrix}, \quad \mathbf{P}^* = \begin{bmatrix} p_{xx}^* & p_{xy}^* \\ p_{yx}^* & p_{yy}^* \end{bmatrix} \quad (3.9)$$

The basic equation (3.8) applied at point i then becomes (assuming that the body force is zero),

$$\mathbf{c}^i \mathbf{u}^i + \int_{\Gamma_1} \mathbf{P}^* \mathbf{u} d\Gamma = \int_{\Gamma_2} \mathbf{U}^* \mathbf{p} d\Gamma \quad (3.10)$$

where \mathbf{u}^i defines the displacements at the internal or boundary point i and \mathbf{c}^i is a 2×2 constant array whose values depend on the type of point under consideration. If point i is an internal point, $c_{kl}^i = \delta_{kl}$, and if the node is a boundary point on a smooth surface $c_{kl}^i = \frac{1}{2} \delta_{kl}$.

3.3.2 Matrix Form after discretising the boundary

The volume surface is discretised by elements which can be constant, linear, quadratic or even of higher order. For some elements (linear for instance), the corners have to be treated with care because of discontinuities of the structure which can complicate numerical implementation. In order to avoid this problem, constant elements can be used, but this means that more elements are required for accuracy.

If the surface of the boundary under study is discretized using constant elements, this implies that the values of \mathbf{u} and \mathbf{p} are equal to the value at the mid-node of the element. If the body surface is discretized into N constant boundary elements then

for element i

$$\mathbf{c}^i \mathbf{u}^i + \sum_{j=1}^N \left(\int_{\Gamma_j} \mathbf{P}^* d\Gamma \right) \mathbf{u}^j = \sum_{j=1}^N \left(\int_{\Gamma_j} \mathbf{U}^* d\Gamma \right) \mathbf{p}^j. \quad (3.11)$$

The spatial order of the solution can be increased by using linear elements with the displacements and the pressures being represented in terms of linear shape functions. For instance if \mathcal{N}_1 and \mathcal{N}_2 are the shape functions, the displacement of a point situated on the j -th element with end points at nodes l_j and r_j is given by

$$\mathbf{u}^j(x) = \mathcal{N}_1(\xi) \mathbf{u}_{l_j} + \mathcal{N}_2(\xi) \mathbf{u}_{r_j} = \xi \mathbf{u}_{l_j} + (1 - \xi) \mathbf{u}_{r_j} \quad (3.12)$$

where ξ is the normalized coordinate which measures distance along the element. The discrete form of equation (3.10) then becomes

$$\mathbf{c}^i \mathbf{u}^i + \sum_{j=1}^N \int_{\Gamma_j} \mathbf{P}^* (\xi \mathbf{u}_{l_j} + (1 - \xi) \mathbf{u}_{r_j}) d\Gamma = \sum_{j=1}^N \int_{\Gamma_j} \mathbf{U}^* (\xi \mathbf{p}_{l_j} + (1 - \xi) \mathbf{p}_{r_j}) d\Gamma \quad (3.13)$$

where the superscript i now refers to nodal values.

The integrals produce, in two dimensions, two 2×2 submatrices called $\bar{\mathbf{H}}$ and $\bar{\mathbf{G}}$. The equation (3.11) can now be written as

$$\mathbf{c}^i \mathbf{u}^i + \sum_{j=1}^N \bar{H}_{ij} \mathbf{u}^j = \sum_{j=1}^N \bar{G}_{ij} \mathbf{p}^j. \quad (3.14)$$

This equation relates the values of \mathbf{u} at node i with the values of \mathbf{u} and \mathbf{p} at all the nodes on the boundary, including node i and can be written in a more compact way, if we define $H_{ij} = \bar{H}_{ij}$ when $i \neq j$ and $H_{ij} = \bar{H}_{ij} + c^i$ when $i = j$. The equation then has the following form

$$\sum_{j=1}^N H_{ij} \mathbf{u}^j = \sum_{j=1}^N G_{ij} \mathbf{p}^j. \quad (3.15)$$

Applying this equation to all boundary points, the result can also be written in matrix form

$$\mathbf{H}\mathbf{u} = \mathbf{G}\mathbf{p}. \quad (3.16)$$

Here \mathbf{H} and \mathbf{G} are $2M \times 2M$ matrices where M is the number of boundary nodes.

3.3.3 Results at Internal Points

Once the values of displacements and tractions are known on the boundary it is possible to calculate the displacements at any internal point. The displacements are given by

$$\mathbf{u}^i = \int_{\Gamma} \mathbf{u}^* \mathbf{p} d\Gamma - \int_{\Gamma} \mathbf{p}^* \mathbf{u} d\Gamma. \quad (3.17)$$

In the same way as matrices \mathbf{H} and \mathbf{G} were introduced above, matrices \mathbf{H}_{bi} and \mathbf{G}_{bi} are defined and they relate the internal points to the boundary points

$$\mathbf{u}^i = \mathbf{G}_{bi} \mathbf{p} - \mathbf{H}_{bi} \mathbf{u}. \quad (3.18)$$

3.3.4 Integral Calculations

A major issue for the implementation is the evaluation of the integrals to define the matrices \mathbf{H} and \mathbf{G} . For integrals which are not singular, a weighted Gauss method is used.

If the function to be integrated becomes singular, the method used for constant elements is to exclude an area around the singular point from the calculation, following the subdivision approach introduced by Lachat [44] who showed that this works for weakly singular integrals (which arise for the terms in the matrix \mathbf{G}). For constant elements the analytical form of the strongly singular integrals is available in [37] on page 144.

For linear elements the regular integrals are again evaluated using the Gauss method. The following relations result from invariance under rigid rotation and translation. For rigid translation

$$\begin{aligned} \sum_i H_{1i} &= 0 \\ \sum_i H_{2i} &= 0 \end{aligned} \quad (3.19)$$

and for the rigid rotation,

$$\sum_i H_{1i}(x_2)_i = \sum_i H_{2i}(x_1)_i$$

$$\sum_i H_{2i}(x_3)_i = \sum_i H_{3i}(x_2)_i$$

$$\sum_i H_{1i}(x_3)_i = \sum_i H_{3i}(x_1)_i$$

where H_{1i}, H_{2i}, H_{3i} correspond to a row of coefficients in the influence matrix corresponding to the node in the direction of x_1, x_2, x_3 respectively. These relations can be used to evaluate the diagonal terms on the matrices in terms of off-diagonal terms, thus avoiding the evaluation of the singular integrals. They can also be used to check the formulation for constant elements.

3.4 Validation

To test the implementation some examples of in-plane static analysis for homogeneous bodies are presented.

3.4.1 2D Circular Cavity Test

A cavity under internal pressure in an infinite medium is studied. The example is taken from Brebbia [36]. The circular cavity is under internal pressure in an infinite medium. The cavity has a radius of 100 in, a shear modulus of $0.945e+5$ N/in^2 and Poisson's ratio of 0.1. The structure is discretised using 24 constant elements. The axis system used has its origin at the centre of the cavity. Comparisons of the displacements at the point (-400 in,0) are given on the Table 3.1 and agree quantitatively.

X0	Y0	dX Brebbia	dY Brebbia	dX Glasgow	dY Glasgow
-400.0	0.0	-0.1250002e-2	0.1111766e-7	-0.1293453e-02	-2.303930e-19

Table 3.1: Circular cavity internal point displacements. All distances are in inches.

3.4.2 Cantilever Beam

This case is taken from Nikken and Brebbia[35]. A beam is under transversal parabolic forces at its two ends. On the left end, horizontal displacements are constrained, with the lower corner node displacements set to zero. The calculations with constant

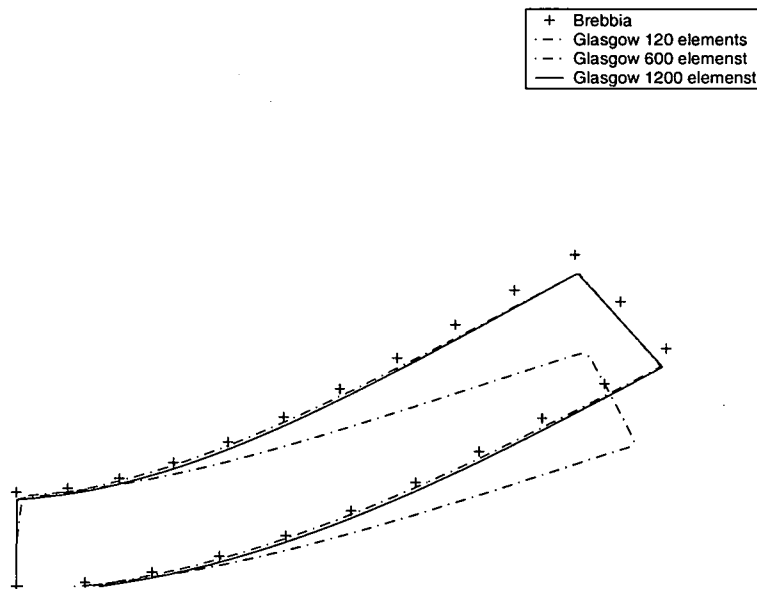


Figure 3.1: Cantilevered Beam Using Constant Elements

elements converge for 600 elements as shown in figure 3.1. The current results compare reasonably well with previous results obtained using quadratic elements.

The second comparison when using linear elements is shown in figure 3.2 . The linear code requires 360 elements for a converged solution. Note that for the circle case, the constant and linear BEM give the same results using 24 elements. However,

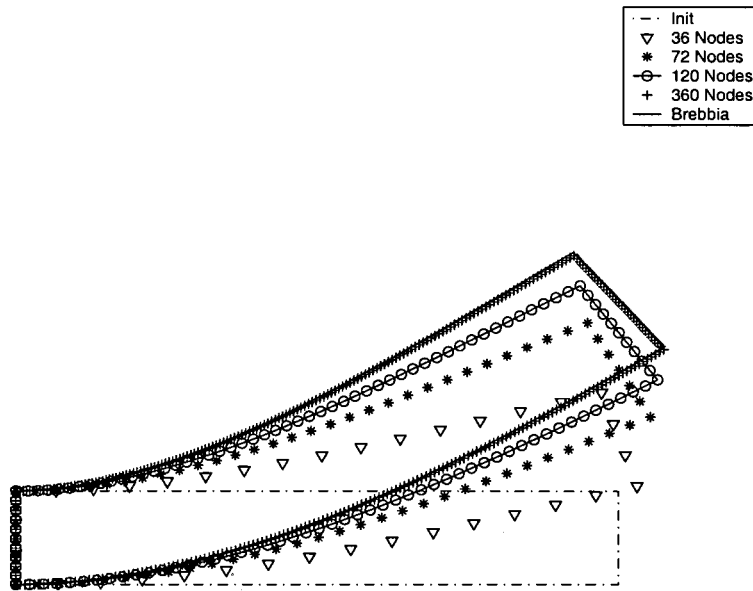


Figure 3.2: Cantilevered Beam Using Linear Elements

for the beam, 360 nodes are needed for convergence using linear elements, whereas 600 nodes are required to converge using constant elements. Faster convergence is obtainable if the integrals are calculated more accurately. However, at convergence, the constant BEM model does not converge to the right final position. It has been suggested in reference [35] that when bending is important, constant elements are insufficient to obtain the right solution.

3.4.3 Conclusion

We have presented here the implementation of the boundary element method. Boundary element solutions offer several advantages over the 'volume' type method. The boundary method can be formulated in terms of influence functions and involves only discretisation on boundary surface elements. The current implementation is made using constant and linear element models.

The potential use of the BEM for advanced industrial type application such as

wing flutter is considered in the following section. Indeed, the popular method in industry to perform aeroelastic calculations is to model the structure using finite element methods or lumped mass models. To our knowledge, no effort has been made to couple directly a BEM solver with a finite volume based flow solver for such challenging problems as aircraft flutter phenomena. The feasibility of the approach is considered in the next section.

3.5 BEM as a Direct Solver

Before we move on to consider the issue of transferring information between offset fluid and structural grids it is interesting to consider the feasibility of using the BEM as a direct solver for aeroelastic problems. In theory, if the fluid surface mesh could be used as the mesh for a structural solution done by using the BEM, then the only additional work required to setup the coupled solution compared with a CFD simulation would be to specify the structural properties. Due to the coincidence of the fluid and structural meshes (by definition), the transfer of forces and displacements would be avoided, thus resolving this problem.

First, we consider whether the fluid surface mesh would be suitable in terms of accuracy for the BEM solution. To test this a flow calculation on a mesh with 129 points around and 33 points normal to the surface was undertaken for the NACA4412 aerofoil at six degrees incidence and a Mach number of 0.6. This mesh has 97 points on the aerofoil surface. The grid is shown in figure 3.3. The pressure contours for these conditions indicate a shock wave on the upper surface which is well resolved, as shown in figure 3.4. The fluid grid here is of standard dimensions for an inviscid aerofoil calculation and has been shown by many authors to be capable of resolving the flow accurately if a second order spatial scheme is applied.

The surface pressures were re-dimensionalised assuming a free stream density of $0.2\text{kg}/\text{m}^3$ and a freestream speed of $247\text{m}/\text{s}$. These values are typical of the calculations for the AGARD 445.6 wing shown later. The forces at the fluid centres were then fed into the linear static BEM solver just described. The aerofoil was fixed at the trailing edge and the deflections calculated assuming a shear modulus of $3 \times 10^8 \text{Pa}$ and a Poisson ratio of 0.33. The resulting deflection is a nose up bending as shown in figure 3.5. Next, a coarser BEM mesh was created by merging adjacent cells in the original mesh. The deflection calculated on this coarser mesh is also shown in figure 3.5. It is clear that the original mesh is the minimum which would be required for spatial accuracy of the BEM solver. In fact, considering the cantilever beam example shown above it would be expected that a finer grid might be required. These conclusions are all for a linear BEM solver and of course the mesh requirements could be reduced by using quadratic or higher order elements. As observed earlier the convergence performance of the BEM is sensitive to the accuracy of the numerical integration scheme used and the number of elements required might be significantly reduced by using an improved method.

The following discussion is based on (and hence restricted to) the BEM formulation described above. These results allow an estimate of the cost of a BEM solution for a statically deflecting wing. The static BEM solver requires two full matrices to be stored, each of which has dimension $(3N_s)^2$ where N_s is the number of surface points in the fluid mesh. For the AGARD 445.6 wing considered below $N_s = 1500$ although this could be considered as a low value due to the simplicity of the wing geometry and the flow over it (i.e. no strong shocks or separations). For this value, the number of floats that need to be stored is $2 \times 9 \times N_s^2$ which works out at 36 million. This is comparable with the number of values which must be stored due to the implicit nature of the flow solver. For realistic cases a parallel solution is required to cope with

the memory requirements of the flow solver alone. Hence, it can be anticipated that a parallel BEM solver would be needed also. However, in the case of the flow solver the linear system is sparse whereas the BEM system is full. The parallel solution of a full system is a harder problem since iterative type methods need good preconditioning to converge, and this can be done relatively efficiently for sparse matrices but is not so easy for full matrices. So there are practical numerical issues which make using BEM structural solutions on the fluid surface grid a less attractive proposition than it might originally appear.

Secondly, the BEM method works well when the geometry is an enclosed and contiguous shape. Wing structures are not like this since they consist of a lattice of beams. A BEM solution would need to describe this internal complexity to allow a realistic description of the structure. This would entail an increase in cost compared to the estimates of the previous paragraph and also the loss of the simplicity which is a motivating factor for considering this approach in the first place. The FEM can often construct a simplified version of the structure which reproduces the structural behaviour very well (eg using a wing box). Direct application of the BEM formulation used in this thesis is unlikely to prove successful for modelling wing flutter. An improved formulation might change this conclusion and would involve accurate integral evaluations, multi-region and shell capabilities. These features improve the convergence and matrix conditioning properties of the method but their development lies outside the scope of the thesis. We continue with an FEM representation of the structure and attempt to resolve the problems this causes with respect to transferring information between the structural and fluid grids.

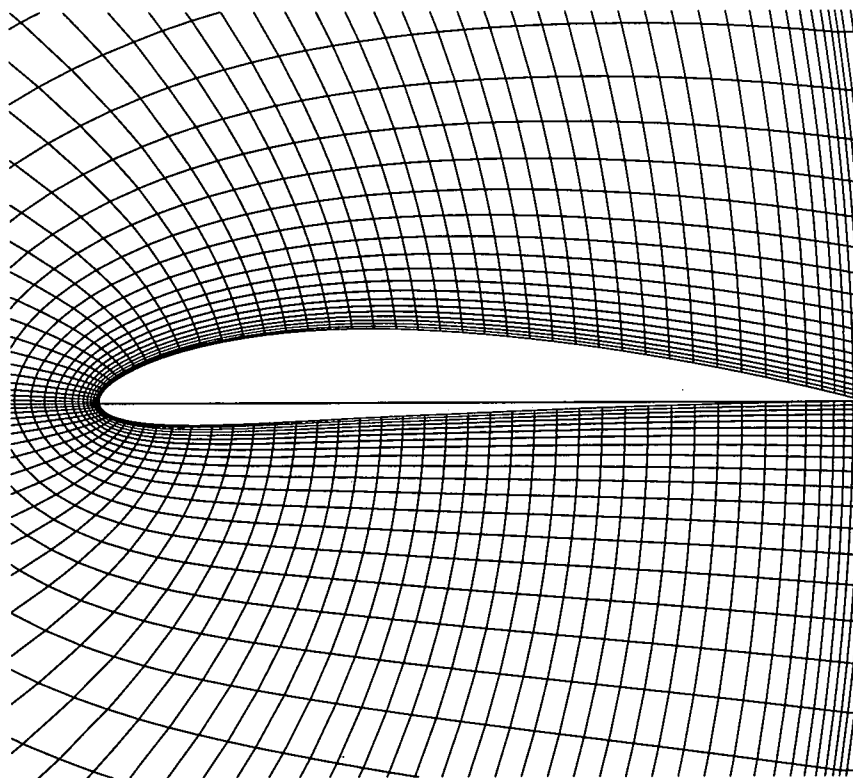


Figure 3.3: Grid for NACA4412 aerofoil.

3.6 Conclusion

In conclusion, using the boundary element method can eliminate the coupling problem. However, significant practical problems arise, especially considering complex structures such as wings. Even if from the hardware and software point of view this is feasible, from an engineering one this is often impractical. A real wing can be modelled accurately by simplifying the structural components, reducing the effort required

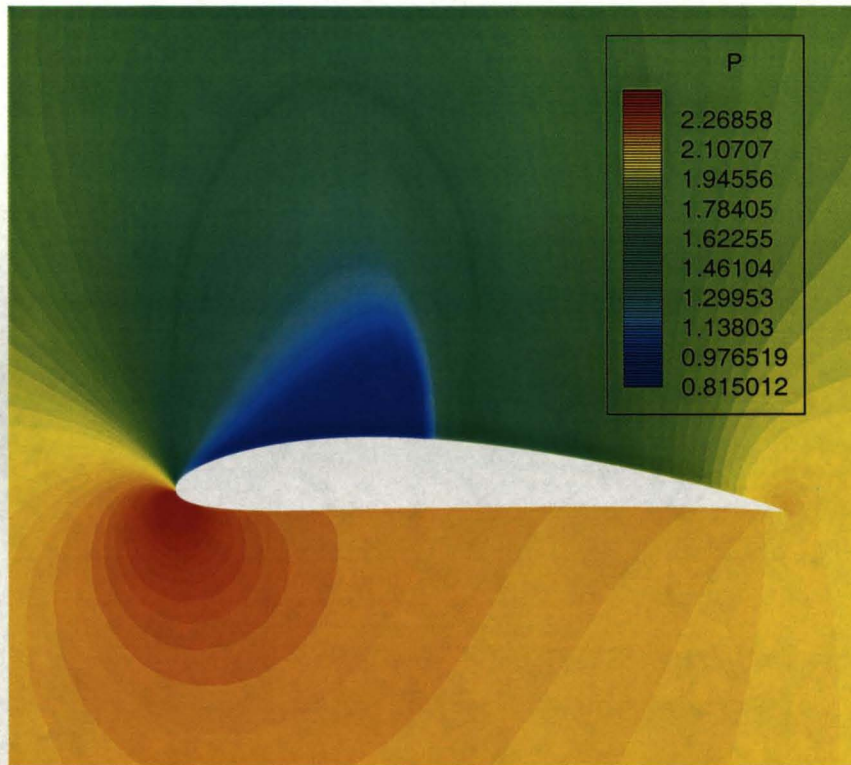


Figure 3.4: Pressure contours for NACA4412 aerofoil at $M_\infty = 0.6$ and $\alpha = 6^\circ$.

to model all the structural details. It is therefore concluded that direct application of the BEM is unlikely to prove successful for modelling wing flutter. An alternative approach which uses the BEM as the basis for a transformation method between a finite element grid and a fluid grid is instead considered.

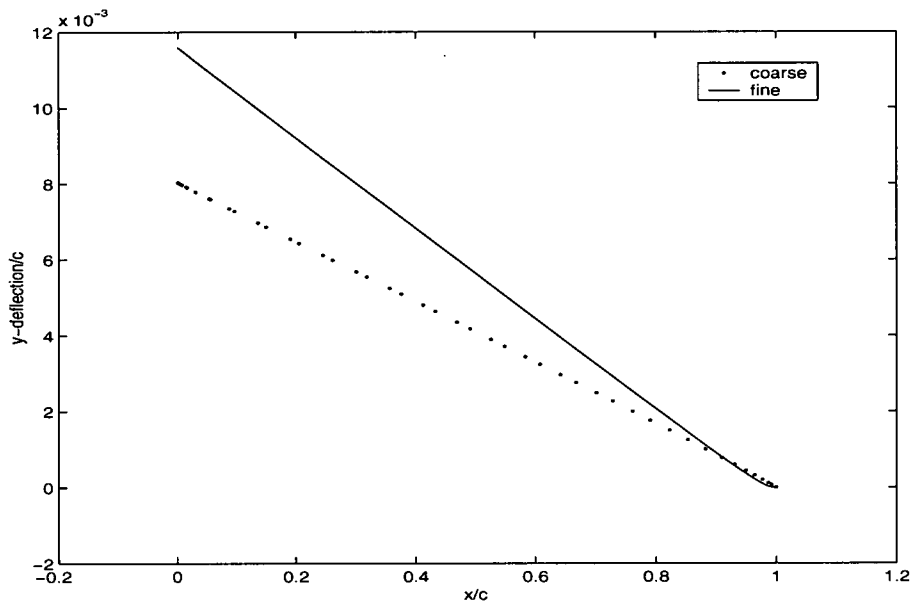


Figure 3.5: Normal deflections for NACA4412 aerofoil on the fine (i.e. derived from CFD) and coarse meshes.

Chapter 4 : Review of interpolation Methods

4.1 Overview

The state of the art for computational fluid dynamics (CFD) and computational structural dynamics (CSD) is represented by different types of numerical methods, finite volume and finite element respectively. This means that simulating a fluid-structure interaction using one monolithic code is an unattractive proposition. A more popular alternative is to interface well established CFD and CSD codes through a coupling procedure. Coupling between the fluid and the structure is achieved by exchanging boundary data, such as aerodynamic pressures and structural deflections, at each time step.

There are two cases to consider for the data exchange. First, even if the surfaces of the fluid and structural problems coincide, in general the grids for the fluid and structure do not. Therefore interpolation between these grids is required. The second case, which arises frequently in aeroelastic analysis, is when the fluid and structural surfaces themselves do not coincide. This happens when a simplified representation is used for the structure but the fluid simulation is carried out for the full geometry. In this case, displacements from the structural surface are used to reconstruct the fluid surface. A plate structural model can be used to represent various aircraft components. If the real geometry is used for the fluid solution then the problem of passing information between the fluid and structural grids becomes more complicated.

Historically, interpolation methods have been developed for fluid-structure simulations based on potential aerodynamic models and plate based structural models. Here, the fluid and structural surfaces are both defined on a plate. For wing flutter simulations the dominant motions are bending and torsion, with dilatation being small. For this type of motion there is only a small coupling between the displacements in different directions and this fact has influenced the interpolation methods developed. A review of these methods is presented in this chapter.

The following notation is adopted. A grid point is denoted by $\mathbf{x}_{ss} = [x_{ss}, y_{ss}]^T$ when it lies on a 2d surface (such as a plate) and $\mathbf{x}_{ss} = [x_{ss}, y_{ss}, z_{ss}]^T$ when it lies on a general three dimensional surface. Here the subscript ss could denote the aerodynamic grid (a), the structural grid (s) or a virtual grid (v). It is useful to define a vector which contain all of the grid points strung together and this is denoted by $\tilde{\mathbf{x}}_{ss} = [x_{ss,1}, \dots, x_{ss,N}]^T$ where $x_{ss,i}$ is the i th point of type ss . Similar definitions are used for $\tilde{\mathbf{y}}_{ss}$ and $\tilde{\mathbf{z}}_{ss}$. Similarly, $\hat{\mathbf{x}}_{ss} = [x_{ss,1}, y_{ss,1}, z_{ss,1}, \dots, x_{ss,N}, y_{ss,N}, z_{ss,N}]^T$. Finally, changes in a grid point location are denoted by adding δ in front of the symbol for the location(s).

4.2 Spline Type Methods

The first proposed transfer method for aeroelastic calculations was the least squares technique, developed by Schmitt [45] in 1956. This calculated out of plane deflections for grids defined on a plate. Assume that the vertical (i.e. out-of-plane) displacements δz_i are known at N structural nodes $\mathbf{x}_{s,i} = (x_{s,i}, y_{s,i})^T$. The displacements at M aerodynamic grid points $\mathbf{x}_{a,i} = (x_{a,i}, y_{a,i})^T$ are calculated from evaluating the expression

$$\delta z(x, y) = \sum_{i=1}^{i=N} c_i E(\mathbf{x}_{s,i}) \quad (4.1)$$

where E is a known function, and c_i are constants calculated by the least squares method, minimising the errors at structural grid points. The function E used in the original paper was $E(\mathbf{x}) = E(x, y) = \phi_a(x)\phi_b(y)$, where ϕ_a and ϕ_b are the bending modes for a beam.

A significant advance followed when Harder and Desmarais developed the Infinite Plate Spline (IPS) method [46]. IPS remains one of the most popular methods for interpolation and is used in the current thesis to provide benchmark results for evaluation of the developed methods.

4.2.1 Infinite Plate Spline

IPS is based on the superposition of solutions for the partial differential equation of equilibrium for an infinite plate. Using the solutions of the infinite plate equation, the set of concentrated loads at the known data points which gives rise to the known structural deflections is calculated. Those concentrated forces are then substituted back into the solution, thus providing a smooth surface that passes through the structural points. The resulting expression is then evaluated on the aerodynamic grid. Points far away from known points are extrapolated nearly linearly. This method is used in this thesis for comparison and hence a more detailed formulation is given

A surface spline defines the out-of-plane deflections $\delta z(\mathbf{x}) = \delta z(x, y)$ of an infinite thin plate which pass through known structural deflections $\delta z(\mathbf{x}_{s,i}) = \delta z_i$. The static equilibrium equation for the plate is

$$\mathcal{D}\nabla^4\delta z = q_l \quad (4.2)$$

where \mathcal{D} is the plate flexibility and q_l the distributed load. The solution, can be written as

$$\delta z(x, y) = a_0 + a_1x + a_2y + \sum_{i=1}^N \mathcal{F}_i r_i^2 \ln r_i^2 \quad (4.3)$$

where r_i is the distance from the point (x, y) to the structural point $(x_{s,i}, y_{s,i})$. To satisfy the boundary conditions at infinity, $\delta z(x, y)$ must be similar to a linear function, thus satisfying the total force and total moment conservation

$$\begin{aligned}\sum \mathcal{F}_i &= 0 \\ \sum x_i \mathcal{F}_i &= 0 \\ \sum y_i \mathcal{F}_i &= 0.\end{aligned}\tag{4.4}$$

From these equations the coefficients \mathcal{F}_i which give the known displacements at the structural nodes are calculated. These forces can then be used to determine the function δz , enabling the unknown displacements to be obtained at the aerodynamic points.

According to the equation of equilibrium, the IPS method takes into account only the bending of the structure, i.e movement in the direction orthogonal to the structure, and any compression or dilatation in the direction parallel to the structure is neglected. In addition if the aerodynamic and structural points do not lie on the same surface then a projection is used onto a neutral surface. The projected aerodynamic points are then displaced using the projected structural points and finally the aerodynamic points are recovered by adding the original offsets.

The relation between the displacements at N structural and M aerodynamic points is conveniently written in terms of a spline matrix. Writing in matrix form the equation(4.3), one gets:

$$\delta z(x, y) = [1, x, y, K_1(x, y), K_2(x, y), \dots, K_N(x, y)] \begin{bmatrix} a_0 \\ a_1 \\ a_2 \\ \mathcal{F}_1 \\ \mathcal{F}_2 \\ \cdot \\ \cdot \\ \mathcal{F}_N \end{bmatrix}\tag{4.5}$$

where $K_i(x, y) = r_i^2 \ln r_i^2$. Including the force and moment equations, and restricting the surface to pass through the structural points leads to the system

$$\begin{bmatrix} 0 \\ 0 \\ 0 \\ \delta z_{s,1} \\ \delta z_{s,2} \\ \vdots \\ \delta z_{s,N} \end{bmatrix} = \begin{bmatrix} 0 & 0 & 0 & 1 & \cdots & 1 \\ 0 & 0 & 0 & x_{s,1} & \cdots & x_{s,N} \\ 0 & 0 & 0 & y_{s,1} & \cdots & y_{s,N} \\ 1 & x_{s,1} & y_{s,1} & 0 & \cdots & K_{1,N}^s \\ 1 & x_{s,2} & y_{s,2} & K_{2,1}^s & \cdots & K_{2,N}^s \\ \vdots & \vdots & \vdots & \vdots & \cdots & \vdots \\ \vdots & \vdots & \vdots & \vdots & \cdots & \vdots \\ 1 & x_{s,N} & y_{s,N} & K_{N,1}^s & \cdots & 0 \end{bmatrix} \begin{bmatrix} a_0 \\ a_1 \\ a_2 \\ \mathcal{F}_1 \\ \mathcal{F}_2 \\ \vdots \\ \mathcal{F}_N \end{bmatrix} = [C][\mathcal{F}] \quad (4.6)$$

where $K_{i,j}^s$ denotes the function K_j evaluated at the i -th structural point and $\delta z_{s,i}$ is the displacement at the i -th structural point. This equation can be solved for the vector with components a_i and \mathcal{F}_i . The displacements at the M aerodynamic points can then be evaluated from

$$\begin{bmatrix} 0 \\ 0 \\ 0 \\ \delta z_{a,1} \\ \delta z_{a,2} \\ \vdots \\ \delta z_{a,M} \end{bmatrix} = \begin{bmatrix} 1 & x_{a,1} & y_{a,1} & K_{1,1}^a & K_{1,2}^a & \cdots & K_{1,N}^a \\ 1 & x_{a,2} & y_{a,2} & K_{2,1}^a & K_{2,2}^a & \cdots & K_{2,N}^a \\ \vdots & \vdots & \vdots & \vdots & \vdots & \cdots & \vdots \\ \vdots & \vdots & \vdots & \vdots & \vdots & \cdots & \vdots \\ 1 & x_{a,M} & y_{a,M} & K_{M,1}^a & K_{M,2}^a & \cdots & K_{M,N}^a \end{bmatrix} [C^{-1}] \begin{bmatrix} 0 \\ 0 \\ 0 \\ \delta z_1 \\ \delta z_2 \\ \vdots \\ \delta z_N \end{bmatrix} \quad (4.7)$$

where $K_{i,j}^a$ indicates the function K_j evaluated at the i -th aerodynamic point. A linear relationship

$$\delta \tilde{z}_a = \tilde{S} \delta \hat{z}_s \quad (4.8)$$

can be obtained by forming the matrix product on the right hand side of equation (4.7) and deleting the first three rows and columns. Note that this relation only gives out-of-plane displacements. If in-plane displacements are required then the same spline matrix is also applied for these. This implies that there is no coupling between displacements in different coordinate directions.

Next, we consider some of the properties of the IPS method. If the structure undergoes a unit translation at every point then $\delta z(x) = 1$ is the unique solution of the biharmonic equation with the boundary conditions at infinity. This means that the unit translation is also recovered at the aerodynamic points, as would be expected.

If the structural points are displaced according to a unit rigid rotation then we note that a unit rigid rotation represents also a solution of the plate equation. This can be seen by noting that for a rotation the displacements must be linear in x and y , which is automatically a solution of the plate equation with associated far field conditions. Hence, the aerodynamic points must also undergo the rotation, again as would be required. This is true when the spline has been calculated when the fluid and structure lie on the same plane. If the aerodynamic points do not lie on the structural surface, each aerodynamic point is linked to its projection onto the structural surface by a rigid bar. The normal displacements of the projected points are determined by IPS and the aerodynamic points are recovered by adding the rigid bars. Since the rigid rotation is not applied to the out-of-plane component, a rigid rotation applied to the structural points is not recovered for the aerodynamic points. Hence, the recovered aerodynamic profile will be distorted in this case.

4.2.2 Other Spline Based Methods

Other methods compatible with potential aerodynamic theories have been presented, and they follow closely the IPS. These are now briefly reviewed.

Multiquadric-Biharmonic

The method named Multiquadric-Biharmonic (MQ) method was proposed by Hardy [47]. MQ was used to perform interpolation in topography and the name reflects

the method's use of quadratic basis functions. The quadratic surface used in most cases is a hyperboloid of revolution in two sheets. The aerodynamic displacements are represented as a function

$$\delta z(x, y) = \sum_{i=1}^N c_i [(x - x_{s,i})^2 + (y - y_{s,i})^2 + \kappa]. \quad (4.9)$$

This equation should be compared with equation (4.3) for IPS. The coefficients c_i are determined by forcing agreement with the known displacements at the structural points. The user-defined parameter κ controls the shape of the basis functions. A large value for κ gives a flat sheet-like function, while a small value for κ gives a narrow cone-like function. For non-zero values of κ , MQ produces an infinitely differentiable function that preserves monotonicity and convexity.

Whereas IPS has a translation invariance property, MQ does not. To illustrate, consider the one-dimensional case, where the structure is represented by two nodes $(x_{s,1}, y_{s,1})^T$ and $(x_{s,2}, y_{s,2})^T$ which are given displacements $\delta z_{s,1} = 1$ and $\delta z_{s,2} = 1$. This represents a rigid translation of the aerodynamic grid by one unit. Due to the nonlinearity of equation 4.9 however, calculating the displacement at an aerodynamic point will not yield a unit value and so a distortion in the surface will be introduced. In reference [48] it was pointed out that MQ performs poorly in regions which are relatively flat when a rigid surface deforms during a rigid translation to a parabolic surface.

Thin Plate Spline(TPS)

Duchon [59] laid the groundwork for the thin plate spline(TPS). An irregular surface is represented by using functions that minimize an energy function. This method is very similar to the MQ method, the difference being in the basis functions which are

used,

$$\delta z(x, y) = \sum_{i=1}^N c_i r_i^2 \ln(r_i^2). \quad (4.10)$$

For a 1-D problem, cubic splines are interpreted as equilibrium positions of a beam undergoing bending deformation. For a 2-D problem, these splines can be determined from the minimization of the bending energy (thus defining the equilibrium position) of a thin plate, and thus are similar to the IPS. Since these splines are invariant with rotation and translation they are suitable for the interpolation of moving or flexible components [49]. The properties of shape preservation under translation and rotation are similar to IPS.

Finite Plate Spline

For the FPS, described by Guruswamy [50], a "virtual surface" is defined which does not necessarily pass through all the defined points. For known structural displacements the virtual surface displacement is calculated which then determines the aerodynamic displacements. The relationship between the virtual surface displacements and the structural displacements can be written

$$\delta \hat{\mathbf{x}}_s = \Psi_s \delta \hat{\mathbf{x}}_v \quad (4.11)$$

where $\hat{\mathbf{x}}_v$ is the vector of points on the virtual surface corresponding to the structural points $\hat{\mathbf{x}}_s$. Similarly the relationship between the virtual surface displacements and the aerodynamic displacements is

$$\delta \hat{\mathbf{x}}_a = \Psi_a \delta \hat{\mathbf{x}}_v \quad (4.12)$$

In practice the virtual surface is constrained to pass through the structural points, whose displacements are known. To find the matrix Ψ_a another condition is introduced, namely that at a steady-state, the potential energy π of the system is min-

imised. A constrained minimization problem in terms of the loads applied to the structure and properties of the virtual surface can then be solved.

Inverse Isoparametric Method(IIM)

In this method the aerodynamic point displacements are interpolated using the same shape functions used to approximate the deformation of the surface. To illustrate,

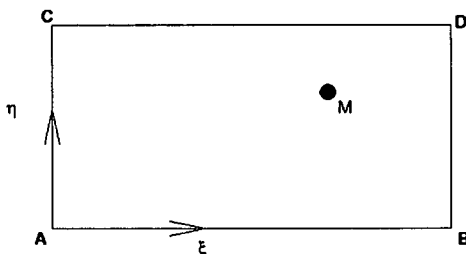


Figure 4.1: Inverse Isoparametric Element

the aerodynamic point M can be represented using shape functions as

$$\begin{aligned} x &= N_A(\xi, \eta)x_A + N_B(\xi, \eta)x_B + N_C(\xi, \eta)x_C + N_D(\xi, \eta)x_D \\ y &= N_A(\xi, \eta)y_A + N_B(\xi, \eta)y_B + N_C(\xi, \eta)y_C + N_D(\xi, \eta)y_D. \end{aligned} \quad (4.13)$$

For point M, the associated values of ξ and η can be determined and then the fluid point displacement is calculated by evaluating the same shape function for these values and using them to weight the known structural displacements. The limitation of the method is that the aerodynamic and structural points must lie on the same surface.

Summary of Review by Smith

In reference [48], a full literature survey was performed to determine the interpolation methods most suitable for aeroelastic calculations. The methods were selected from

aeroelasticity, physical sciences and engineering design (CAD). They were assessed in terms of accuracy, ease of use, robustness and cost-effectiveness.

Three methods were retained for a follow-on paper which appeared three years later [49]. These were IPS, TPS and MQ. These methods were evaluated for the 445.6 wing, an engine liner and a space shuttle test case.

The first case presented was on the 445.6 wing. This wing interpolation was assumed to involve only out-of-plane displacements. The TPS and MQ methods yielded good results. However the IPS method was found to give oscillations which perhaps indicates a problem of implementation.

The second case performed was the engine liner. It was found that MQ performed poorly and that the TPS had the same significant distortions when used unscaled. However, it was claimed that applying *scaling* to the methods yielded good results, although it was never explained what this means. For the IPS method, three splines were needed and problems were seen in joining these splines.

For the lifting body test case (space shuttle), it was found that results could be improved for the IPS by modifying the implementation, although again the details were not given. Otherwise the MQ and TPS performed well. These results were confirmed for an F-16 wing interpolation.

In conclusion, it was asserted that the best methods were the MQ and TPS, when scaled. It was also recognised that aeroelastic calculations should be performed using different interpolation methods to see their effects.

Brown interpolation method

An attempt to tackle the problem by introducing virtual elements between the structural and the fluid meshes for three dimensional configurations was given in Brown[51]. The idea resulted from consideration of an airfoil beam structural model. It was noted

that points originally perpendicular to the beam stay perpendicular and that their distances stay constant. This allows the extrapolation for the aerodynamic profile to be done by rigidly rotating the aerodynamic points as a function of the rotation of associated structural points. To generalise the method in three dimensions, virtual finite elements were introduced, which do not add mass or stiffness to the problem because they are solely used for displacement interpolations. However, it has been suggested that the addition of virtual elements is an unnecessary complication, particularly for complex geometries by Cebal and Lohner [52].

4.3 Weighted Residual Based Methods

4.3.1 Method of Chen

To overcome the shape distortion problem often associated with spline based methods an interpolation method based on the boundary element method (BEM) was proposed in reference Chen and Jadic [53]. The BEM is used in conjunction with structural potential energy minimisation and the spline matrix is built by assuming that the structure is at equilibrium and the potential energy is minimised, requiring the stiffness matrix. The use of the BEM instead of the finite element method allows the problem to be tackled when the fluid and structural surfaces are not co-incident. But because the number of structural nodes is often less than the number of aerodynamic surface nodes, building a displacement interpolation method leads to a system of equations which has less equations than unknowns. In order to have a well posed problem the condition of minimum potential energy is introduced. Demonstrations of the method were performed for two dimensional problems in reference [53].

In figure 4.2, the fluid points lie on the real structural surface, and the internal points are used to represent the structural points used in the modelling. For the

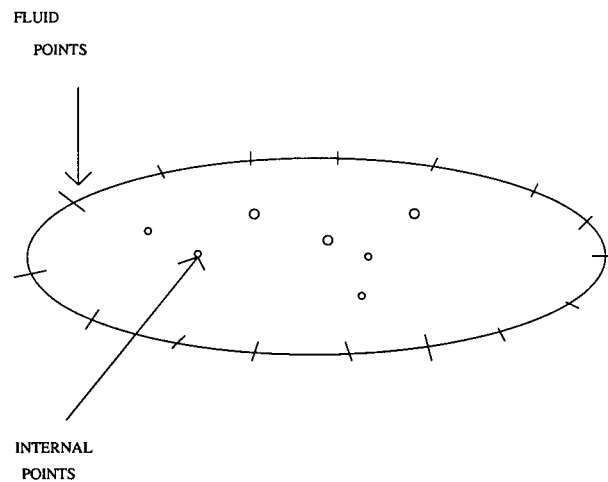


Figure 4.2: Structural BEM problem

BEM interfacing, the fluid points, $\hat{\mathbf{x}}_f$, are represented as the boundary points, and the structural ones, $\hat{\mathbf{x}}_s$ as the internal points. Note here that in common with the BEM literature the displacements on these grids are denoted by the symbol \mathbf{u} in this section.

Writing the BEM for the internal structural points leads to the relation

$$\mathbf{u}_s = \mathbf{G}_{bi}\mathbf{p}_f - \mathbf{H}_{bi}\mathbf{u}_f. \quad (4.14)$$

Here the notation for the BEM matrices follows the description given in chapter 3.

For the boundary points

$$\mathbf{G}\mathbf{p}_f = \mathbf{H}\mathbf{u}_f. \quad (4.15)$$

Substitution of this last equation into equation 4.14 yields

$$\mathbf{u}_s = (\mathbf{G}_{bi}\mathbf{G}^{-1}\mathbf{H} - \mathbf{H}_{bi})\mathbf{u}_f. \quad (4.16)$$

Three cases need to be considered. If the number of internal points is equal to the number of boundary points, the system can be inverted. If the number is greater then

a least squares solution is used. If the number is lower then additional conditions are required to solve the system and in this case the strain energy is minimised.

Denote the strain energy by $\mathcal{E} = \int_{\Gamma} \mathbf{p}_{f,k} \mathbf{u}_{f,k} d\Gamma$ where Γ designates the fluid boundary, and the indices k the three spatial directions. In matrix form the strain energy is written as $\mathcal{E} = \mathbf{u}_f^T \mathbf{R}_a \mathbf{p}_f$ where \mathbf{R}_a is a matrix containing the areas of the boundary elements. Using the equation (4.14) and defining $\mathcal{A} = \mathbf{R}_a \mathbf{H}^{-1} \mathbf{G}$, then $\mathcal{E} = \mathbf{u}_f^T \mathcal{A} \mathbf{u}_f$. Finally, the strain energy can be written as

$$\mathcal{E} = \mathbf{u}_f^T \mathbf{R}_f \mathbf{G}^{-1} \mathbf{H} \mathbf{u}_f. \quad (4.17)$$

A Lagrange multiplier technique is then used to minimise the energy. The objective function is defined as $F = \mathbf{u}_f^T \mathcal{A} \mathbf{u}_f - \boldsymbol{\lambda}^T (\mathbf{u}_s - \mathbf{u}_{s,given})$, where $\boldsymbol{\lambda}$ and $\mathbf{u}_{s,given}$ are the vector of Lagrange multipliers and the given structural displacements respectively. Solving the system

$$\begin{aligned} \frac{\partial F}{\partial \mathbf{u}_f} &= 0 \\ \mathbf{u}_s &= \mathbf{u} - \mathbf{u}_{s,given} \end{aligned} \quad (4.18)$$

leads to the spline matrix $\mathbf{u}_f = \hat{\mathbf{S}} \mathbf{u}_s$. The transpose of the spline matrix is taken in order to get the force transformation matrix.

The method was improved by Chen and Hill [54] by introducing a virtual BEM mesh, as shown in figure 4.3. The BEM mesh is defined to contain the fluid and structural nodes. So considering the BEM mesh as the external mesh and the fluid mesh as the internal mesh one has

$$\mathbf{u}_f = \mathbf{B} \mathbf{u}_{BEM} \quad (4.19)$$

and for the structural mesh

$$\mathbf{u}_{BEM} = \mathbf{C} \mathbf{u}_s. \quad (4.20)$$

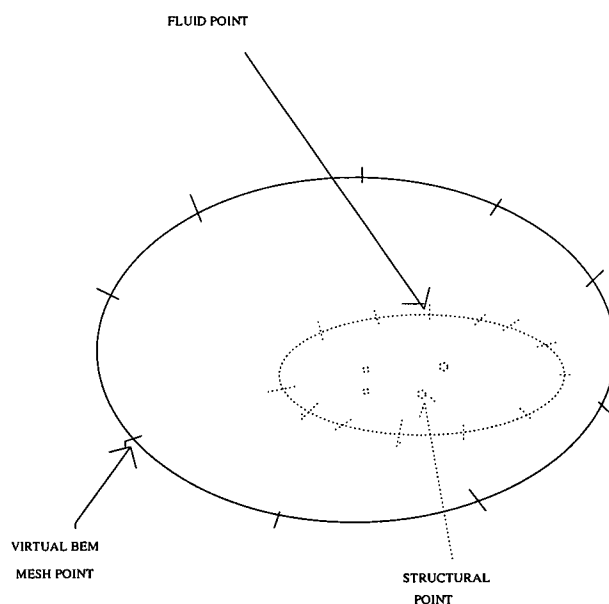


Figure 4.3: Virtual BEM method

Hence the relation between the fluid and structural points is

$$\mathbf{u}_f = \mathbf{BCu}_s. \quad (4.21)$$

The performance of the original and modified Chen methods is evaluated in the next chapter.

4.3.2 Methods of Lohner and Cebal

The method described by Lohner and co-workers [55] consists of two parts, the in-plane and out-of-plane interpolation. For the in-plane motion, the method first considers the exchange of information in terms of pressures. The fluid pressure distribution is defined on a coarse fluid mesh and features a shock. The problem is to interpolate the pressure defined on the fluid grid to the structural grid. The fluid and structural grids lie on the same surface but are not coincident, as shown in figure 4.4.

Using a point wise interpolation, the pressure shock is not interpolated correctly.

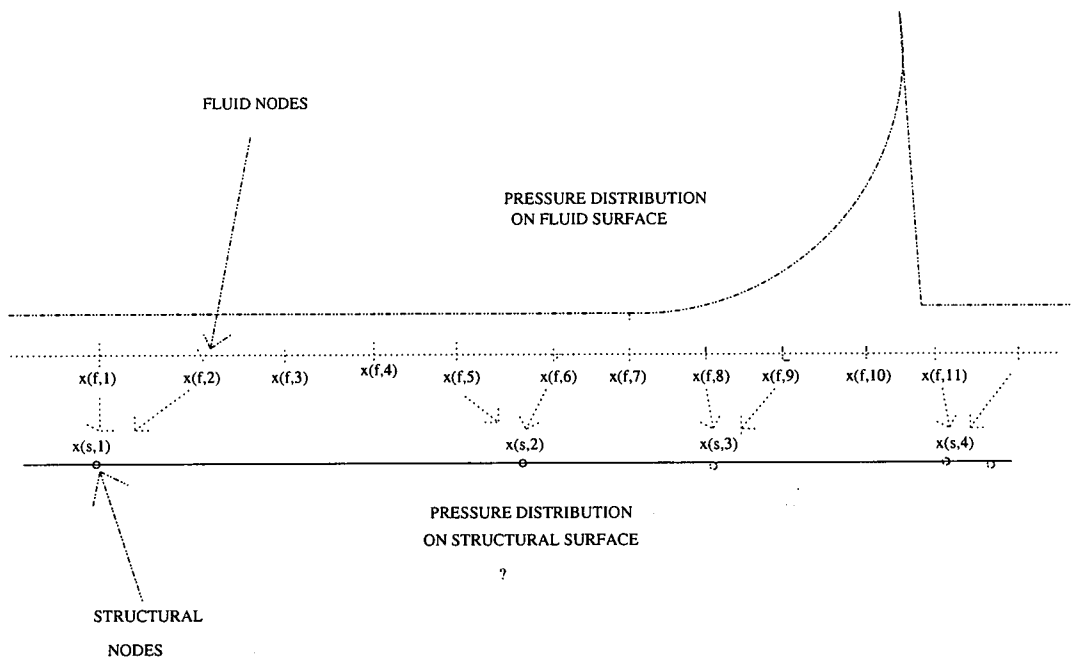


Figure 4.4: Pressure interpolation

The method defines the interpolation so that $p_s(x) = p_f(x)$. Interpolating the pressures with the help of shape functions gives $p_s(x) = N_s^i p_{i,s}$ for the pressure on the structural surface, and $p_f(x) = N_f^j p_{j,f}$ for the pressure on the fluid surface. For illustration, constant shape functions give

$$\begin{aligned} p_s(x) &= 0, x \notin [x_{s,i-1}, x_{s,i}] & p_s(x) &= p_{s,i}(x), x \in [x_{s,i-1}, x_{s,i}] \\ p_f(x) &= 0, x \notin [x_{f,i-1}, x_{f,i}] & p_f(x) &= p_{f,i}(x), x \in [x_{f,i-1}, x_{f,i}]. \end{aligned} \quad (4.22)$$

Using the shape functions as weights the pressure equality can be expressed in integral form as

$$\int_{Interface} N_s^i N_s^j p_{j,s} d\Gamma = \int_{Interface} N_s^i N_f^j p_{j,f} d\Gamma. \quad (4.23)$$

This form, similar to a weighted residual, leads to a matrix system:

$$\mathbf{M}_s \tilde{\mathbf{p}}_s = \mathbf{M}_f \tilde{\mathbf{p}}_f. \quad (4.24)$$

Using constant shape functions from a force point of view is equivalent to a linear

interpolation.

When the fluid and structure meshes are offset, a surface tracking method with distance vectors is performed. The distance vectors are rotated according to the rotations of the normals to the deforming CFD mesh. In Cebal [56] it is stated that *“For the case of reduced models or models with incompatible dimensionalities, it is still not clear if the rotation of the distance vector is enough”* and *“Treatment of reduced models or models with incompatible dimensionalities, in particular, the surface tracking algorithms that ensure work or energy conservation”* is listed as a future development of the method. This method is in fact an inverse isoparametric method using linear shape functions and supposes that any out-of-plane motion is a rigid rotation. The limitations of this assumption will become clear when the CVT method is presented in the next chapter.

Chapter 5 : Analysis of Transfer Methods

With the growth in multi-disciplinary simulation, the problem of coupling fluid and structural dynamics codes has attracted increasing interest. Most approaches were designed for the case where the fluid is modelled by a linear method which allows the true geometry to be simplified to a plate, consistent with the structural dynamics model. The transformation in this case can be based on scalar splines for the in-plane displacement. With the advent of higher levels of fluid modelling, which require a grid that conforms to the aerodynamic surfaces, new transformation procedures are needed.

A new transformation method between a structural surface grid and a fluid surface grid is proposed and analysed in the current chapter. The transformation is local and is based on a volume conservation property. The method is analysed for conservation properties which are identified as being important in airframe aeroelasticity. The method properties are contrasted with other transformation method, the IPS and BEM methods, which were described in the preceding chapter.

5.1 Transformation Methods

5.1.1 The Constant Volume Tetrahedron Transformation

The CVT method for the position of a fluid surface grid point is local in the sense that it only relies on information obtained from one element constructed from the

surface structural mesh. The first stage is to identify fluid grid points with structural grid points. Denote the fluid grid point under consideration by $\mathbf{x}_{a,l}(t)$. A search is carried out over the structural surface points to locate the nearest three points $\mathbf{x}_{s,i}(t)$, $\mathbf{x}_{s,j}(t)$, $\mathbf{x}_{s,k}(t)$ which form a triangle (see figure 5.1).

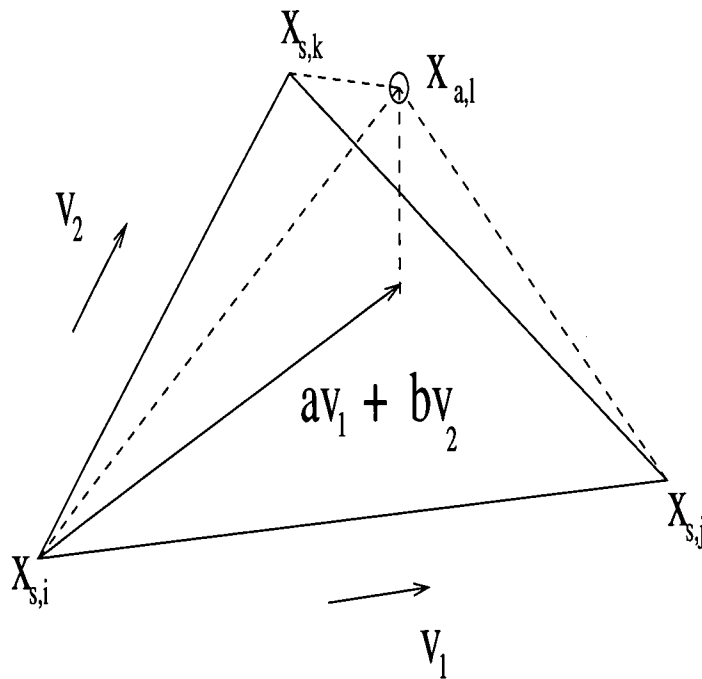


Figure 5.1: Interpolation from structural mesh to fluid mesh.

Once the fluid point has been associated with a structural surface element the position of $\mathbf{x}_{a,l}$ is expressed as

$$\mathbf{c} = \alpha \mathbf{a} + \beta \mathbf{b} + \gamma \mathbf{d} \quad (5.1)$$

where $\mathbf{a} = \mathbf{x}_{s,j} - \mathbf{x}_{s,i}$, $\mathbf{b} = \mathbf{x}_{s,k} - \mathbf{x}_{s,i}$, $\mathbf{c} = \mathbf{x}_{a,l} - \mathbf{x}_{s,i}$ and $\mathbf{d} = \mathbf{a} \times \mathbf{b}$. The parameters α , β and γ are computed from

$$\alpha = \frac{|\mathbf{b}|^2(\mathbf{a} \cdot \mathbf{c}) - (\mathbf{a} \cdot \mathbf{c})(\mathbf{b} \cdot \mathbf{c})}{|\mathbf{d}|^2} \quad (5.2)$$

$$\beta = \frac{|\mathbf{a}|^2(\mathbf{b} \cdot \mathbf{c}) - (\mathbf{a} \cdot \mathbf{b})(\mathbf{a} \cdot \mathbf{c})}{|\mathbf{d}|^2} \quad (5.3)$$

$$\gamma = \frac{(\mathbf{c} \cdot \mathbf{d})}{|\mathbf{d}|^2}. \quad (5.4)$$

Here, the term $\alpha\mathbf{a} + \beta\mathbf{b}$ denotes the component of $\mathbf{x}_{a,l}$ in the plane of the structural points and $\gamma\mathbf{d}$ the component normal to the plane. The volume of the tetrahedral element formed by the three structural and one aerodynamic points is given by the triple product

$$V = (\mathbf{a} \cdot \mathbf{b} \times \mathbf{c})/4 \quad (5.5)$$

which remains constant if the displaced fluid grid position is calculated from

$$\mathbf{x}_{a,l} = \mathbf{x}_{s,i}(t) + \alpha\mathbf{a}(t) + \beta\mathbf{b}(t) + \gamma(t)\mathbf{d}(t) \quad (5.6)$$

where α and β are fixed at their initial values and

$$\gamma(t) = \frac{|\mathbf{d}(0)|^2}{|\mathbf{d}(t)|^2}\gamma(0). \quad (5.7)$$

This expression means that the projection of the fluid point onto the plane of the structural points moves linearly with the structural points whereas the out of plane component is chosen to conserve the volume of the tetrahedron. If the fluid and structural points are planar then the expression reduces to linear interpolation for the position of the fluid point.

It proves useful for defining force transformations to have a linear relationship between fluid and structural grid displacements. Equation (5.6) can be linearised in the structural displacements, giving

$$\delta\mathbf{x}_{a,l} = \mathbf{A}\delta\mathbf{x}_{s,i} + \mathbf{B}\delta\mathbf{x}_{s,j} + \mathbf{C}\delta\mathbf{x}_{s,k} \quad (5.8)$$

where $\mathbf{A} = \mathbf{I} - \mathbf{B} - \mathbf{C}$, $\mathbf{B} = \alpha\mathbf{I} - \gamma\mathcal{UV}(\mathbf{b})$ and $\mathbf{C} = \beta\mathbf{I} + \gamma\mathcal{UV}(\mathbf{a})$. Here

$$\mathbf{U} = \mathbf{I} - \frac{2}{d^2}\mathcal{D}(\mathbf{d})\mathcal{S}(\mathbf{d}) \quad (5.9)$$

$$\mathcal{V}(\mathbf{z}) = \begin{bmatrix} 0 & -z_3 & z_2 \\ z_3 & 0 & -z_1 \\ -z_2 & z_1 & 0 \end{bmatrix}, \quad (5.10)$$

$$\mathcal{D}(\mathbf{z}) = \begin{bmatrix} z_1 & 0 & 0 \\ 0 & z_2 & 0 \\ 0 & 0 & z_3 \end{bmatrix} \quad (5.11)$$

$$\mathcal{S}(\mathbf{z}) = \begin{bmatrix} z_1 & z_2 & z_3 \\ z_1 & z_2 & z_3 \\ z_1 & z_2 & z_3 \end{bmatrix}. \quad (5.12)$$

The linear relationship can also be expressed in the form $\delta \mathbf{c} = \mathbf{B}\delta \mathbf{a} + \mathbf{C}\delta \mathbf{b}$. For all of these expressions the matrices are evaluated at the initial values of \mathbf{a} , \mathbf{b} and \mathbf{c} .

The two-dimensional version of the method is now described here along with a complex variable form. In the special case of two dimensional problems the linear form of the CVT method can be written as

$$\delta \mathbf{x}_{a,l} = \mathbf{A}\delta \mathbf{x}_{s,i} + \mathbf{B}\delta \mathbf{x}_{s,j} \quad (5.13)$$

where

$$\mathbf{A} = \begin{bmatrix} 1 - \alpha & \gamma \\ -\gamma & 1 - \alpha \end{bmatrix}. \quad (5.14)$$

$$\mathbf{B} = \begin{bmatrix} \alpha & -\gamma \\ \gamma & \alpha \end{bmatrix}. \quad (5.15)$$

Here the constants α and γ are calculated from the initial decomposition of $\mathbf{x}_{a,l}$ into a component in the direction of the structural points $\mathbf{x}_{s,i} - \mathbf{x}_{s,j}$ and a component normal to this direction \mathbf{d} , given by

$$\mathbf{x}_{a,l} - \mathbf{x}_{s,i} = \alpha(\mathbf{x}_{s,j} - \mathbf{x}_{s,i}) + \gamma \mathbf{d}. \quad (5.16)$$

This expression is simpler than the three dimensional case since in two dimensions the displaced normal direction \mathbf{d} is a linear expression of the structural points ($\mathbf{d} = \mathbf{k} \times (\mathbf{x}_{s,j} - \mathbf{x}_{s,i})$ where \mathbf{k} is the normal vector to the plane of the points), but is a nonlinear expression in three dimensions ($\mathbf{d} = (\mathbf{x}_{s,j} - \mathbf{x}_{s,i}) \times (\mathbf{x}_{s,k} - \mathbf{x}_{s,i})$).

We express also the method in complex notation for the two dimensional cases. This formulation will be used for demonstrating invariance properties. If the position of a point (x, y) is represented by the complex number $x + iy$ then properties of complex numbers can be used to prove rotational invariance. Adopting the notation that the fluid point is at ζ_a and the two associated structural points are at $\zeta_{s,i}$ and $\zeta_{s,j}$ with $\zeta_{ij} = \zeta_{s,j} - \zeta_{s,i}$ then the nonlinear CVT method can be written as

$$\zeta_a = (1 - \alpha)\zeta_{s,i} + \alpha\zeta_{s,j} + \delta i\zeta_{ij} \quad (5.17)$$

where α and δ are real. The vector associated with $i\zeta_{ij}$ is orthogonal to the one associated with ζ_{ij} . The linearised form in complex notation is

$$\delta\zeta_a = (1 - \alpha - i\gamma)\delta\zeta_{s,i} + (\alpha + i\gamma)\delta\zeta_{s,j} \quad (5.18)$$

where α and γ are fixed at their initial values.

5.1.2 Spline Based Transformation Methods

We summarise here the characteristics of the spline based methods which will help the understanding of the ideas behind the CVT.

Commonly used transformation methods rely on projection, interpolation and recovery. The CVT method described in the last section uses volume conservation and angle preservation principles for the projection and recovery stages. The interpolation phase is done using linear interpolation.

In contrast, the projection and recovery steps for transformation methods designed for plate aerodynamics assume constant out-of-plane vectors. Using the notation from the previous section, the displacements of projected aerodynamic points $\hat{\mathbf{x}}_p$ onto the plane of the structural points are calculated from

$$\delta\tilde{\mathbf{x}}_p = \tilde{\mathbf{S}}\delta\tilde{\mathbf{x}}_s \quad (5.19)$$

$$\delta\tilde{\mathbf{y}}_p = \tilde{\mathbf{S}}\delta\tilde{\mathbf{y}}_s \quad (5.20)$$

$$\delta\tilde{\mathbf{z}}_p = \tilde{\mathbf{S}}\delta\tilde{\mathbf{z}}_s \quad (5.21)$$

and then the displaced aerodynamic points from

$$\delta\hat{\mathbf{x}}_a = \delta\hat{\mathbf{x}}_p. \quad (5.22)$$

If we write $\mathbf{x}_a = \mathbf{x}_p + \mathbf{d}_0$ then the transformation maintains a constant out-of-plane component \mathbf{d}_0 . The matrices $\tilde{\mathbf{S}}$ are calculated from equation (4.8). Note that these matrices are calculated for the out-of-plane displacement but are then applied for the in-plane displacements also. To obtain the consolidated for of the three dimensional transformation

$$\delta\hat{\mathbf{x}}_a = \hat{\mathbf{S}}\delta\hat{\mathbf{x}}_s \quad (5.23)$$

the matrix $\hat{\mathbf{S}} = [\hat{\mathbf{S}}_{ij}]$, where $\hat{\mathbf{S}}_{ij}$ are 3x3 blocks is defined by

$$\hat{\mathbf{S}}_{ij} = \begin{bmatrix} \tilde{\mathbf{S}}_{ij} & 0 & 0 \\ 0 & \tilde{\mathbf{S}}_{ij} & 0 \\ 0 & 0 & \tilde{\mathbf{S}}_{ij} \end{bmatrix} \quad (5.24)$$

where $\tilde{\mathbf{S}} = [\tilde{\mathbf{S}}_{ij}]$.

The method used for the comparisons shown in this chapter is IPS.

5.2 Translational and Rotational Shape Preservation

The nature of one of the most common aeroelastic instabilities which an airframe encounters is torsion-bending flutter, involving torsion and bending modes. Rotation (for torsion) and translation (for bending) are therefore important component motions. A desirable property for a transformation method is that it should be able to reproduce a translation or rotation in the aerodynamic grid when one of these is applied to the structural grid.

5.2.1 Translation

If the transformation is linear of the form

$$\delta \hat{\mathbf{x}}_a = \hat{\mathbf{S}} \delta \hat{\mathbf{x}}_s \quad (5.25)$$

a translation is reproduced on the aerodynamic grid if

$$\hat{\mathbf{S}} \hat{\mathbf{h}} = \hat{\mathbf{h}} \quad (5.26)$$

for every vector $\hat{\mathbf{h}}$ which can be partitioned so that

$$\hat{\mathbf{h}} = [\mathbf{h}_s, \mathbf{h}_s, \dots, \mathbf{h}_s]^\top \quad (5.27)$$

where \mathbf{h}_s is a three component vector of position.

For the linearised CVT method, in three dimensions, $\mathbf{A} = \mathbf{I} - \mathbf{B} - \mathbf{C}$ and hence

$$\mathbf{A}\mathbf{h}_s + \mathbf{B}\mathbf{h}_s + \mathbf{C}\mathbf{h}_s = (\mathbf{A} + \mathbf{B} + \mathbf{C})\mathbf{h}_s = \mathbf{h}_s. \quad (5.28)$$

For the IPS method the transformation recovers a translation due to the properties of the thin-plate solution used to define the matrices $\tilde{\mathbf{S}}$. The rigid projection does not disrupt this.

5.2.2 Rotation

Two dimensions

We first prove here that the CVT method is invariant under rigid rotation in two dimensions, before presenting the demonstration for the three dimensional case.

The displacement $\delta \mathbf{x}_{s,i}$ of a point $\mathbf{x}_{s,i}$ caused by a rigid rotation through an angle θ about the origin can be written as

$$\delta \mathbf{x}_{s,i} = \mathbf{R} \mathbf{x}_{s,i} \quad (5.29)$$

where

$$\mathbf{R} = \begin{bmatrix} \cos \theta & -\sin \theta \\ \sin \theta & \cos \theta \end{bmatrix}. \quad (5.30)$$

A simple calculation shows that if two matrices satisfy $\mathbf{A} = -\mathbf{A}^T$ and $\mathbf{B} = -\mathbf{B}^T$, then $\mathbf{AB} = \mathbf{BA}$. Since $\mathbf{A}_1 = -\mathbf{A}_1^T$, $\mathbf{A}_2 = -\mathbf{A}_2^T$ and $\mathbf{R} = -\mathbf{R}^T$, it follows that $\mathbf{A}_1\mathbf{R} + \mathbf{A}_2\mathbf{R} = \mathbf{R}(\mathbf{A}_1 + \mathbf{A}_2)$ and so the displacement of the aerodynamic point which is interpolated from a rigid rotation applied to the structural points is $\delta\mathbf{x}_a = \mathbf{R}\mathbf{x}_a$. Hence the transformation is invariant under rotation.

Using the complex formulation, the displacement of point ζ_1 due to a rotation through an angle θ is given by $\delta\zeta_1 = e^{i\theta}\zeta_1$. Then, applying a rigid rotation to the structural points implies that

$$\delta\zeta_a = e^{i\theta}((1 - \alpha - i\gamma)\delta\zeta_2 + (\alpha + i\gamma)\delta\zeta_2) = e^{i\theta}\zeta_a.$$

Hence the two-dimensional linear transformation recovers rigid rotations.

Three Dimensions

The analysis of this section follows the approach laid out by Jonathan Smith of BAE SYSTEMS in private communications with the author.

The rotation through an angle θ about an axis parallel to the vector \mathbf{n} can be written in the form $\mathbf{x} = \mathbf{R}\mathbf{x}_0$ where $\mathbf{R} = \mathbf{R}_0\mathbf{R}_x\mathbf{R}_0^T$. Here

$$\mathbf{R}_0 = \begin{bmatrix} \cos \Xi \cos \Theta & -\sin \Theta & \sin \Xi \cos \Theta \\ \cos \Xi \sin \Theta & \cos \Theta & \sin \Xi \sin \Theta \\ -\sin \Xi & 0 & \cos \Xi \end{bmatrix} \quad (5.31)$$

where Θ and Ξ are angles defining the direction of the axis and

$$\mathbf{R}_x = \begin{bmatrix} 1 & 0 & 0 \\ 0 & \cos \theta & -\sin \theta \\ 0 & \sin \theta & \cos \theta \end{bmatrix}. \quad (5.32)$$

Expanding \mathbf{R} in a Taylor series in θ gives

$$\mathbf{R} = I + (\mathbf{R}_0\mathbf{R}_x\mathbf{R}_0^T)\theta + O(\theta^2) \quad (5.33)$$

which to first order in θ is $\mathbf{R} = (I + \mathbf{T})$ where $\mathbf{T} = -\mathbf{T}^T$. Hence the rotation can be written as $\mathbf{x} = (I + \mathbf{T})\mathbf{x}_0$. For a matrix of the form $\mathbf{T} = -\mathbf{T}^T$, there exists a vector $\boldsymbol{\omega}$ such that $\mathbf{T}\mathbf{x} = \boldsymbol{\omega} \times \mathbf{x}$. Hence, to first order in the rotation angle, the displacement $\delta\mathbf{x}$ of a point at position \mathbf{x} due to the rotation is $\delta\mathbf{x} = \boldsymbol{\omega} \times \mathbf{x}$.

Applying a rotation to the structural points, the linear CVT method can be written as

$$\delta\mathbf{c} = \mathbf{B}\delta\mathbf{a} + \mathbf{C}\delta\mathbf{b} \quad (5.34)$$

where $\delta\mathbf{a} = \boldsymbol{\omega} \times \mathbf{a}$ and $\delta\mathbf{b} = \boldsymbol{\omega} \times \mathbf{b}$. Noting that $\mathcal{V}(\mathbf{a})\mathbf{b} = \mathbf{a} \times \mathbf{b}$ since $\mathcal{V}^T = -\mathcal{V}$ and $\mathcal{D}(\mathbf{a})\mathcal{S}(\mathbf{b})\mathbf{c} = (\mathbf{b} \cdot \mathbf{c})\mathbf{a}$, it follows that

$$\mathbf{B}\delta\mathbf{a} = \alpha\boldsymbol{\omega} \times \mathbf{a} - \gamma\mathbf{b} \times (\boldsymbol{\omega} \times \mathbf{a}) + \frac{2\gamma\mathbf{d}}{d^2}(\mathbf{d} \cdot (\mathbf{b} \times (\boldsymbol{\omega} \times \mathbf{a}))). \quad (5.35)$$

Now, $\mathbf{b} \times (\boldsymbol{\omega} \times \mathbf{a}) = (\mathbf{b} \cdot \mathbf{a})\boldsymbol{\omega} - (\mathbf{b} \cdot \boldsymbol{\omega})\mathbf{a}$ and $(\mathbf{d} \cdot \mathbf{a}) = (\mathbf{d} \cdot \mathbf{b}) = 0$ since $\mathbf{d} = \mathbf{a} \times \mathbf{b}$, this expression simplifies to

$$\mathbf{B}\delta\mathbf{a} = \alpha\boldsymbol{\omega} \times \mathbf{a} - \gamma\mathbf{b} \times (\boldsymbol{\omega} \times \mathbf{a}) + \frac{2\gamma\mathbf{d}}{d^2}((\mathbf{d} \cdot \boldsymbol{\omega})(\mathbf{b} \cdot \mathbf{a})). \quad (5.36)$$

Similarly,

$$\mathbf{C}\delta\mathbf{b} = \alpha\boldsymbol{\omega} \times \mathbf{b} + \gamma\mathbf{a} \times (\boldsymbol{\omega} \times \mathbf{b}) - \frac{2\gamma\mathbf{d}}{d^2}((\mathbf{d} \cdot \boldsymbol{\omega})(\mathbf{b} \cdot \mathbf{a})). \quad (5.37)$$

Hence,

$$\mathbf{B}\delta\mathbf{a} + \mathbf{C}\delta\mathbf{b} = \alpha\boldsymbol{\omega} \times \mathbf{a} + \beta\boldsymbol{\omega} \times \mathbf{b} - \gamma\mathbf{b} \times (\boldsymbol{\omega} \times \mathbf{a}) + \gamma\mathbf{a} \times (\boldsymbol{\omega} \times \mathbf{b}). \quad (5.38)$$

Using the identity for the vector products it follows that

$$\mathbf{a} \times (\boldsymbol{\omega} \times \mathbf{b}) - \mathbf{b} \times (\boldsymbol{\omega} \times \mathbf{a}) = \boldsymbol{\omega} \times (\mathbf{a} \times \mathbf{b}) \quad (5.39)$$

and hence

$$\mathbf{B}\delta\mathbf{a} + \mathbf{C}\delta\mathbf{b} = \alpha\boldsymbol{\omega} \times \mathbf{a} + \beta\boldsymbol{\omega} \times \mathbf{b} + \gamma\boldsymbol{\omega} \times \mathbf{d} = \boldsymbol{\omega} \times \mathbf{c}. \quad (5.40)$$

In other words, the linear CVT method applied to a linearised rotation of the structural grid returns the same linearised rotation applied to the fluid grid.

For IPS, the influence of the constant projection vector means that this type of method cannot be invariant under a rotation since the rotation is not applied to \mathbf{d}_0 . Setting $\delta\hat{\mathbf{x}}_s = \hat{\mathbf{R}}\hat{\mathbf{x}}_s$, the error incurred in recovering a rigid rotation is

$$\delta\hat{\mathbf{x}}_a - \hat{\mathbf{R}}\hat{\mathbf{x}}_a = \hat{\mathbf{S}}\hat{\mathbf{R}}\hat{\mathbf{x}}_s - \hat{\mathbf{R}}(\hat{\mathbf{x}}_p + \mathbf{d}_0) \quad (5.41)$$

and noting that $\hat{\mathbf{S}}\hat{\mathbf{R}} = \hat{\mathbf{R}}\hat{\mathbf{S}}$ since the matrix $\hat{\mathbf{R}}$ is block diagonal and the blocks of $\hat{\mathbf{S}}$ are diagonal,

$$\delta\mathbf{x}_a - \hat{\mathbf{R}}\mathbf{x}_a = -\hat{\mathbf{R}}\mathbf{d}_0. \quad (5.42)$$

Hence, the magnitude of this error increases linearly with θ for small values of the rotation angle.

5.3 Forces

A coupled simulation also requires the transformation of forces. The principle of virtual work can be applied to define the force transformation from the fluid to the structural grid in terms of the linearised displacement transformation

$$\delta\hat{\mathbf{x}}_a^T \hat{\mathbf{f}}_a = \delta\hat{\mathbf{x}}_s^T \hat{\mathbf{f}}_s \quad (5.43)$$

where $\hat{\mathbf{f}}_a$ and $\hat{\mathbf{f}}_s$ are the forces at the fluid and structural grid points respectively. This yields

$$\hat{\mathbf{f}}_s = \hat{\mathbf{S}}^T \hat{\mathbf{f}}_a. \quad (5.44)$$

The condition of conserved virtual work is a global one. It is also interesting to examine behaviour at the local level. Taking one CVT tetrahedron, the force at the aerodynamic point $\mathbf{f}_{a,l}$ is distributed to forces $\mathbf{f}_{s,i}$, $\mathbf{f}_{s,j}$ and $\mathbf{f}_{s,k}$ at the structural points

according to $\mathbf{f}_{s,i} = \mathbf{A}^T \mathbf{f}_{a,l}$, $\mathbf{f}_{s,j} = \mathbf{B}^T \mathbf{f}_{a,l}$ and $\mathbf{f}_{s,k} = \mathbf{C}^T \mathbf{f}_{a,l}$. Since $\mathbf{A} = \mathbf{I} - \mathbf{B} - \mathbf{C}$, it follows that $\mathbf{f}_{s,i} + \mathbf{f}_{s,j} + \mathbf{f}_{s,k} = \mathbf{f}_{a,l}$.

Considering the structural moment about point $\mathbf{x}_{s,i}$,

$$\mathbf{m} = \mathbf{a} \times \mathbf{f}_{s,j} + \mathbf{b} \times \mathbf{f}_{s,k} = \mathbf{a} \times \mathbf{B}^T \mathbf{f}_{a,l} + \mathbf{b} \times \mathbf{C}^T \mathbf{f}_{a,l}. \quad (5.45)$$

Applying a similar argument to that used to show rotational invariance, this expression simplifies to

$$\mathbf{m} = (\alpha \mathbf{a} + \beta \mathbf{b} + \gamma \mathbf{d}) \times \mathbf{f}_{a,l} = \mathbf{c} \times \mathbf{f}_{a,l} \quad (5.46)$$

which shows that the moment is conserved by the initial transformation of forces.

The total force and moment are conserved by IPS through the conditions applied to obtain a closed system for the weights of the basic thin-plate solutions. However, no local properties are available.

5.4 Representation of Structural Behaviour

Transformation methods attempt to recover structural dynamic responses from information at a limited number of points. For IPS this is done by constructing a solution to the thin-plate equations which passes through the known points. An error is incurred by the projection of the known and unknown points onto the common thin-plate and the neglect of thickness effects.

The CVT method constructs control volumes in the structure which involve one unknown point and three known points. Conservation of volume restricts the unknown point to a surface. To choose the correct point on this surface the deformation of the control volume is required. For wing aeroelastic examples the known points are likely to lie in a plane, with the unknown points being on a surface which is roughly parallel to this plane (consider a wing modelled by a plate structural model). The significant local forces for high Reynolds' number flow are normal to these surfaces.

To change the angle of projection of the unknown point onto the plane of the known point, there needs to be a significant internal force in the plane of the known points. Given that the externally applied forces are normal to this plane, this type of deformation seems unlikely. Hence, the choice in the CVT method to keep the projection angle fixed appears justified for this particular case.

5.5 Evaluation of CVT and IPS

To illustrate the behaviour of the CVT and IPS transformations we first consider two-dimensional examples where it is easy to view and interpret the results. We shall apply a rigid rotation to a plate representation of the geometry and then calculate the recovered position of the fluid grid which lies on the true geometry. For these cases the analysis presented above predicts that the error in the recovered fluid grid points is zero for the CVT method and increases linearly with the rotation angle for IPS.

First, consider the deformation of a circle. The initial and rotated shapes are shown in figure 5.2.

The linear CVT transformation recovered fluid points preserve the shape of the circle exactly for any rotation angle and are not shown. The IPS recovered shape becomes distorted as shown in the figure. The plot of error against rotation angle in figure 5.3 shows a first order variation as predicted.

The circle case is difficult for the IPS method because at some points there is a large distance between the circle and the plate. An aerofoil test case is shown in figure 5.4. Here the aerofoil surface and the plate are closer at all points and therefore the IPS should perform better (in the sense of less introduced deformation). Again the CVT method recovers the aerofoil profile exactly. The recovered profiles by IPS are

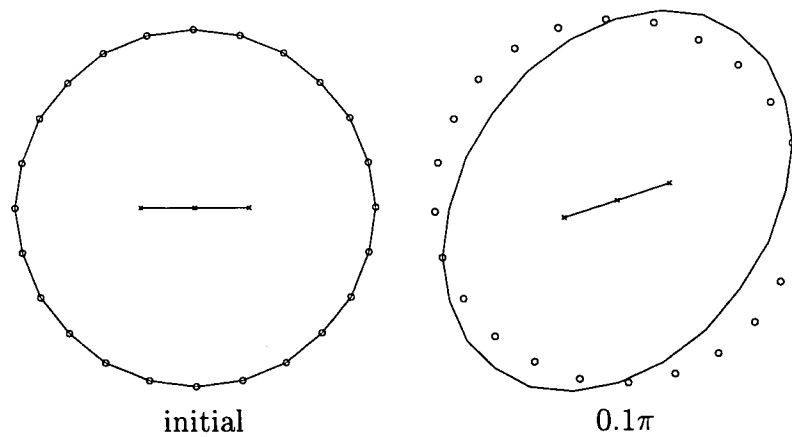


Figure 5.2: Rigidly rotated circle - solid line is interpolated fluid grid points by IPS, crosses are structural grid used for transformation, circles are exactly rotated fluid points.

shown in figure 5.4 and indeed show a smaller distortion than for the circle. Again the error is linear in the rotation angle, as shown in figure 5.5.

For a second set of test cases a finite element solution is used to calculate the deformation of a solid under an applied load. The ability of the transformation to recover the deformation of one surface of the solid given the exact location of another surface is examined.

The next test case involves the bending of a beam. The aerodynamic grid lies on the exterior of the beam and the structural grid is defined by three points on a line along the main axis of the beam. The outer two structural points are displaced by equal amounts. Sections through a beam undergoing such a motion remain parallel to the beam axis [60].

The transformation methods are again used to recover the fluid grid, as shown in figure 5.6. The IPS results do not conserve the beam right angles, again due to the out-of-plane treatment, in contrast to the CVT.

The final two-dimensional case involves significant dilatation. A bar is fixed at one

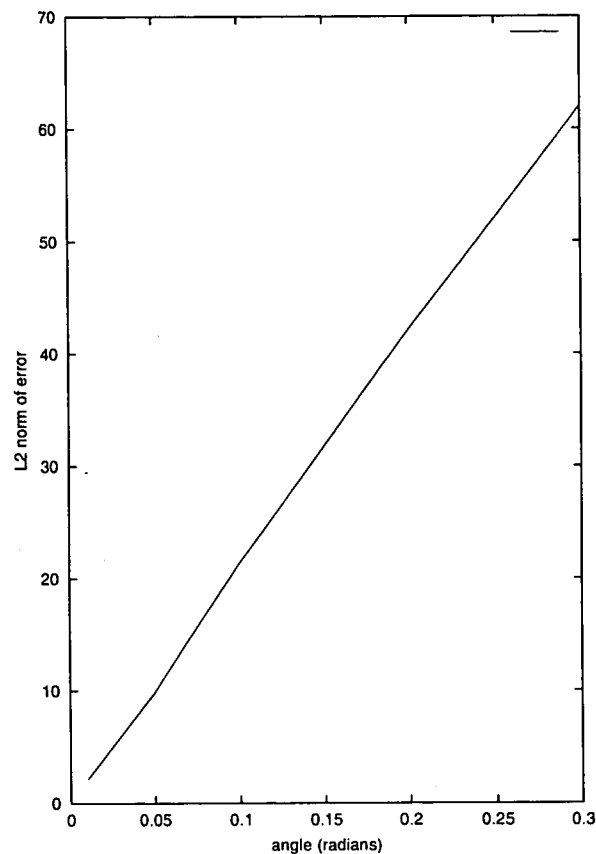


Figure 5.3: Rigidly rotated circle - L2 norm of the difference between the rigidly rotated fluid positions and the interpolated positions by IPS for different rotation angles

end and is stretched by a force applied parallel to the axis of the beam at the other end. The deformed shape was calculated using the finite element package NASTRAN. The ability of the interpolation methods to recover the fluid grid points on the outer surface given the locations of grid points on the beam axis was investigated. First, since the out-of-plane component for IPS is fixed and the displacements on the axis are in-plane, IPS stretches the upper and lower surfaces parallel to the axis. This results in a bar of increased volume. In contrast, CVT adjusts the out-of-plane components according to in-plane displacements. The recovered surfaces are close to

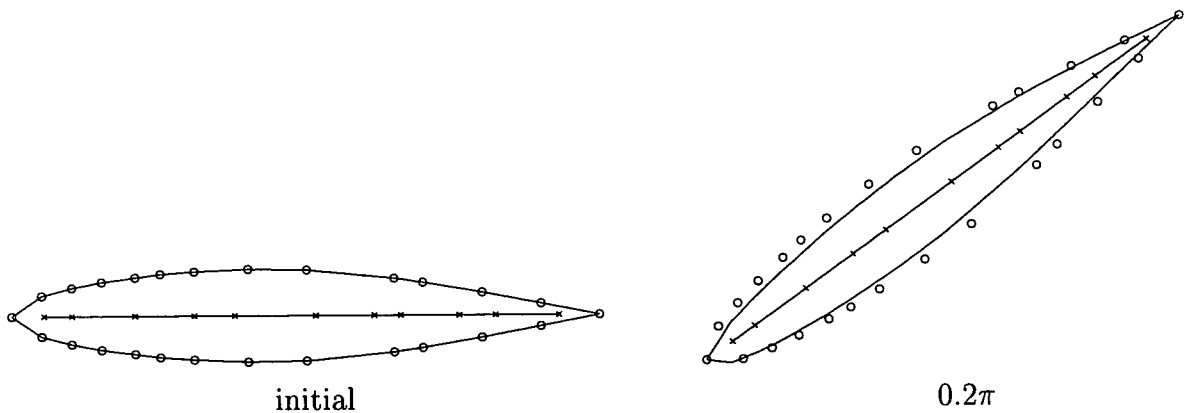


Figure 5.4: Rigidly rotated aerofoil - solid line is interpolated fluid grid by IPS, crosses are structural grid used for transformation, circles are exactly rotated fluid points.

the FE solution, as shown in figure 5.7.

To test the method for three dimensional problems the bending and torsion of a half cylinder fixed at the root is considered. The response of the cylinder to applied forces is calculated using an FE model in MSC/NASTRAN. The deformation of the flat surface is then used with a transformation for the new location of the curved surface, shown in figure 5.8. The interpolated points are then compared with the predictions of the FE model to assess the performance of the interpolation. For the bending motion IPS and CVT both perform well, with the maximum difference with the FE solution in calculated location being 2.5 %. For the torsional case the maximum differences are 2.4 % and 6 % respectively. The node line patterns for the torsional case are shown in figure 5.9 and show the qualitative differences in the reconstructed surface for IPS, again arising from the treatment of the out-of-plane motion.

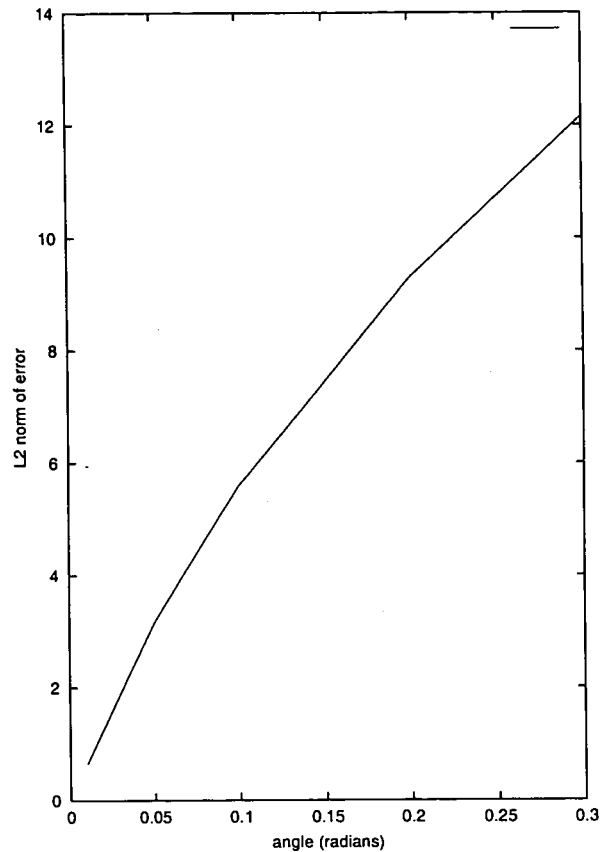


Figure 5.5: Rigidly rotated aerofoil - L2 norm of the difference between the rigidly rotated fluid positions and the interpolated positions by IPS for different rotation angles

5.6 Evaluation of CVT and BEM-based Transformation

Next, the CVT method is compared for some of the above test cases with the BEM methods described in the previous chapter. The first case is the aerofoil under rigid rotation. Slight distortions are seen at the trailing edge when using the original method which are eliminated when using the modified method, as seen in figures 5.10 and 5.11. The results are similar to those obtained using CVT.

The second case considered is the rigid rotation of a circle. For small rotations,

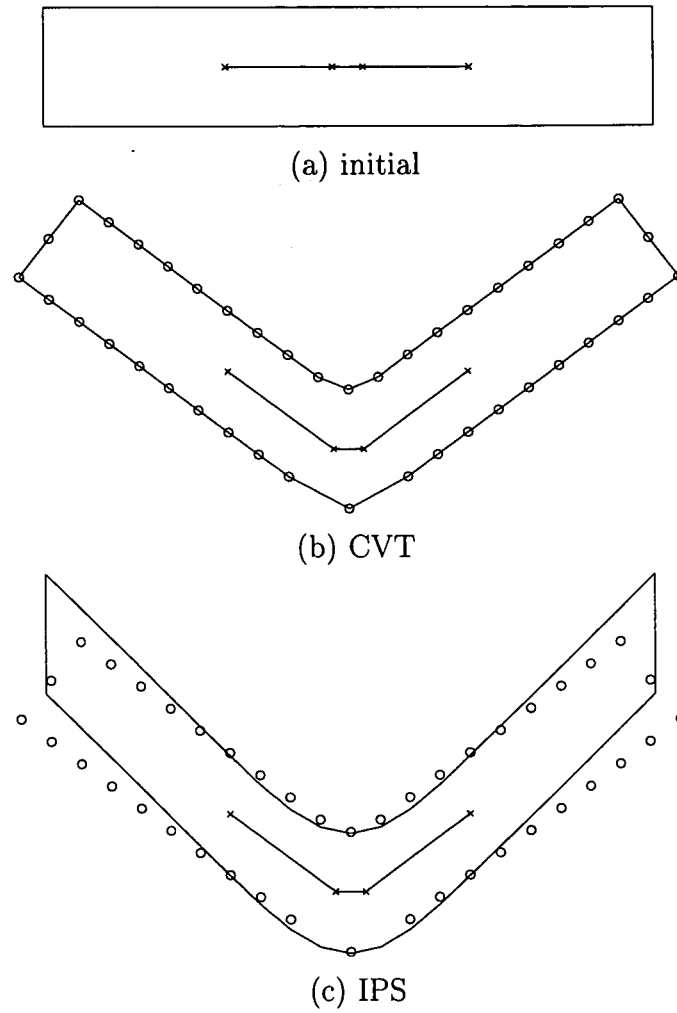


Figure 5.6: Bending beam - solid line is interpolated fluid grid, crosses are structural grid used for interpolation, circles are FE solution from MSC/ NASTRAN.

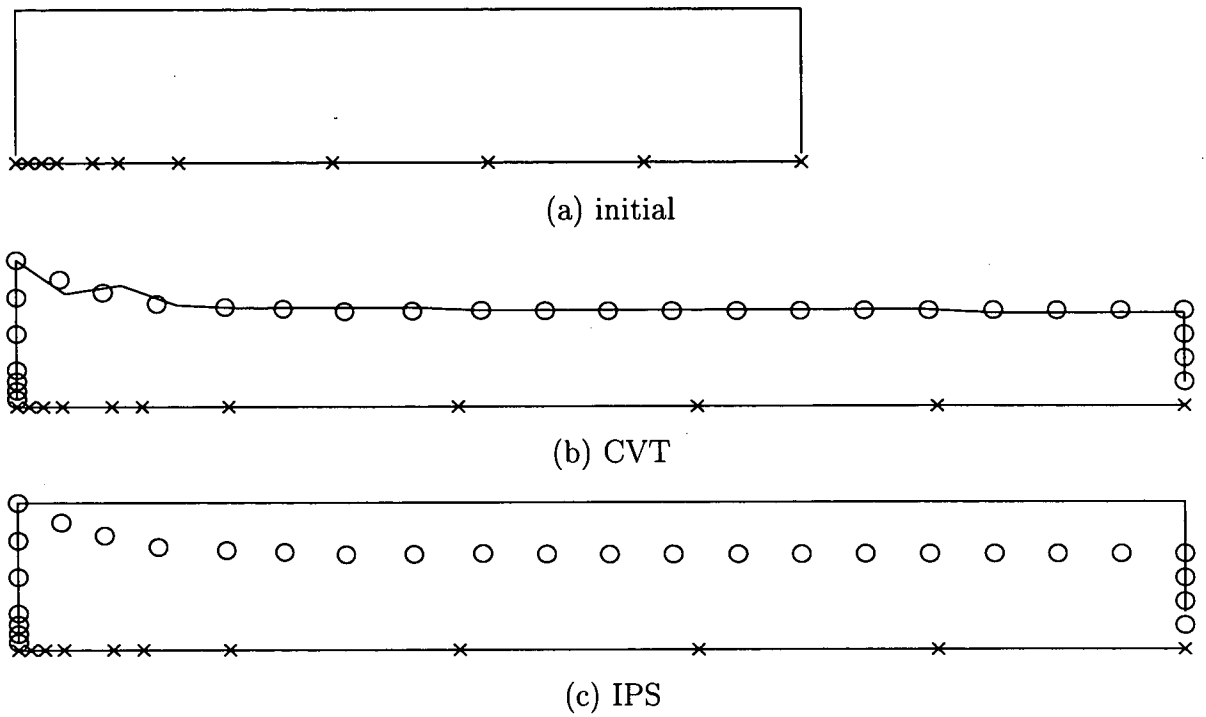
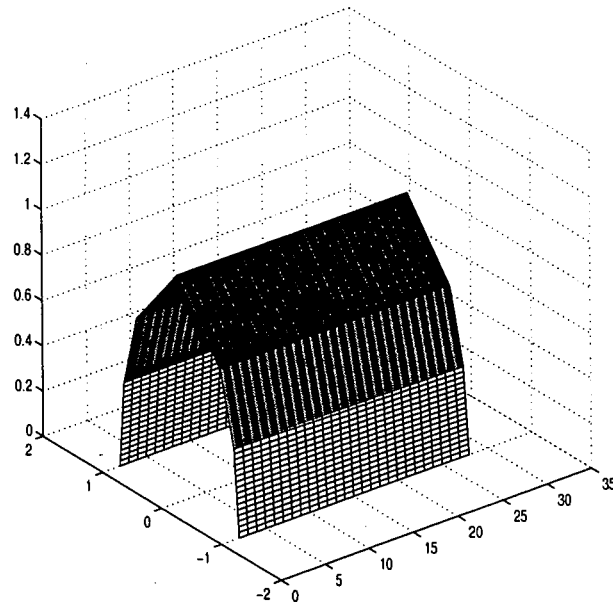
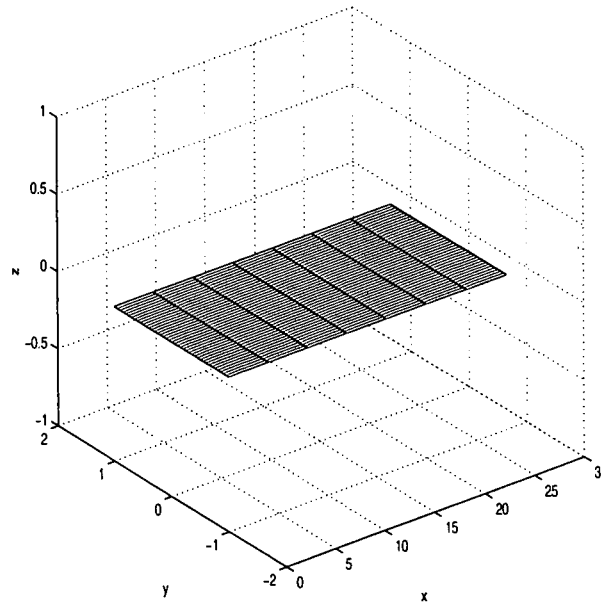


Figure 5.7: Upper half of stretching beam - solid line is interpolated fluid grid, crosses are structural grid used for interpolation, circles are FE solution from MSC/NASTRAN.



(a) Fluid surface



(b) Structural Surface

Figure 5.8: Initial Solid and Fluid Surfaces

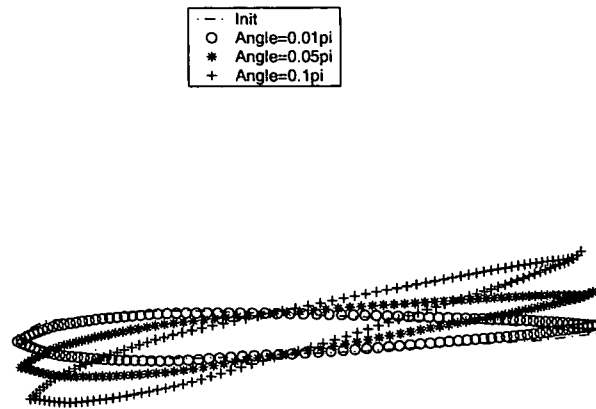


Figure 5.10: Aerofoil rigid motion original BEM method

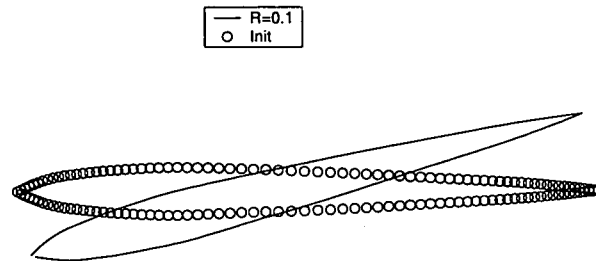


Figure 5.11: Aerofoil rigid motion with Modified BEM method

the shape is conserved as shown in figure 5.12, However, the circle is thickened for larger rotations, as shown in figure 5.13. These results are worse than those presented above for CVT.

In reference [53] the bending beam was considered to illustrate that, because of the lack of coupling of displacements in different directions, the IPS method does not conserve orthogonality. This was seen in the results already presented. Reproducing the results using the Chen method we found that although the orthogonality of the beam corners is preserved, the area is not. In fact the BEM based method thickens the beam as illustrated in figure 5.14.

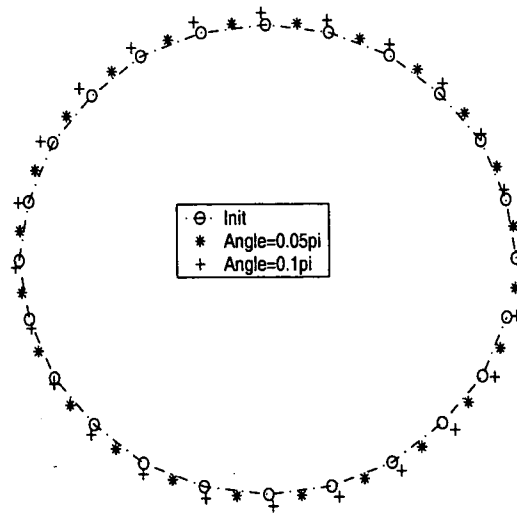


Figure 5.12: Circle rigid motion with Virtual BEM

In conclusion, the results here show no reason for using the Chen methods, especially when considering the disadvantages of a relatively involved derivation and the need to store full matrices.

5.7 Conclusions

A method for transforming data between non-matching fluid and structural grids has been analysed. The shape preservation properties of the new method for rigid rotations has been shown to be superior to a commonly used scalar method, which introduces significant distortion which increases with both the rotation angle and the distance between the surfaces, and the BEM based methods of Chen. Two dimensional test cases have verified the analysis.

An immediate possibility is to combine the CVT out-of-plane treatment with a spline based method for the in-plane treatment. One significant advantage of the CVT as formulated is that the transformation can be written in terms of a sparse

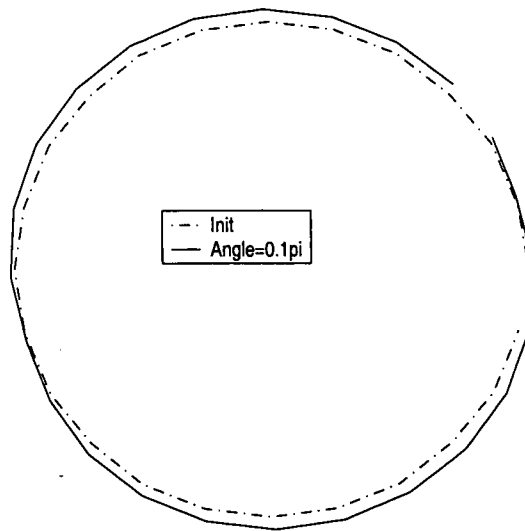


Figure 5.13: Circle rigid motion with Virtual BEM

matrix whereas spline based methods result in a full matrix which can be very costly to construct, store and retrieve.

The final stage of the work is to evaluate the influence of the transformation effects on dynamic and static aeroelastic responses. This is presented in the next chapter.

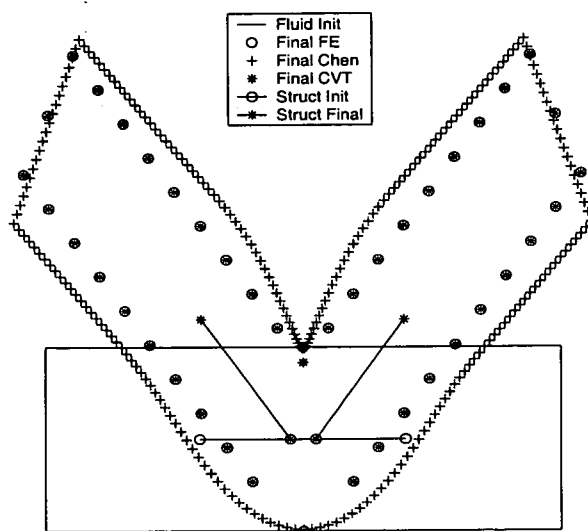


Figure 5.14: Beam under large bending

Chapter 6 : Time Marching Analysis

6.1 Overview

The geometrical properties of some transformation schemes have been considered in the previous chapter. However, these are only really significant in the way that they impact on the calculation of aeroelastic responses. In this chapter this aspect is examined by looking at two wing test cases. These cases are first reviewed and then results are presented for each case in turn. The results considered are the geometrical influence of the transformations and the influence on results computed for static and dynamic cases.

The transformation methods considered are listed in table 6.1. The colours next to each method are used for the presentation of transformed mode shapes and aerostatic and dynamic data unless stated otherwise. These methods are derived from those presented in the last chapter with *constant CVT* being the linearised version of CVT, *constant CVT-IPS* being the CVT method but with the linear in-plane treatment replaced by IPS and *regenerated CVT* being the linearised version of CVT applied incrementally, i.e. the structural deflections are applied in small steps and the transformation matrix is recalculated at each step. The latter method approaches the full nonlinear version of CVT as the increments become small.

method	in-plane	out-of-plane	colour
regenerated CVT	linear	updated CVT	blue
constant CVT	linear	fixed CVT	red
constant CVT -IPS	IPS	fixed CVT	cyan
IPS	IPS	stick	green
linear	linear	stick	purple

Table 6.1: Transformation Methods Evaluated in this chapter together with plotting colours used

6.2 Description and Review of Wing Flutter Test Cases

6.2.1 AGARD 445.6 Wing

An important problem inhibiting the development of aeroelastic simulation tools is the lack of experimental data available for their assessment. The experiments are intrinsically destructive and require delicate model construction to ensure the correct scaling of frequencies. Hence they are more expensive than rigid model tests. A complete set of measurements is available for the AGARD 445.6 wing and results for this case have been included in most publications on simulating flutter, giving a wide range of data with which to evaluate the current results. The disadvantage of this test case is that it does not feature significant nonlinear effects since the wing is thin. However, in the absence of a better case and due to the wide range of previous results, this test case will be used to evaluate the current method.

The AGARD 445.6 wing, whose planform is represented below, is made of mahogany and has a 45° quarter chord sweep (figure 6.1), a root chord of 22.96 inches and a constant NACA64A004 symmetric profile [61].

A series of flutter tests, which were carried out at the NASA Langley Transonic

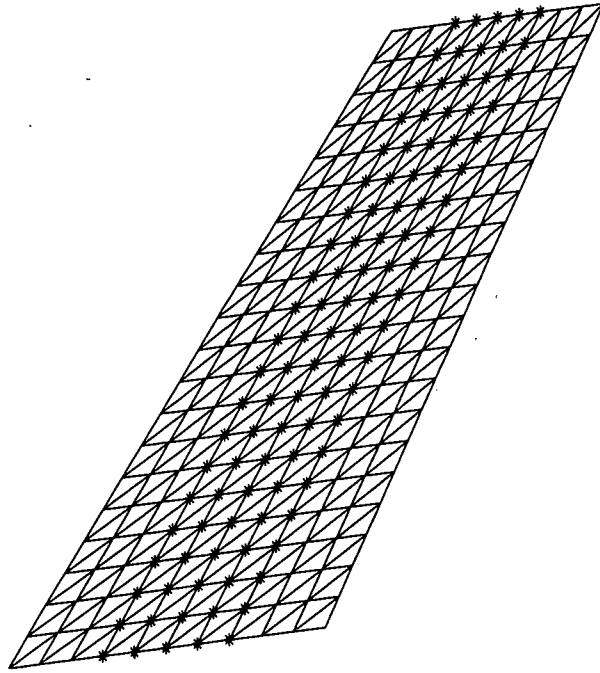


Figure 6.1: 445.6 wing planform. The dark shaded area indicates the extent of the grid for a reduced plate structural model used for some tests.

Dynamics Tunnel to determine stability characteristics, were reported in 1963 . Various wing models were tested (and broken). The case for which most published results have appeared is the weakened wing (wing 3) in air. This wing had holes drilled out to make it weaker and these were filled with plastic to maintain the aerodynamic shape. Published experimental data includes the dynamic conditions at which the wing was viewed to be unstable for Mach numbers in the range 0.338 to 1.141. The structural characteristics of the wing were provided in the form of measured natural frequencies and mode shapes derived from a finite element model.

A stability analysis of the wing using linear aerodynamic theory is described in the manual of the aeroelastic package ZAERO [62]. The small disturbance potential model is used to relate the fluid forces on a series of wing panels to the deflection of structural grid points. This linear relation, which is frequency dependent, can then be used in an eigenvalue analysis of the structural system to determine flutter points. The results of this method are used below for comparison with results from the current method. In theory linear results can be improved by using known nonlinear data to correct the linear force-deflection relationship. One example, which uses a Navier-Stokes solution of the steady state around the rigid wing at fixed Mach numbers, is given in reference by da Silva [63].

The aerodynamic model used in reference by Batina [64] is based on the frequency modified transonic small disturbance (TSD) equation. This model accounts for weak shock waves but involves a grid based fluid solution and hence is more expensive than a potential based model. It was found that the TSD results compared less favourably with experiment than linear results.

A coupled solution of the transonic small disturbance equations and a boundary layer model was used in reference by Edwards [65] to provide the fluid loading on a modal structural model. A time step of about 100 steps for each cycle of the first

bending mode was used with a sub-iteration to reduce sequencing errors. It was concluded that viscosity only has a small influence on the flutter behaviour but that nonlinear amplitude effects are significant at supersonic conditions.

An unstructured grid explicit solution of the Euler equations was coupled with a modal model of the wing by Gupta [66]. The fluid grid featured more than 240 thousand elements and 4167 explicit steps were used to resolve a cycle of the first bending mode. The region exterior to the wing was regridded when the deflections exceeded a user specified tolerance.

A multiblock Navier-Stokes solution was reported in reference [67]. The flow solution used the Beam-Warming Approximate factorisation with one sub-iteration to reduce factorisation errors. A modal model with 14 modes was used to describe the structure with transfinite interpolation being used for grid deformation. A grid with 815 thousand points was used for the flow solution with a coarse grid derived from this by taking every second point in each direction. Four thousand time steps were used to resolve the first bending mode. The wing stability was investigated at Mach 0.96 and at a Reynolds' number of 365 thousand. It was noted that the behaviour using 4 and 14 modes to describe the structural motion resulted in very similar behaviour. A very useful static test case was also published. The deflection at Mach 0.8, one degree of incidence and a dynamic pressure of 60.0 psf (pounds force per square foot) was computed by setting the time derivative in the structural model to zero.

An unstructured grid explicit solution of the Euler equations was coupled with a modal solver in Rausch [68]. A spring analogy was used to deform the mesh around the moving wing. The mesh contained about 130 thousand elements and 3000 time steps were used to resolve each cycle of the first bending mode.

A full finite element structural model was coupled to an unstructured solution of

the Euler equations by Lesoinne and Farhat[69]. The grid used for the fluid calculation is coarse with only 22 thousand vertices. A second order time accurate formulation was used which allowed large time steps to be used, resulting in 100 steps for a cycle of the first bending mode. The simulation produced comparable results to those in the references cited above but at less computational cost.

The numerical details of these calculations are summarised in table 6.2 and the prediction of the reduced flutter speed in table 6.3. Results are presented in this chapter which were generated by a time marching solution of the Euler equations coupled with a modal structural model. The performance of the method is indicated through comparison with the results shown in tables 6.2 and 6.3.

The linear structural model for the 445.6 wing which is used for the current results was built in NASTRAN. The model parameters are as quoted in Kolonay's[70] aeroelastic optimisation study and were also used in a static and dynamic time marching study, Melville [67]. The wing is modelled as a homogeneous material by quadrilateral plates. The material properties used are $E_1 = 3.15106 \times 10^9$ Pa, $E_2 = 4.16218 \times 10^8$ Pa, $\nu = 0.31$, $G = 4.39218 \times 10^8$ Pa and $\rho = 381.98 \text{ kg/m}^3$ where E_1 and E_2 are the moduli of elasticity in the longitudinal and lateral directions, ν is Poisson's ratio, G is the shear modulus in each plane and ρ is the wing density. The model consists of two hundred and thirty one elements. Comparison of the frequencies of the first four modes with experiment is made in table 6.4, showing reasonable agreement, and the first four mode shapes are shown in figure 6.2. Previous results have suggested that the difference in flutter speed for a dynamic test case when using 4 and 14 nodes is less than 1% [67]. To characterize the modes, the first is a bending mode at a frequency of 9 Hz, the second is a torsion mode at a frequency of 34 Hz, the third mode is a bending mode at a frequency of 50 Hz, and the fourth is a torsion mode at 80 Hz.

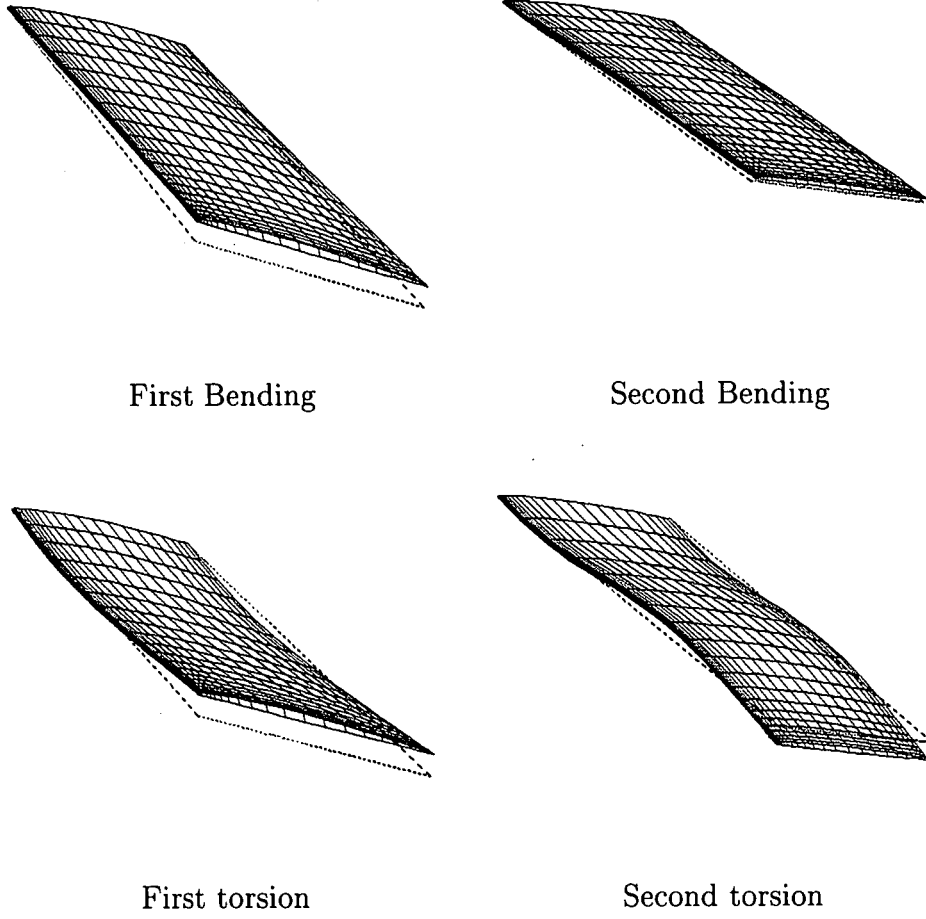


Figure 6.2: First four modes from FE model of 445.6 wing.

reference	Modelling	grid	Time step (steps/cycle)	CPU
[64]	TSD	N/A	N/A (105)	N/A
[66]	Euler	240k elem	N/A (4167)	19h on RS6000/590
[69]	Euler	22k vert	N/A (100)	N/A
[68]	Euler	130k elem	N/A (3000)	12h on Cray-2s
[67]	Navier-Stokes	102k cells	N/A (4000)	N/A
present	Euler	98k cells	0.22 (105)	4 hours on P200

Table 6.2: Summary of numerical details for single flutter calculation. N/A indicates that the information was not included in the reference. Here, steps per cycle refers to the first bending mode and the time step is non-dimensionalised with respect to the freestream velocity and the root chord.

Mach	Pmb	Nastran	[61] Exp	[63] da Silva	[62] Zaero	[68] Rausch	[66] Gupta	[67] Melville	[69] Lesoinne
0.449	0.452	0.43	0.4459	0.45	0.44	0.439	0.436	N/A	0.45
0.678	0.418	0.43	0.4174	0.395	0.44	0.417	0.380	N/A	0.42
0.901	0.332	0.373	0.3700	0.367	0.38	0.352	0.341	N/A	0.38
0.960	0.293	0.34	0.3076	0.319	0.35	0.275	0.280	0.34	0.30
1.072	0.452	0.424	0.3201	N/A	N/A	0.466	0.302	N/A	0.45
1.141	0.476	0.39	0.4031	N/A	N/A	0.660	0.410	N/A	0.66

Table 6.3: Summary of flutter speed predictions and measurements for AGARD 445.6 wing. N/A indicates that the information was not included in the reference.

6.2.2 MDO Wing

The Multi-Disciplinary Optimisation (MDO) wing was extracted from the MDO aircraft designed in a Brite-Euram project to establish design methodology for future large commercial aircraft. It was used in the Unsteady Flow in the Context of Fluid-Structure Interaction (UNSI) project as a test case for coupled CFD-structural dynamics simulations. Presentation of the case and the comparison of the results between the different partners can be found in the publication by the UNSI [57] partners. The MDO configuration was optimized for high performance at a particular cruise

	mode 1	mode 2	mode 3	mode 4
measured	9.60	38.10	50.70	98.50
calculated	9.67	36.87	50.26	90.00

Table 6.4: Measured [61] and computed modal frequencies in Hertz for AGARD 445.6 wing.

condition. The calculations are started from an estimate of the jig shape which leads to the design shape at cruise conditions.

The wing has a span of 36m and the planform is shown in figure 6.3. The profile is a thick supercritical section. The wing was structurally modelled as a box using finite elements. Calculations made on the wing used 18 mode shapes extracted from this model, a selection of which are shown in figure 6.4.

The different partners involved in the comparisons for this case were Alenia, BAE SYSTEMS, Dassault, ONERA and Saab. The methods they used for their calculations are now briefly described. Most of the codes solved the Euler equations, with one full potential solution and some codes being coupled with a boundary layer solver. Alenia used the full finite element structural model for their calculations. The static and dynamic results showed minor differences between the different methods. The interpolation methods used were IPS or polynomial methods for ONERA, interpolation on an intermediate grid for Dassault and the use of rigid elements in the NASTRAN solver by Alenia.

Three cases were used for the comparisons and are summarised in table 6.5. For each code the angle of attack is chosen to match the design lift coefficient. This necessitates at least three calculations to obtain the correct angle of attack. The static results are compared for the leading and trailing edge displacement distributions. For cases 2 and 3 dynamic calculations are initiated from the converged static solution

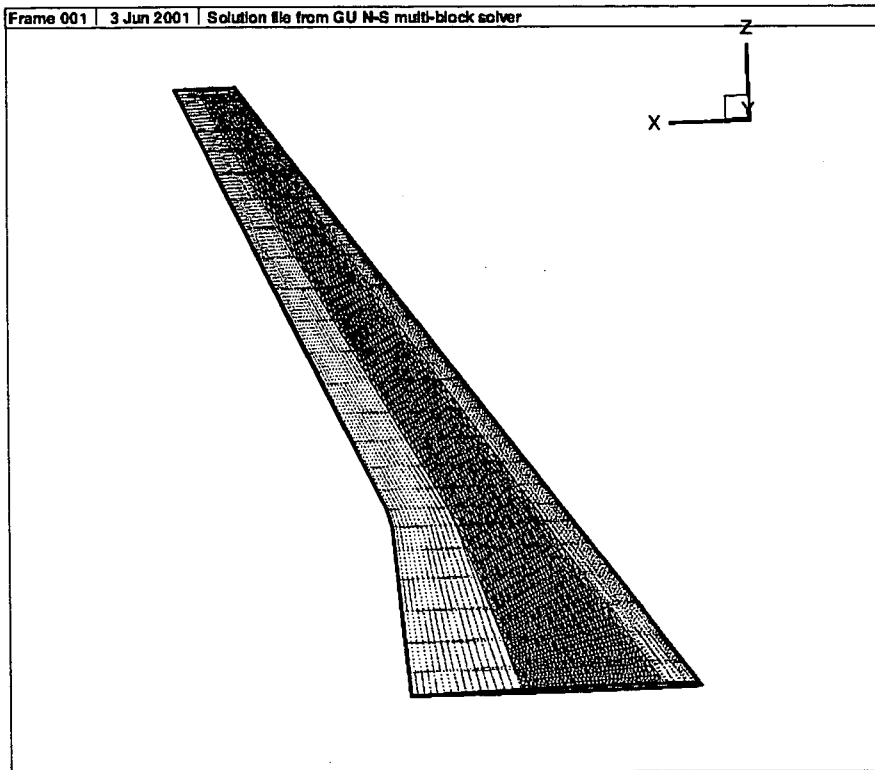
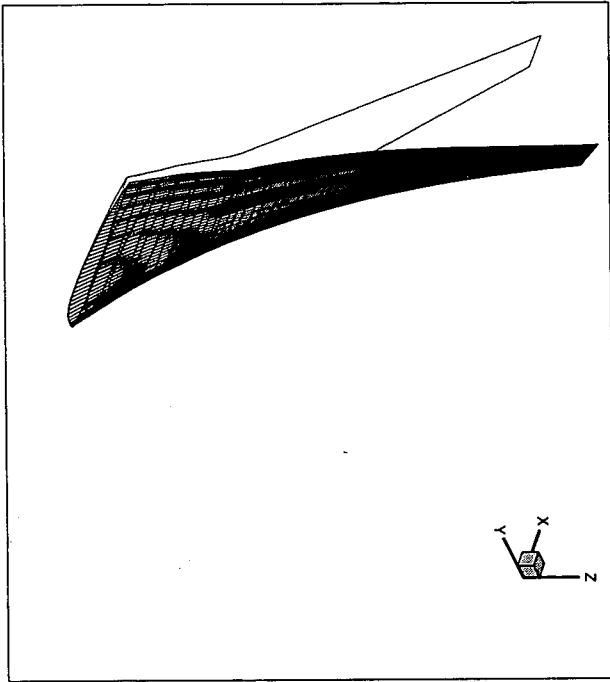
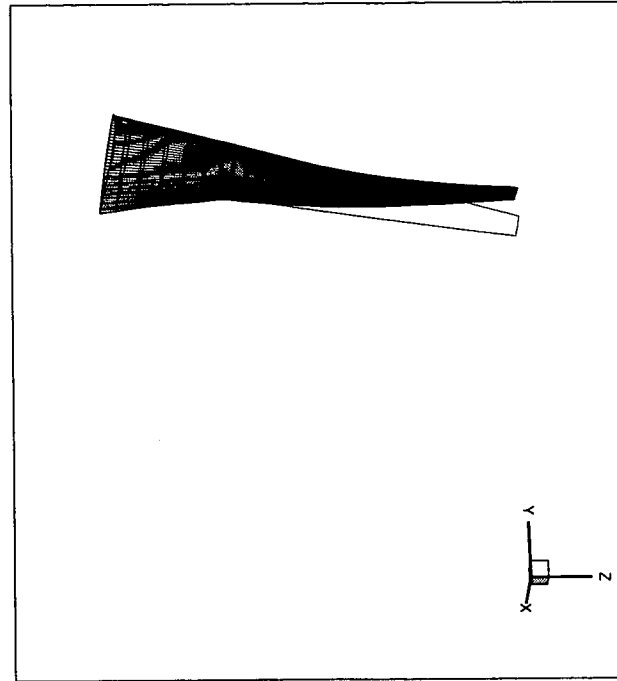


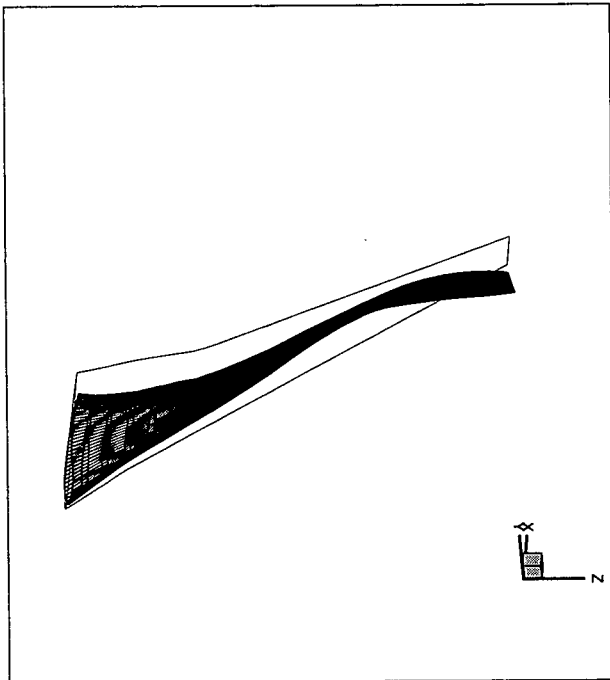
Figure 6.3: MDO wing planform. The dark shaded region indicates the extent of the structural model.



mode 1



mode 2



mode 5

Figure 6.4: MDO mode shapes.

by giving the first mode a velocity of $v_1 = 2\pi f_1 q_1 = 78.95$ where q_1 is the coordinate of the first mode which results in a tip deflection of one metre. Case two turns out to be stable and case three gives flutter. A linear analysis using MSC NASTRAN indicates that case two is just below the flutter boundary and that the stability changes due to the damping of mode three becoming positive. Comparison of the current results is made with results from Saab which are typical of the results from the UNSI comparisons [57].

	Case 1	Case 2	Case 3
Mach Number	0.85	0.88	0.88
Lift Coefficient	0.4581	0.3263	0.1686
Aircraft Mass	371 tons	537 tons	537 tons
Altitude	11.27 km	7km	2km

Table 6.5: Conditions for MDO test case. The lift coefficient quoted here is scaled in terms of the wing surface area,

The Saab results were generated using the EURANUS code which solves on multi-block structured grids using explicit time stepping and multigrid. Central and upwind differencing options are available. The mesh is moved via a sequence of pre-determined perturbation grids. The transfer is achieved by projection onto a neutral surface and interpolation to obtain the displacement of projected points. Pseudo-time stepping is used for unsteady calculations and pseudo iterations are used to remove sequencing effects between the fluid and structural solutions.

6.3 445.6 Results

6.3.1 Grids and Numerical Tests

The aerodynamic grid is of C-H topology with 217 points around the section, 57 points normal and 61 points in the spanwise direction. There are 153 by 41 points

on the wing. A coarse grid was extracted to facilitate a grid convergence study by taking every second point in each direction.

No aerodynamic measurements are available for this wing. To test the aerodynamic predictions comparison is first made with previously published results [68]. The case considered is at a freestream Mach number of 1.141 and zero incidence. The convergence history on the coarse grid is shown in figure 6.5. The residual is reduced by 8 orders of magnitude in 638 residual evaluations on the coarser grid and 936 residual evaluations on the fine grid. The pressure distributions at 4 spanwise slices are shown in figure 6.6. It is clear that the coarser grid gives a good solution and close agreement is observed with the previous results by Rausch [68]. The coarse grid is used below for the aeroelastic calculations. Finally, a plot of the pressures on the wing in figure 6.7 indicates that a shock wave is located close to the trailing edge and is in good agreement with the plot shown in reference [68].

6.3.2 Interpolated Mode Shapes

Before presenting the aeroelastic results we examine how the mode shapes are transformed onto the fluid grid from forced motions in single modes on the structural grid. The interpolation methods tested group around the in- (with linear or IPS used) and out- (with stick, CVT constant and CVT regenerated) of plane treatments. The transformed mode shapes are presented as the profile cut at 75% of the span.

First, the bending modes do not show any differences (figure 6.8 (a)) between the various methods, as anticipated above when considering the model problems. However, when a torsion mode is considered differences are observed as seen in figure 6.8(b). These are exaggerated here by applying a large modal coordinate value to mode 2 to make the behaviour clear. The largest influence is seen if the constant CVT method is used for out-of-plane treatment, leading to a substantial fattening of

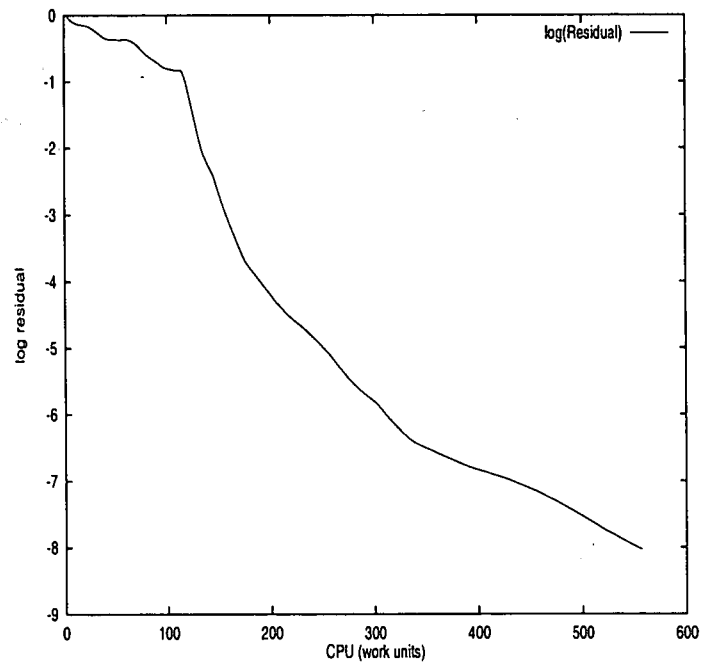


Figure 6.5: 445.6 rigid wing steady test case convergence history. $M_\infty = 1.141$, $\alpha = 0^\circ$.

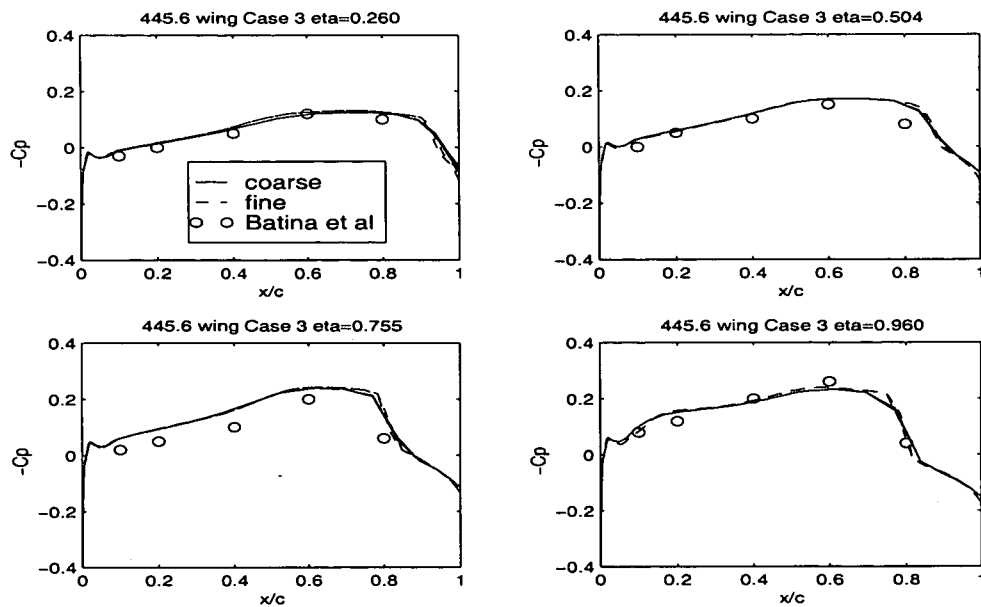


Figure 6.6: 445.6 rigid steady test case pressure distributions compared with the results from [68]. $M_\infty = 1.141$, $\alpha = 0^\circ$.

the profile. This is ascribed to the linearisation error used to derive the spline matrix. This can be cured by applying the modal coordinate as a series of increments (here ten increments was found to give an identical final result to using one hundred increments) and updating the spline matrix at each increment. Since the modal displacements are in the vertical direction the aerofoil chord is stretched by the torsional motion. The nonlinear CVT method, which the regenerated CVT method approaches here to good accuracy, reacts to this in-plane stretching by thinning the profile to maintain a constant volume between the fluid and aerodynamic surfaces. The thinned profile is seen in the figure. Finally, the influence of a stick out-of-plane treatment is seen to further thin the aerofoil profile. The in-plane treatment does not change the behaviour at all.

It proves useful for understanding the behaviour for the MDO wing examined later

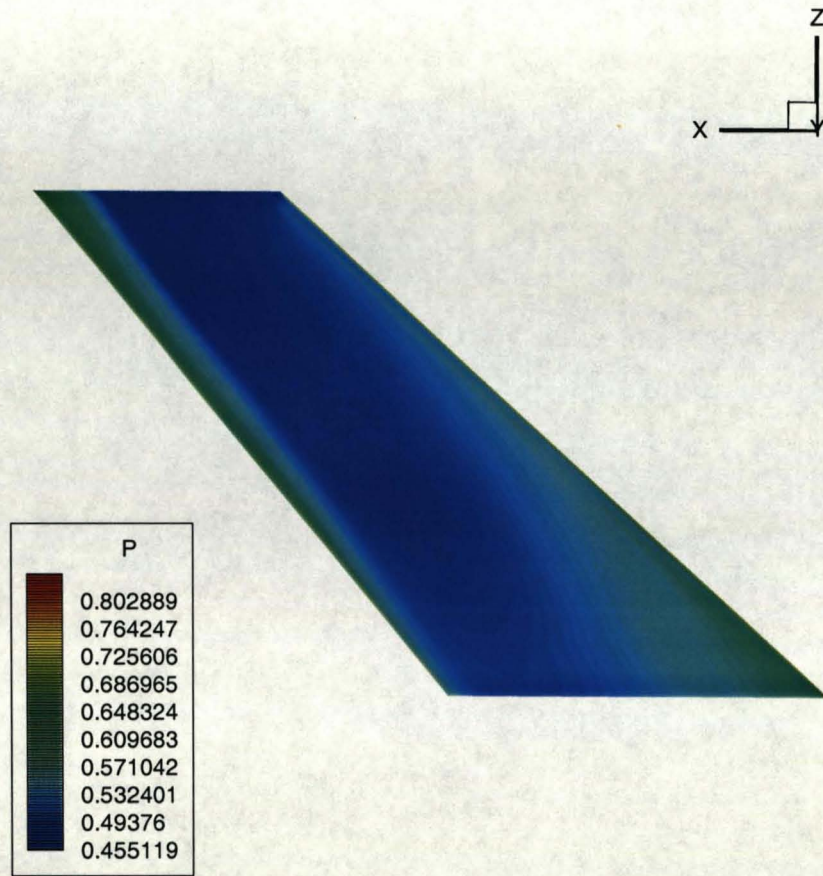


Figure 6.7: 445.6 rigid steady test case pressure contours. $M_\infty = 1.141$, $\alpha = 0^\circ$.

to view the transformed mode shapes from a structural grid which is a subset of the full grid and has had the leading and trailing edge portions removed, as shown in the darker area in figure 6.1. This challenges the transformation method to extrapolate the mode shapes off the leading and trailing edges of the structural grid onto those of the aerodynamic grid. The out-of-plane behaviour is as described above for the full structural model. However, in contrast, the in-plane treatment leads to different shapes for the torsional mode, as shown in figure 6.9 for the region around the leading edge. The essential shape of the mode is linear and hence it is not surprising that the linear in-plane treatment for the reduced model leads to a transformed shape which is close to that obtained using the full plate. The IPS method forces the displacement to behave linearly at increasingly large distances from the reduced plate leading and trailing edges, but linear behaviour is not enforced at small distances. This introduces an unwanted camber into the transformed profile. This influence has been noted by Brown [51] and has been termed graphically by one researcher as the “potato chip effect” since the edges of the aerodynamic profile become curled.

6.3.3 Static Case

As a check on the fluid grid movement and inter-grid interpolation, the static case first published in reference [67] was considered. This case is for the AGARD 445.6 wing at $M_\infty = 0.8$ and $\alpha = 1^\circ$. The freestream conditions are a velocity of 247.09 m/s and density of 0.09411 kg/m^3 . The wing tip deflections on the coarse and fine grids are summarised in table 6.6 and shown in figure 6.10.

The deflections on the coarse grid differ from those on the fine grid by less than 2% indicating that the fluid loading is well predicted on the coarse grid. The results are in close agreement with previously published results [67], which in turn agree well with the predictions from other codes. These results provide a good first check on

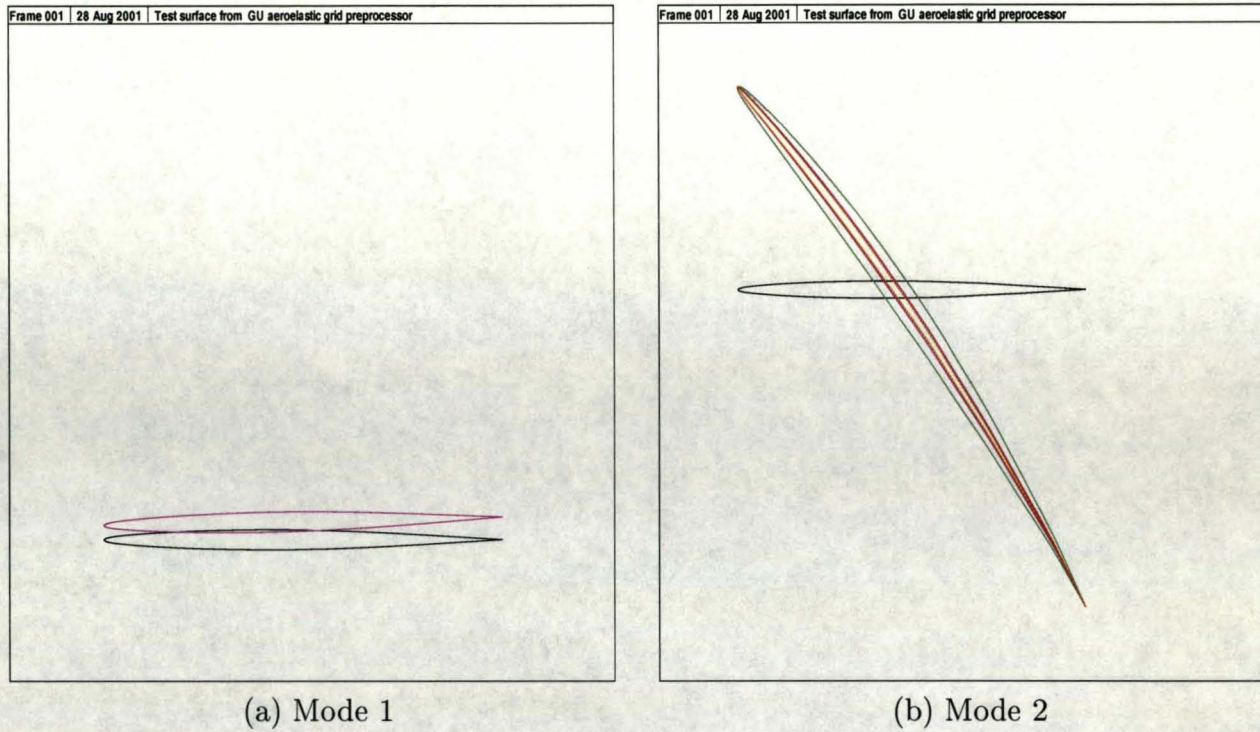


Figure 6.8: Transformed mode shapes at 75 % span

Mesh	Leading Edge	Trailing Edge
present-fine	0.44	0.50
present-coarse	0.42	0.48
Morton-fine	0.44	0.48

Table 6.6: Tip Deflection in inches for static aeroelastic deformation of AGARD 445.6 wing at a Mach number of 0.8 and an incidence of 1 degree.

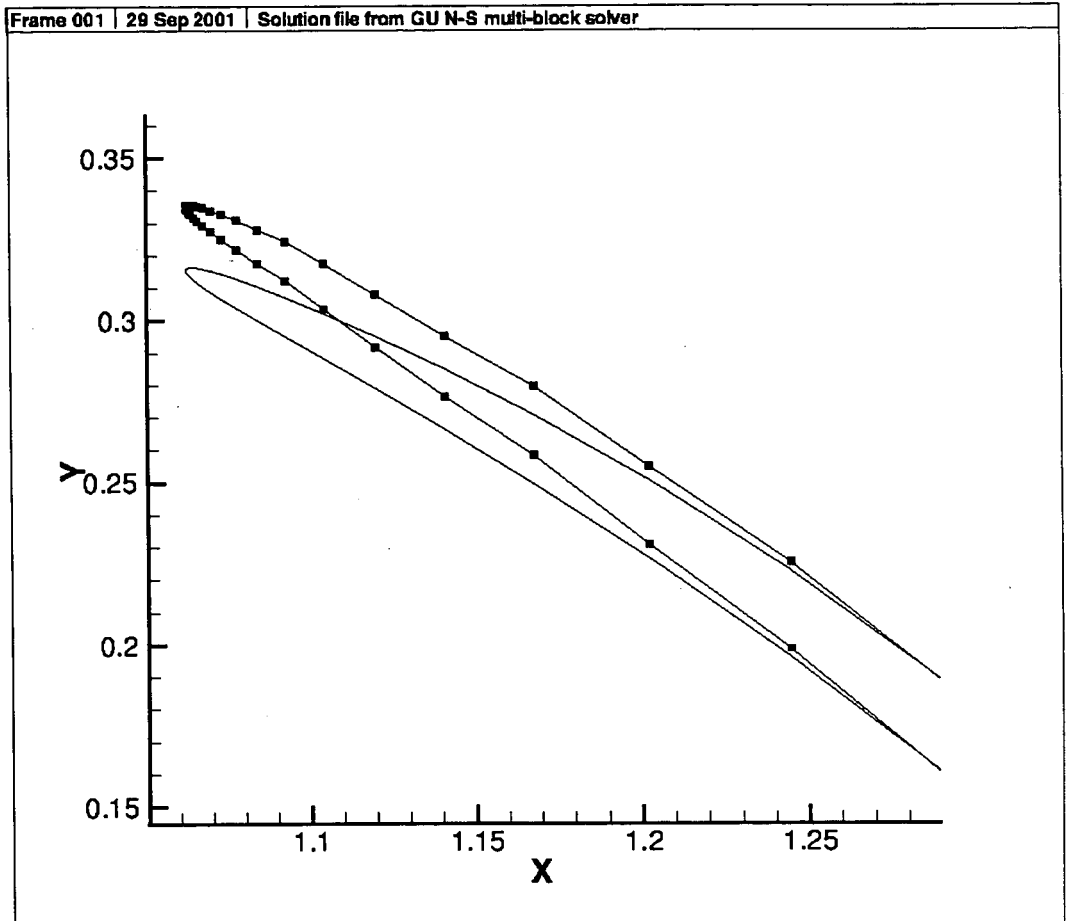


Figure 6.9: Transformed mode shapes for the 445.6 wing in the region of the leading edge at 75 % span. The profile marked with squares is obtained using IPS on the full span grid and is almost indistinguishable from that obtained using the linear transformation on both the full span and reduced span grids. The profile which is unmarked with squares is obtained using IPS on the reduced span grid.

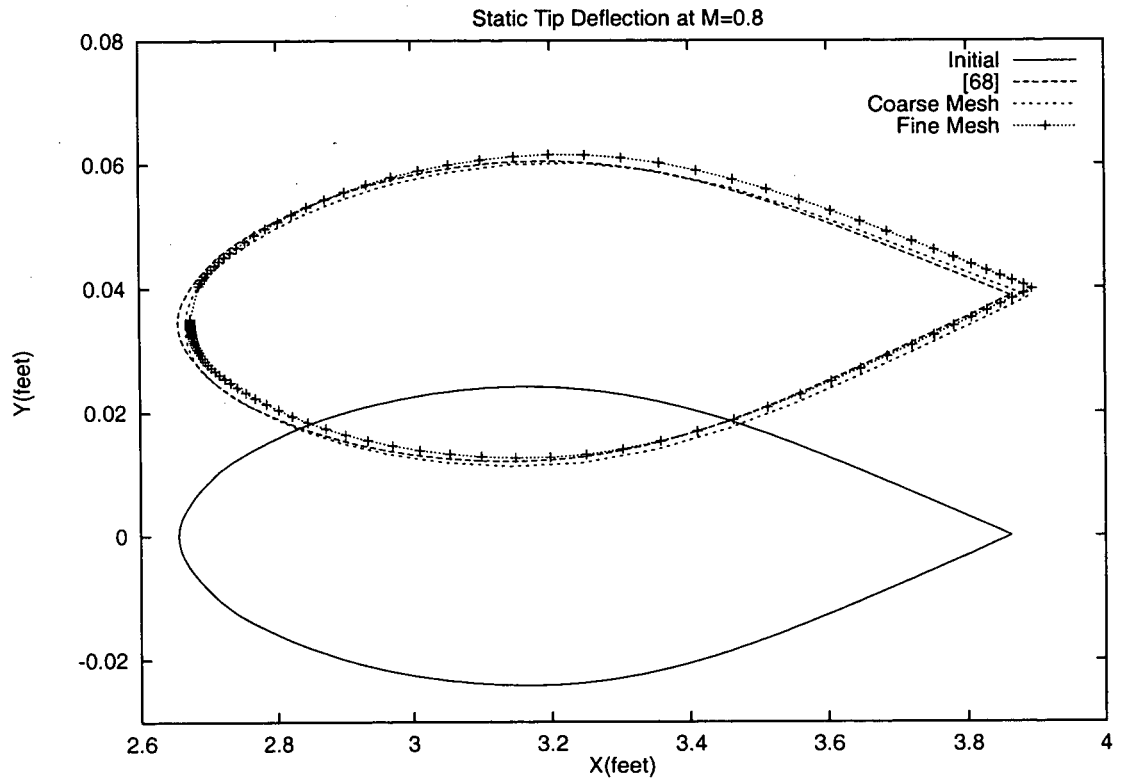


Figure 6.10: Aerofoil profile for first grid point inboard of tip for aerostatic 445.6 wing test case. $M_\infty = 0.8$, $\alpha = 1^\circ$.

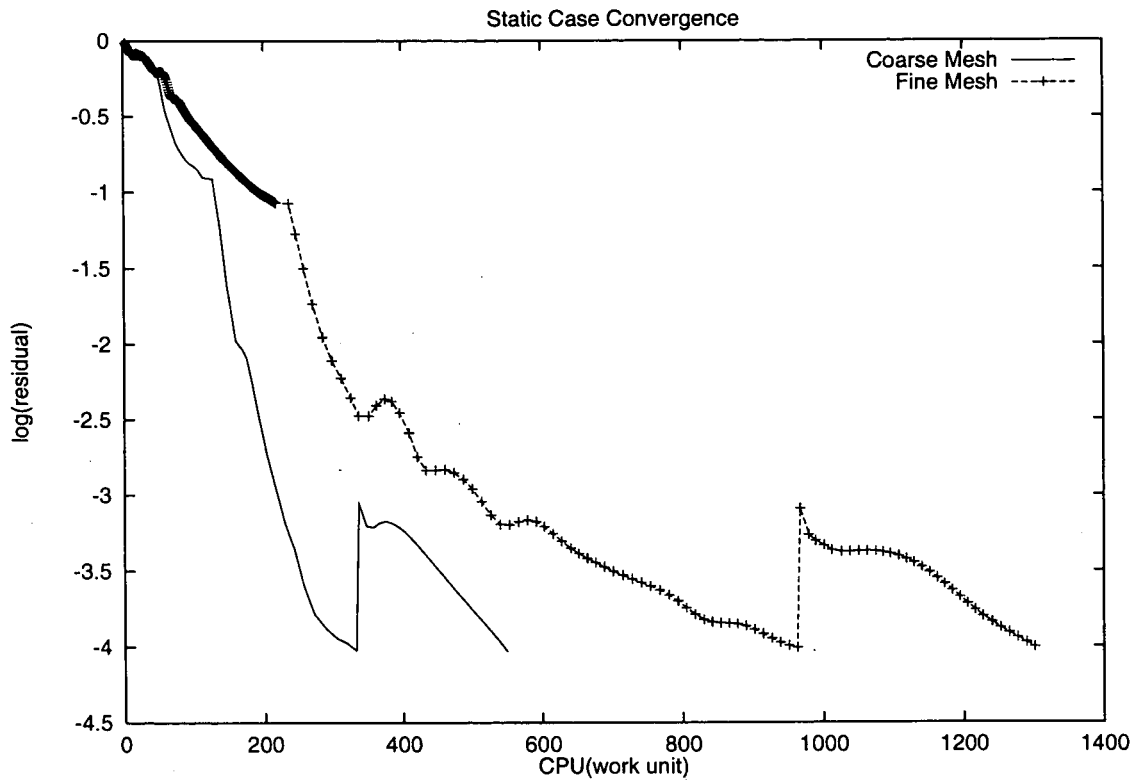


Figure 6.11: 445.6 aerostatic test case convergence history. $M_\infty = 0.8$, $\alpha = 1.^\circ$.

the methodology before examining dynamic behaviour. The calculation time using a Pentium Pro 200 MHz processor is 833 sec on the coarse grid. The convergence history is shown in figure 6.11 and shows that the convergence behaviour is similar for the rigid and deforming phases of the calculation. The rigid phase here refers to the calculation of the flow solution around the rigid wing, which is then followed by the deforming phase when the structure is allowed to deform.

Finally, we note that the tip profiles show that, due to the small displacements, and the small contribution of the torsional mode compared with the bending mode, the differences between the various transformation methods is small.

6.3.4 Numerical Tests for Dynamic Cases

For the dynamic results we look at four Mach number cases separately, with values of 0.678, 0.901, 0.960 and 1.141. The wing is given an initial dimensionless velocity in the first mode of $5.0e^{-5}$. The subsequent time evolution of the modal response is then calculated to see whether this grows or decays. The freestream velocity is fixed and the freestream density is increased until the damping changes sign (from negative to positive with increasing density). The value of the density at which this happens indicates the flutter speed, which can be expressed as an altitude or a dynamic pressure. Here, following convention, we express the flutter point in terms of a flutter speed coefficient

$$\bar{U} = \frac{U_\infty}{b_s \omega_\alpha \sqrt{\mu}}$$

where U_∞ is the freestream velocity at flutter, b_s is the semispan, $\omega_\alpha = 36.87 \text{ Hz}$ is the frequency of the first torsional mode and $\mu = m/\rho_\infty V$ where $m = 1.863 \text{ kg}$ is the mass of the wing, $V = 0.130 \text{ m}^3$ is related to the volume of the wing (see reference [61]) and ρ_∞ is the freestream density at flutter.

We first show that the numerical parameters used for the time marching calculations give reasonably accurate solutions. The conditions used for these tests are a freestream Mach number of 0.96, a velocity of 308.20 m/s and a density of 0.08 kg/m^3 . This turns out to be an unstable condition, where the initial velocity perturbation to the first mode grows in time.

The comparison of the time histories of the generalised displacements when using reduced time steps of 0.11 and 0.22 is shown in figure 6.12. Here the linear in-plane and stick out-of-plane transformations are applied although similar conclusions for the sensitivity studies were deduced for every method. The close comparison shows that the larger time step is adequate. The responses on the coarse and fine grids

are shown in figure 6.13. The coarse grid produces some numerical damping for the response and this increases the flutter speed. Due to the memory requirements of the method (about 2 Gb on the fine grid) it was not possible to continue the grid convergence study to complete convergence. The differences in the dynamic solutions is larger than was observed for the static aeroelastic cases. However, the results are in reasonable agreement, justifying the use of the coarse grid for the study of stability over a Mach number range. Typically only about four pseudo iterations are needed per real time step since small wing deflection changes are encountered at each time step. The coarse grid calculations require only 3-4 hours on a Pentium Pro 200 to calculate eight cycles of the first bending mode.

Comparing the performance of the numerical scheme with previously published results, as summarised in table 6.2, the advantages of the pseudo time method become clear. Results using explicit time stepping, as in Gupta [66], typically require 3-5 residual evaluations for each real time step. The stability limit on the time step leads to a very large number of steps being required for each cycle. In contrast the pseudo time method allows the time step to be chosen for time accuracy and hence much fewer steps are required (by a factor of 40). On average, using the unfactored solution method for the pseudo time problem, the equivalent computational time for about 20 residual evaluations per real time step is needed. Hence, by using a steady state solver which gives good convergence properties and the pseudo time method which allows sequencing effects to be removed without significant additional cost, the cost of Runge-Kutta time stepping method can be reduced by an order of magnitude.

The pseudo time method recovers second order time accuracy at convergence. Implicit time stepping is used by Rausch [68] but no mention was made of the use of sub-iterations to remove linearisation or sequencing errors. This could be the reason why a much larger number of time steps is required to resolve each cycle. An implicit

method is also used by Lesoinne and Farhat[69] in which second order accuracy is recovered. A staggering algorithm is used to ensure that the sequencing between the fluid and structural solvers does not reduce the accuracy of the coupled simulation below either component solver. The time step used is comparable to the one used here. Finally, an approximately factored implicit solver with three subiterations to remove fluid factorisation and sequencing effects was used by Melville [67]. This method is similar to the pseudo time method but using a restricted number of iterations is unlikely to completely remove the influence of factorisation errors at every time step, and this possibly explains the larger number of time steps required.

Dynamic Results

The dynamic results are presented in terms of the modal time histories for two values of the density which bracket the flutter point. The responses are shown in figures 6.14 to 6.17 for the four Mach numbers 0.678, 0.901, 0.960 and 1.141. The results are influenced by the out-of-plane treatment, with the constant CVT transformation introducing additional damping. For these dynamic calculations the transformation is recalculated at each real time step for regenerated CVT. The stick out-of-plane treatment gives results which are similar to regenerated CVT. There is no strong in-plane influence on the results, with the IPS results being only slightly more energetic.

The dynamic results for the 445.6 wing group according to the out-of-plane treatment. At all the Mach numbers the constant CVT and constant CVT-IPS methods are more heavily damped than the other three. The flutter boundary for the constant CVT and constant CVT-IPS methods lies above the one calculated using the other three methods, indicating that the response is stable at a higher density. The other three methods give a flutter boundary which agrees well with the experimental data and other calculations, as shown in figure 6.18. The difference introduced by the

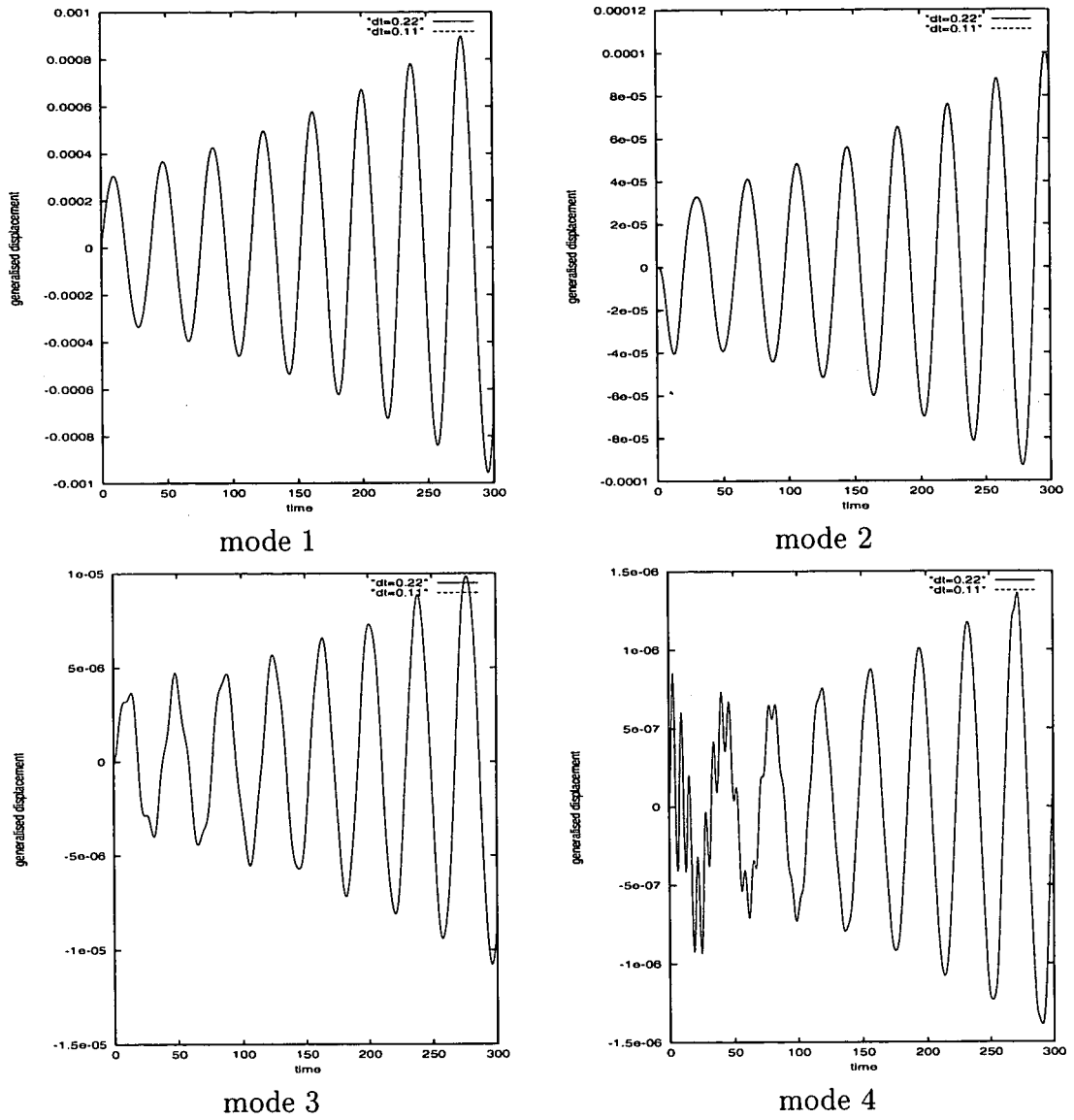


Figure 6.12: Time convergence for aeroelastic dynamic case at $M_\infty = 0.96$, $\rho_\infty = 0.08 \text{ kg/m}^3$, $U_\infty = 308.20 \text{ m/s}$.

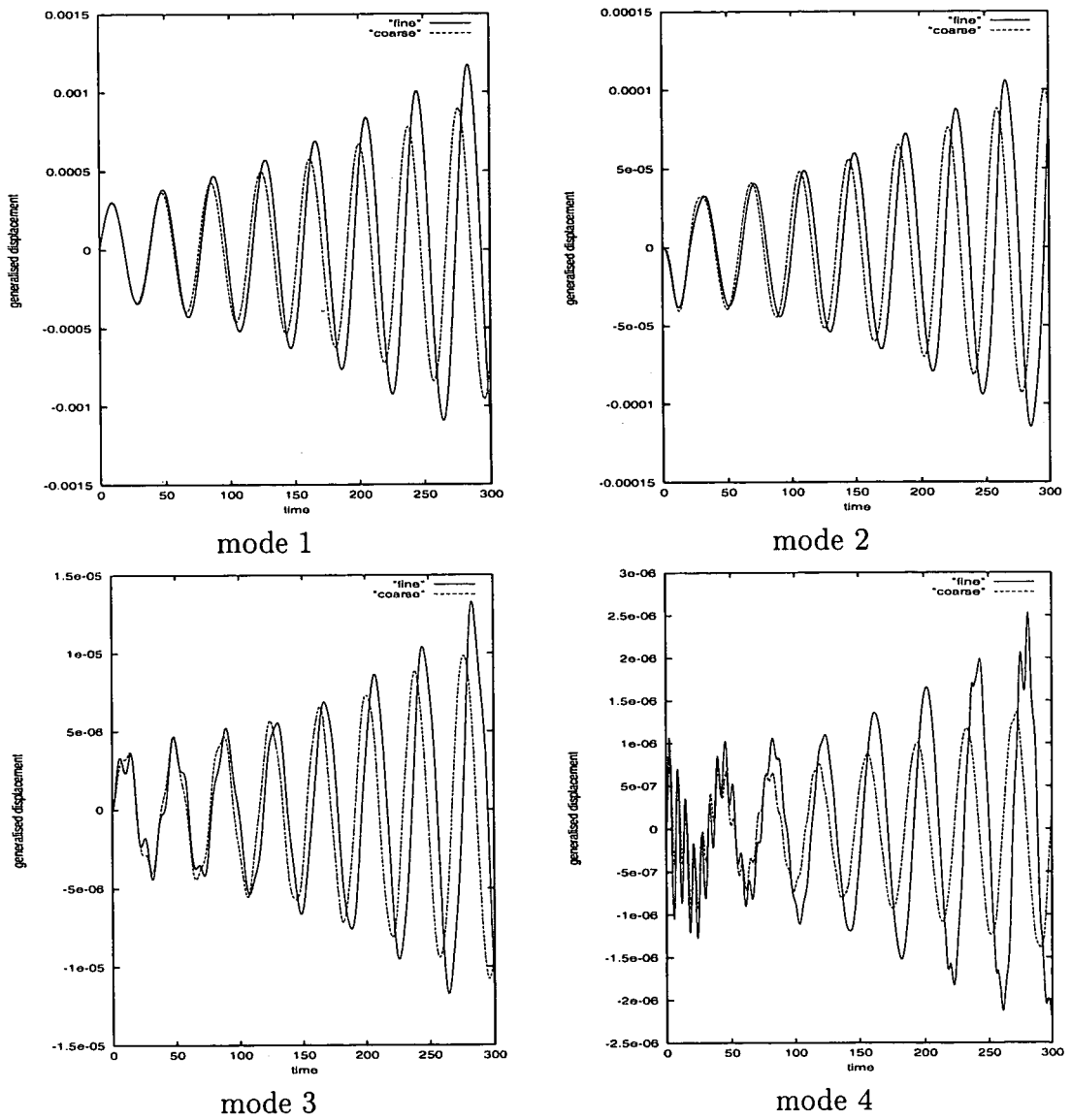


Figure 6.13: Grid convergence for aeroelastic dynamic response at $M_\infty = 0.96$, $\rho_\infty = 0.08 \text{ kg/m}^3$, $U_\infty = 308.20 \text{ m/s}$

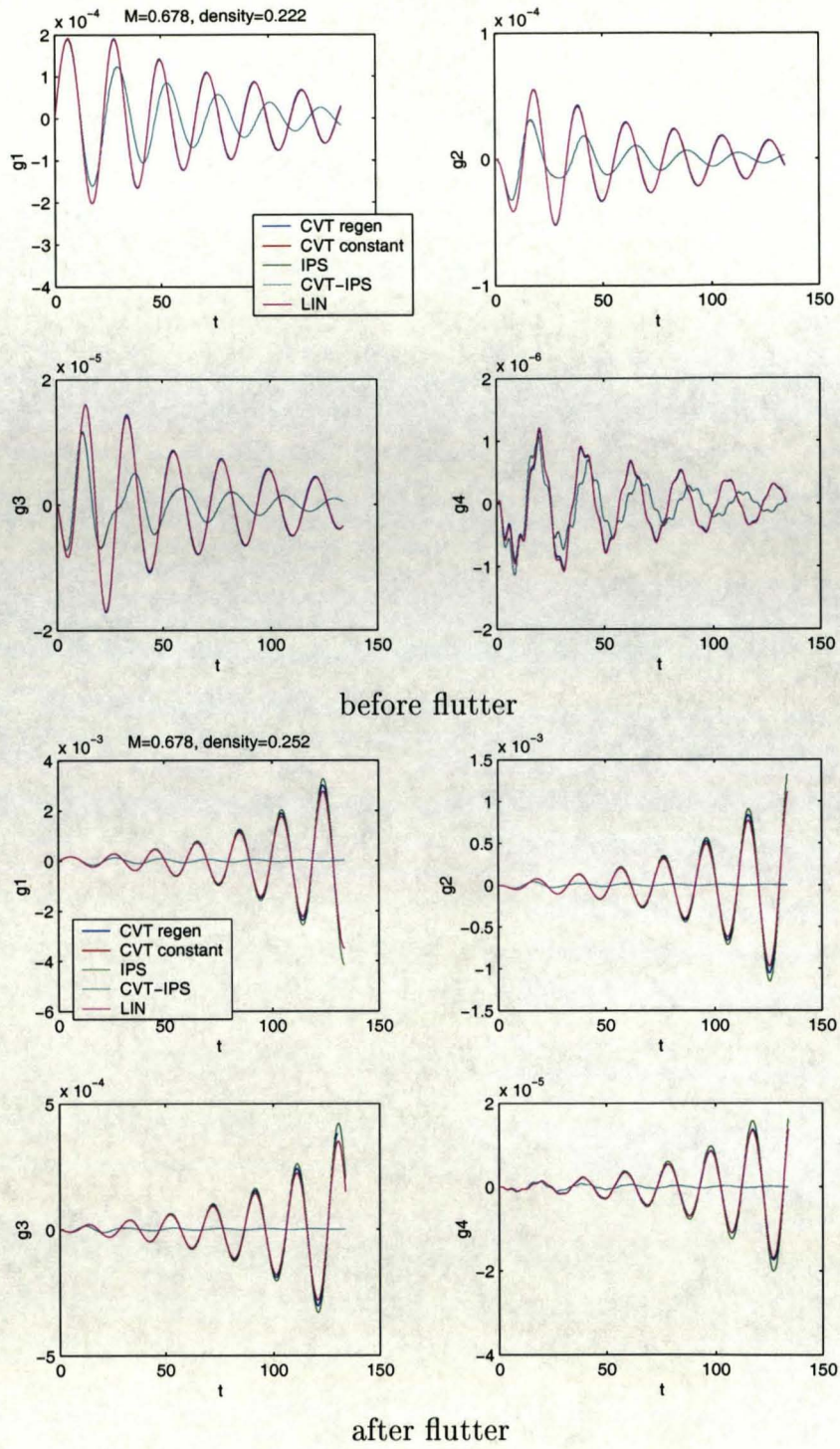


Figure 6.14: Time marching responses at Mach 0.678 for two values of density.

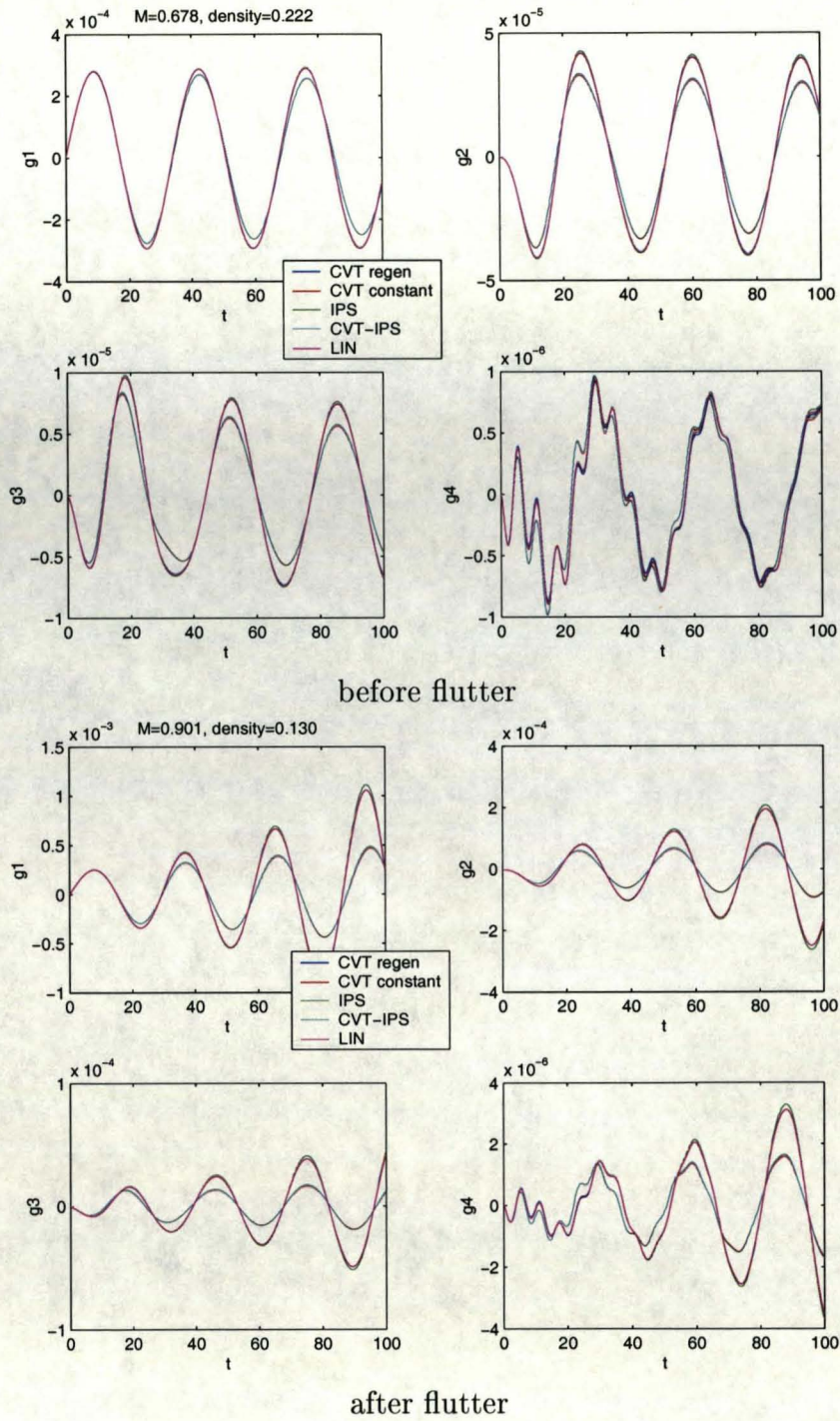


Figure 6.15: Time marching responses at Mach 0.901 for two values of density.

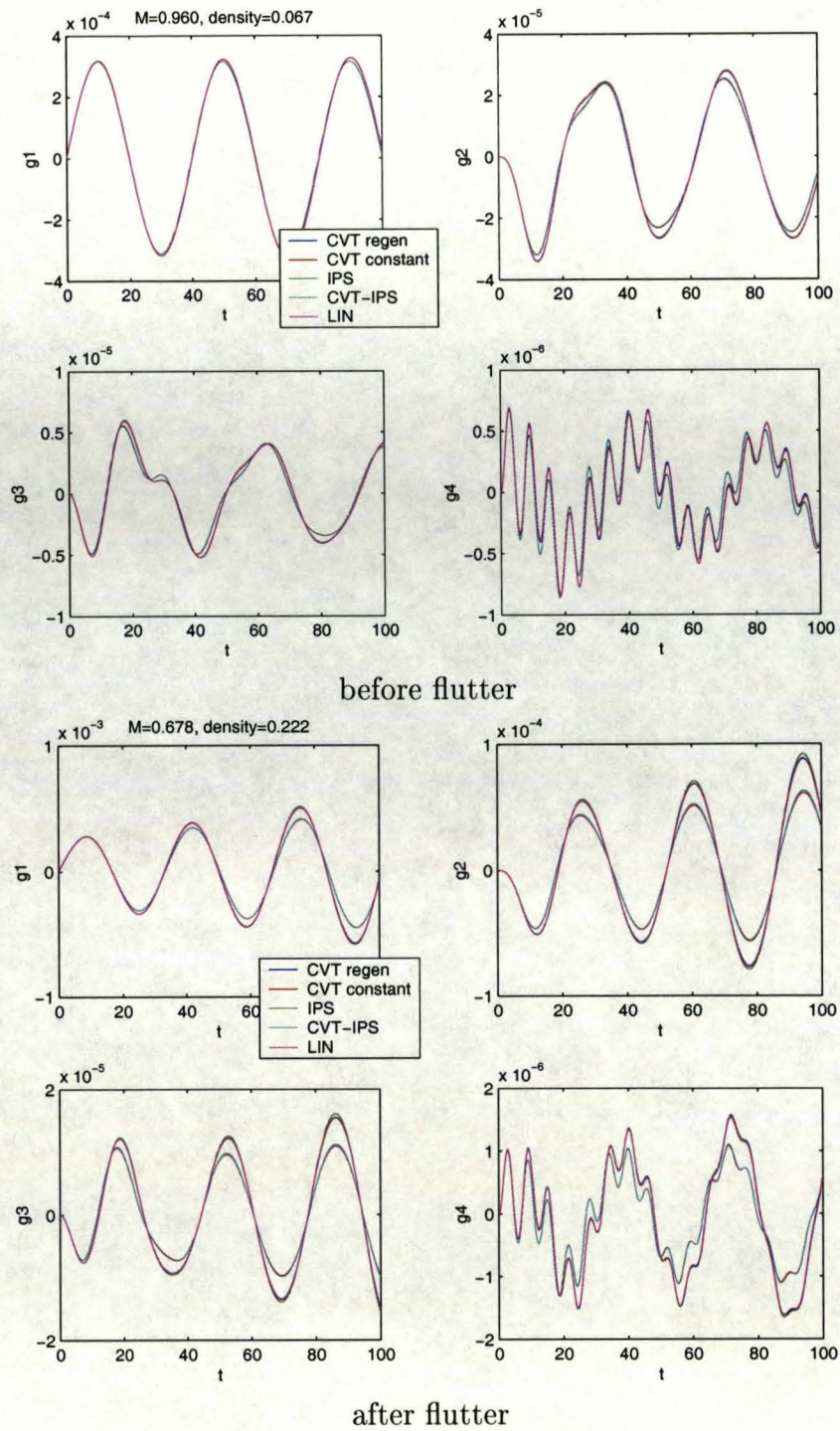


Figure 6.16: Time marching responses at Mach 0.960 for two values of density.

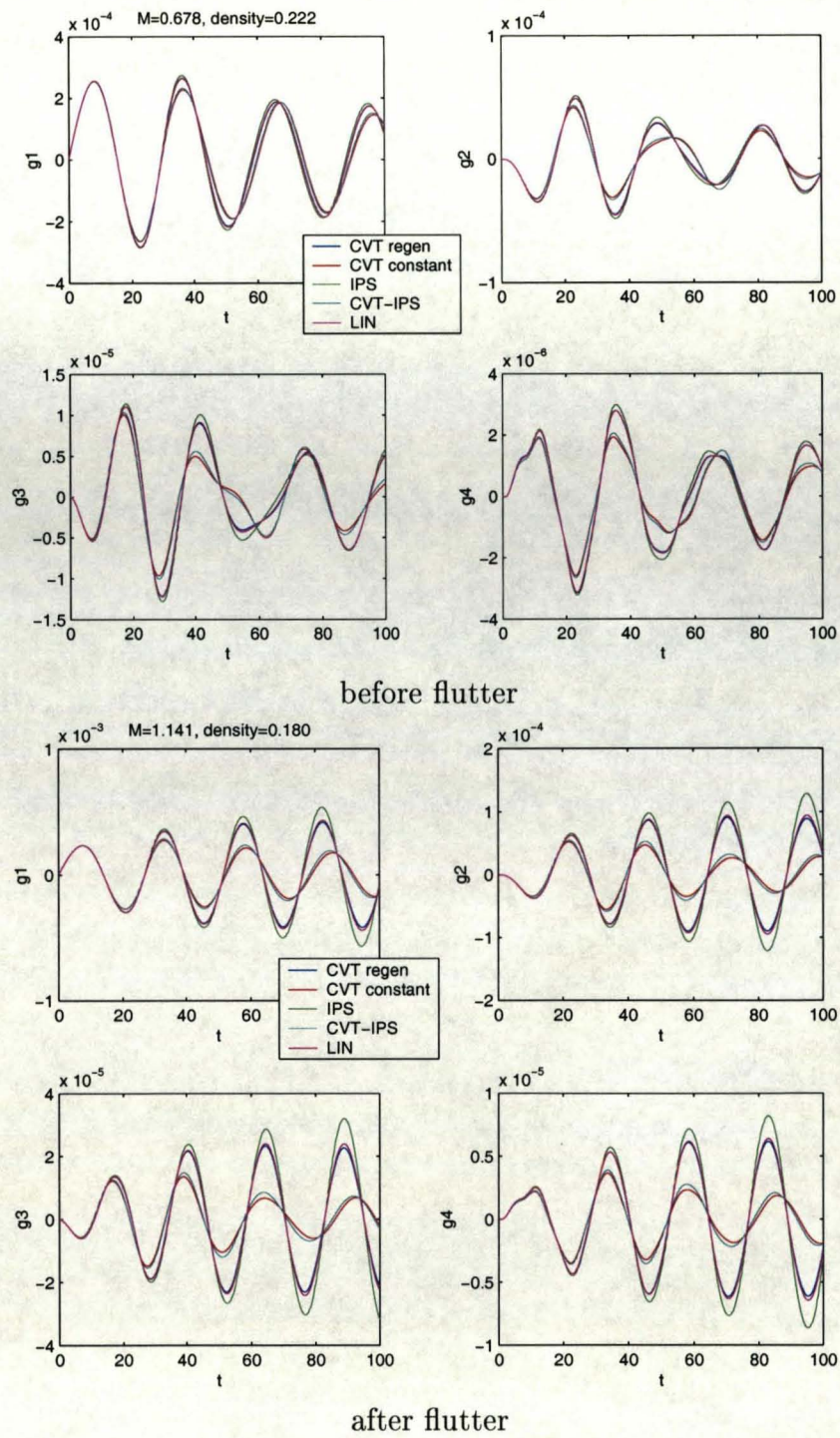


Figure 6.17: Time marching responses at Mach 1.141 for two values of density.

transformation method for the constant CVT out-of-plane treatment was seen above to be a fattening of the aerofoil profile for the torsion modes. Since the deflections are small and the wing is thin, the difference between the regenerated CVT and stick out-of-plane treatments is small, explaining the close agreement between time responses for these cases.

The computed stability boundary is compared with linear results in figure 6.18 and previously published results in table 6.3. For the thin wing considered here the transonic effects are minimal and linear methods can provide very good agreement with the measured behaviour. This is shown in figure 6.19 where the difference in the pressure coefficient between the lower and upper surfaces at Mach 0.96 and 1° incidence is shown for the Euler and potential models. No shock waves are present and the two sets of results agree closely. Even considering the thickness of the wing this is still a surprising result and shows that the advantages of a nonlinear flow model need to be quantified for a range of wing geometries. The linear results required a total of five minutes of CPU time on an SGI workstation to compute, although large memory requirements increased the elapsed time to thirty minutes due to swapping. The time marching results required about 250 hours of CPU time on a Pentium Pro 200 processor.

6.4 MDO Wing

6.4.1 Grids and Numerical Tests

The grids using for the MDO wing calculations are of C-H type and were previously generated at Saab for use in the EURANUS calculations discussed below. The grid has 129 by 25 by 33 points in the streamwise, normal and spanwise directions respectively, with 81 by 25 points on the wing itself. The total number of points in the grid is

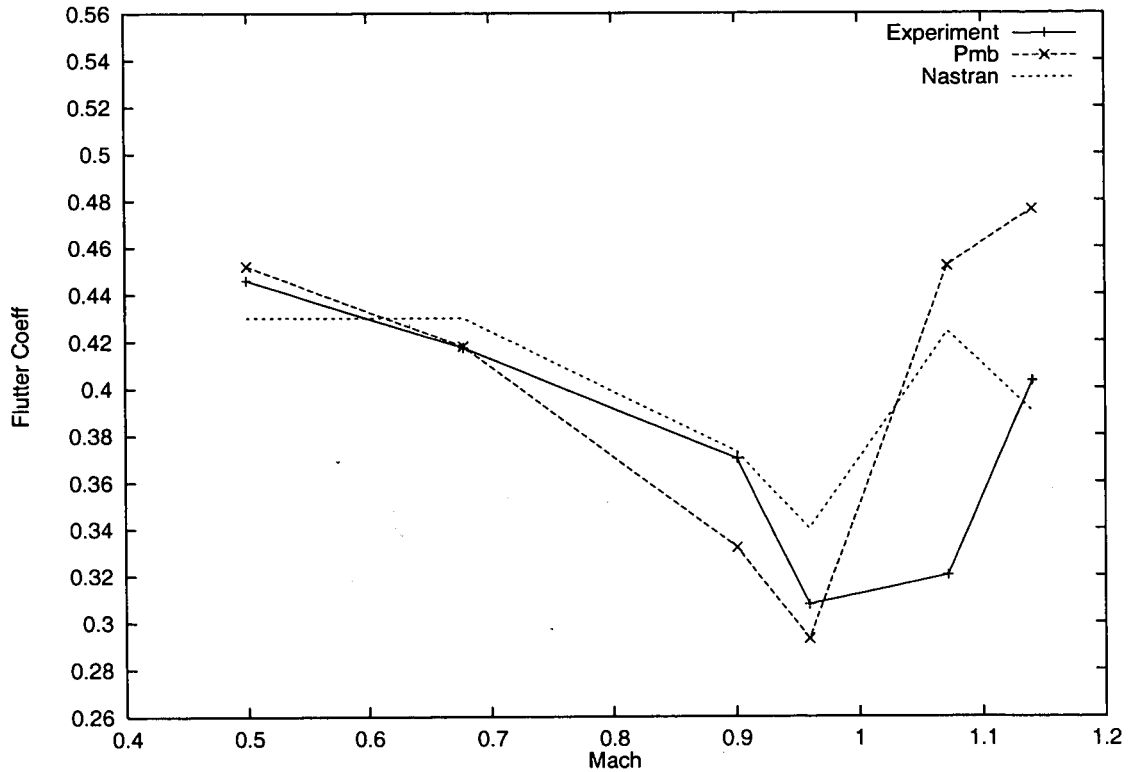


Figure 6.18: Comparison of predictions and measurements of 445.6 flutter boundary.

106 thousand. This grid, termed coarse, was derived from a fine grid by taking every second point. The tip is sharpened off to a line in one cell.

A steady calculation was computed for a freestream Mach number of 0.88 and an incidence of one degree. The comparison of the pressure distributions on the coarse and fine grids at 20, 40, 60 and 80 % span are shown in figures 6.20. There is good agreement between the two solutions, with the main feature being the shock wave which is close to the trailing edge. The coarse solution required 45 minutes and the fine solution 190 minutes to converge six orders on a 750 MhZ processor.

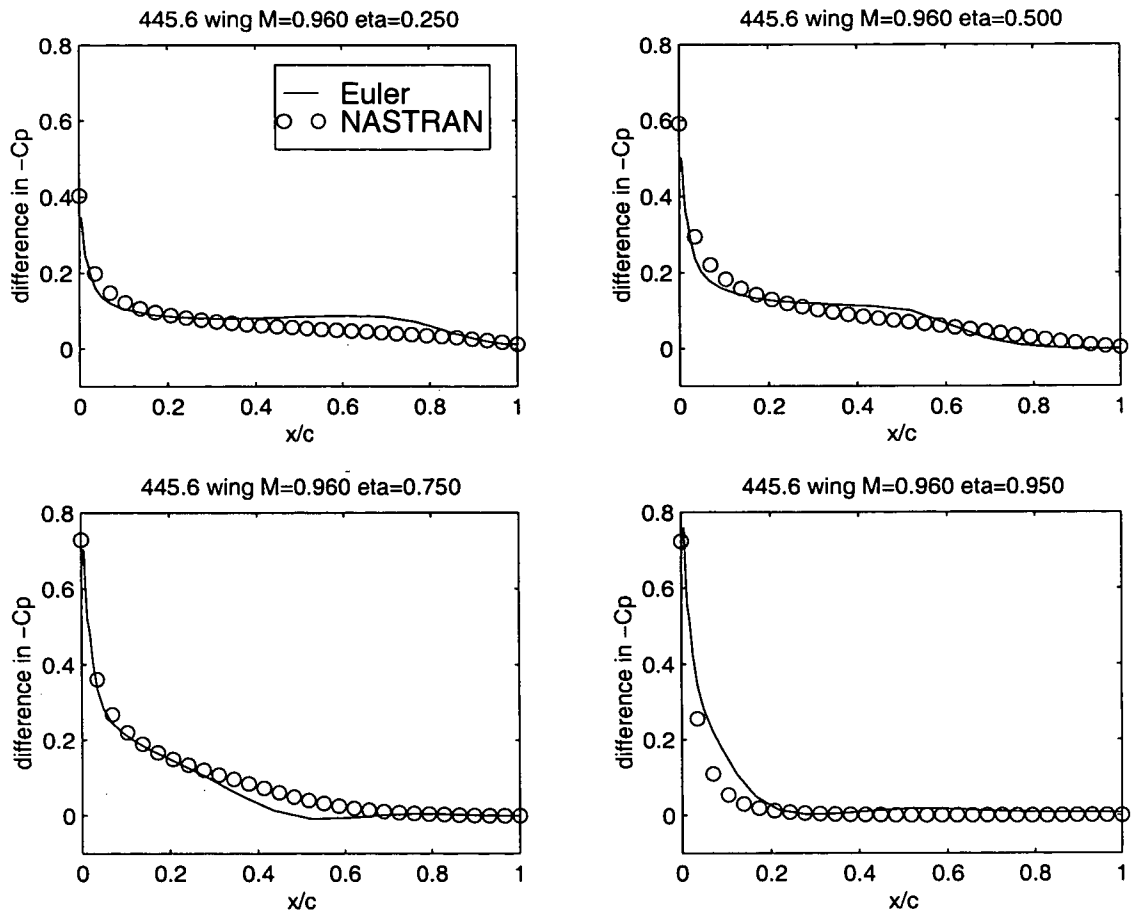


Figure 6.19: Comparison of pressure coefficient difference for flow around the rigid 445.6 wing at $M_\infty = 0.96$ and $\alpha = 1.0^\circ$ computed from the Euler and potential models.

6.4.2 Interpolated Mode Shapes

The main geometrical differences between the MDO and AGARD wings are first that the structural model for the MDO wing is only defined on part of the planform and secondly that the section for the MDO wing is thicker. To test the influence of a reduced plate on the recovered aerodynamic profile and the subsequent aeroelastic response some experiments were first carried out with the 445.6 wing. A cut down version of the structural model was prepared by removing layers at the leading and

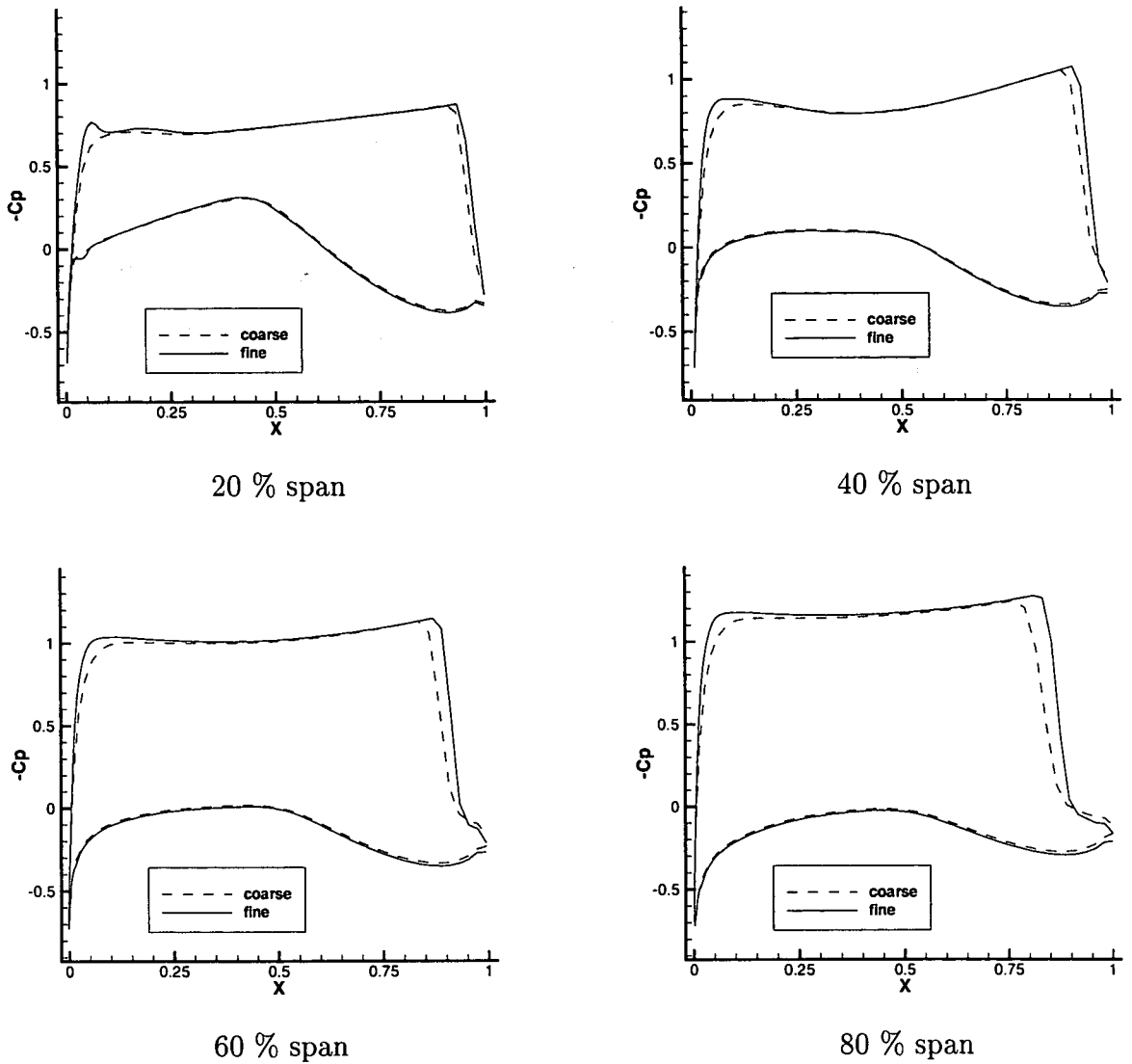


Figure 6.20: Comparison of pressure coefficient at 20, 40, 60 and 80 % span for the MDO wing with $M_\infty = 0.88$ and $\alpha = 1^\circ$. The lines are the coarse grid result and the symbols the fine grid result.

trailing edge to make the mismatch between the structural and aerodynamic planforms resemble the MDO wing. The results of this study were shown in section 6.3.2 above and it was concluded that linear in-plane transformation gives a good representation of the transformed mode shapes on the reduced model whereas the IPS method introduces additional (and spurious) camber to the torsion modes. It is expected that this will be the case for the MDO wing also due to the extent of the structural plate.

Secondly, the shape of the transformed mode 5, which is a torsion mode, is considered at 75 % of the span. The structural solution is given a large modal coordinate for the fifth mode and then the shape is transformed onto the fluid grid, as shown in figure 6.21. First, it is seen that using the constant CVT method for the out-of-plane treatment leads to a fattening of the section, as seen for the 445.6 wing. Also, the CVT-IPS result has an additional twist at the trailing edge comparing green for linear in-plane with blue for IPS in-plane). Since the trailing edges of the aerodynamic and structural planforms are much further apart than the leading edges it is consistent that the discrepancy should be largest at the trailing edge. This conclusion also holds when the stick out-of-plane treatment is used (comparing cyan for IPS in-plane with purple for linear in-plane). Using an incremental application of the modal coordinate and updating the CVT spline matrix at each step leads to a good preservation of the original aerodynamic profile. The stick out-of-plane treatment leads to a slightly different profile around mid-chord and also shortens the chord by about 2 %. Hence, the out-of-plane treatment makes a more significant difference for this case than for the 445.6 wing. This is explained by the thicker profile. However, it is noted that the applied motion for the case shown is extreme and that for cases with a smaller disturbance the differences between stick and regenerated CVT out-of-plane treatment are likely to be small.

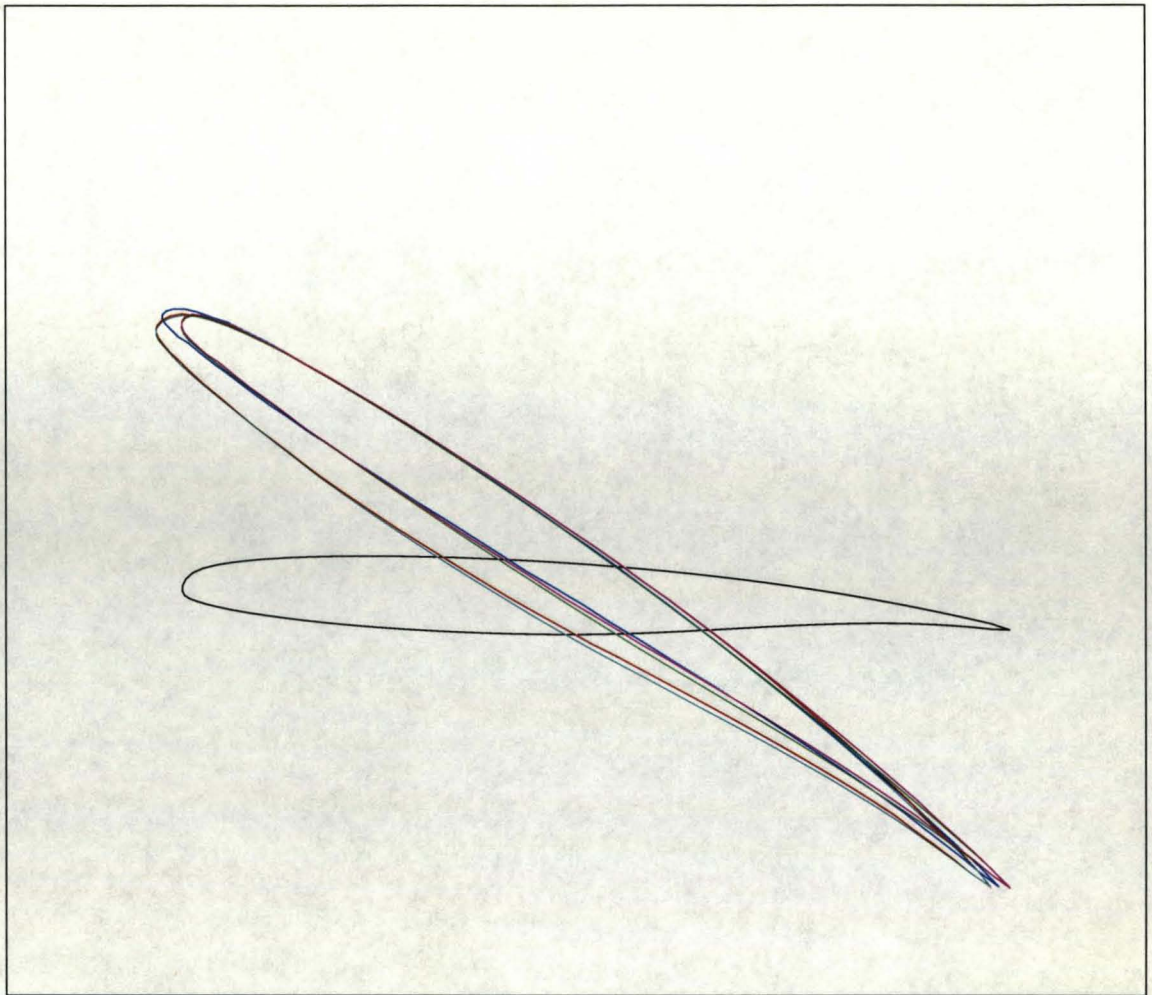


Figure 6.21: Comparison of transformed mode 5 for MDO wing.

6.4.3 Static Cases

We first present static results for the three test cases. The first task is to calculate the angle of attack for which the target lift coefficient is attained. This was done by calculating the lift coefficient for two values of the angle of attack and estimating the required value through a linear approximation. A calculation was then made at this angle of attack to check that the correct lift coefficient is in fact obtained. The trimmed conditions and corresponding lift coefficients are given in table 6.7.

	Case 1		Case 2		Case 3	
	α	C_L	α	C_L	α	C_L
Target		0.1187		0.0845		0.0437
regenerated CVT	1.094	0.1188	0.589	0.0844	-0.313	0.0437
constant CVT	1.070	0.1188	0.514	0.0845	-0.424	0.0437
constant CVT - IPS	1.642	0.1120	0.938	0.0843	-0.187	
IPS	1.987	0.1273	0.970	0.0843	-0.135	0.0437
linear	1.074	0.1188	0.539	0.0844	0.3743	0.0437

Table 6.7: Trimmed conditions for MDO wing. Note that the lift coefficient is based on an area given by the root chord squared and the angle of attack α is given in degrees.

The results are compared in terms of the leading and trailing edge deflections and the profiles adjacent to the tip which are shown in figures 6.22 to 6.24. The results calculated by Saab using the EURANUS code are included for comparison.

The results group around the in-plane treatment. When IPS is used the deflections and twist tend to be larger. This could be explained by the additional camber introduced by the extrapolated part of the aerodynamic profile as discussed above. The influence tends to be greater at the trailing edge than the leading edge, consistent with this interpretation since the extrapolation is over a greater distance for the trailing rather than the leading edge for the MDO wing. The linear in-plane results are all very similar, indicating that the influence of the out-of-plane treatment is relatively small for these cases. In addition, all of the results agree reasonably with the Saab results, which in turn fall within the scatter of the UNSI results.

The calculations for cases 1,2 and 3 using linear transformation require 74, 196 and 236 CPU minutes respectively on an Athlon 750 MHz processor. These calculations drive the residual for the initial rigid and subsequent aerostatic phases down six orders of magnitude, which might not represent the optimal strategy. The convergence

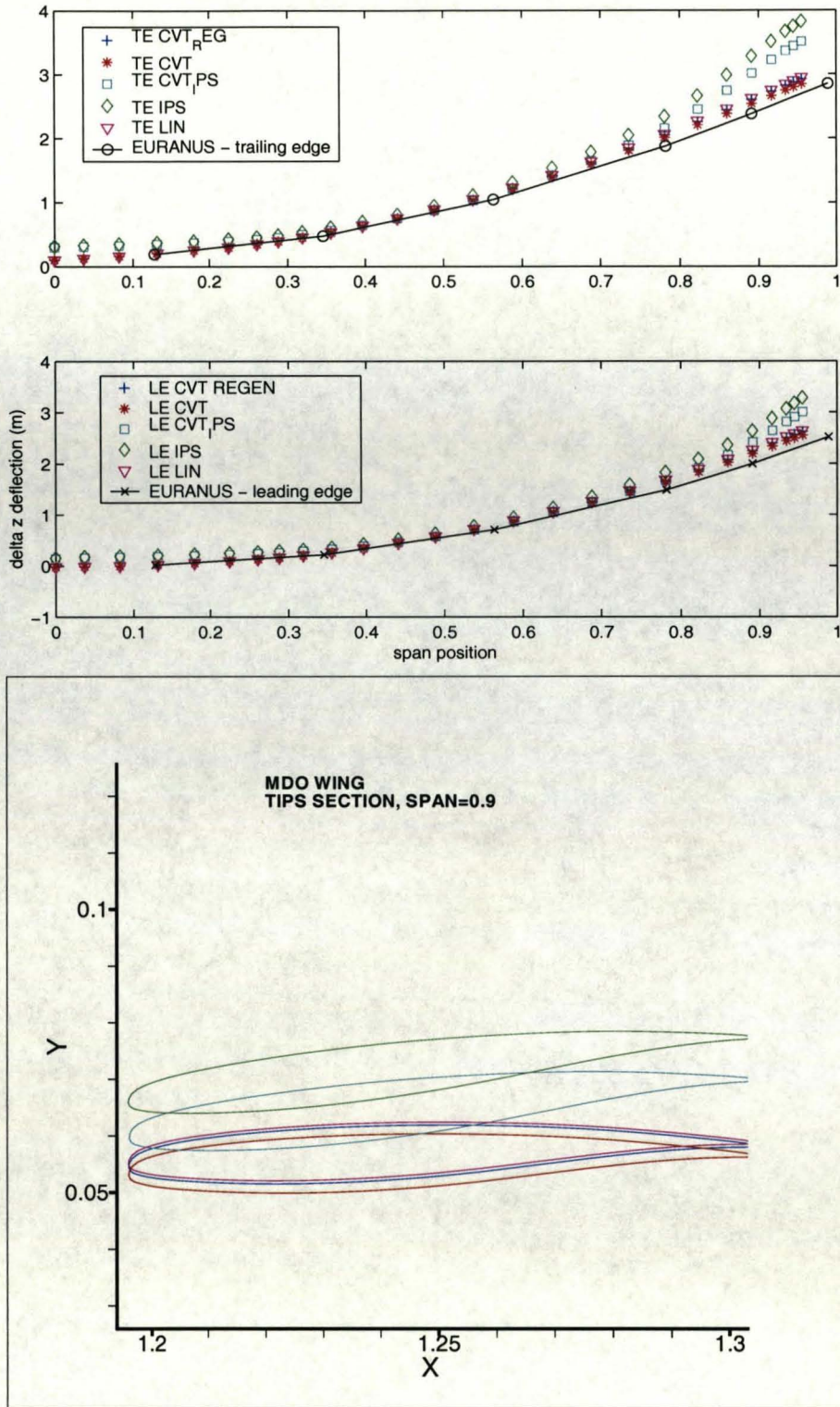


Figure 6.22: Aerostatic comparisons for case 1 for trimmed conditions.

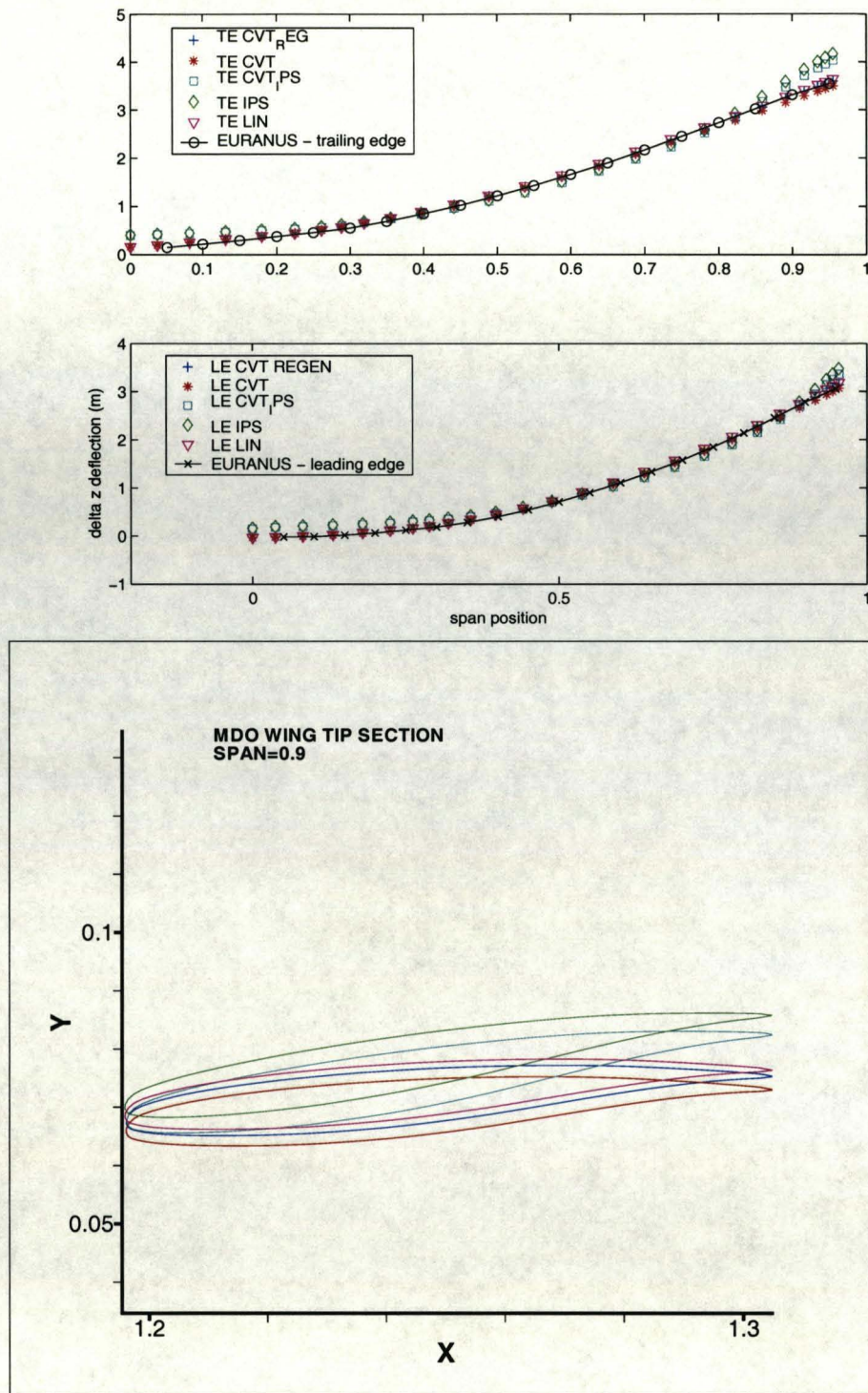


Figure 6.23: Aerostatic comparisons for case 2 for trimmed conditions.

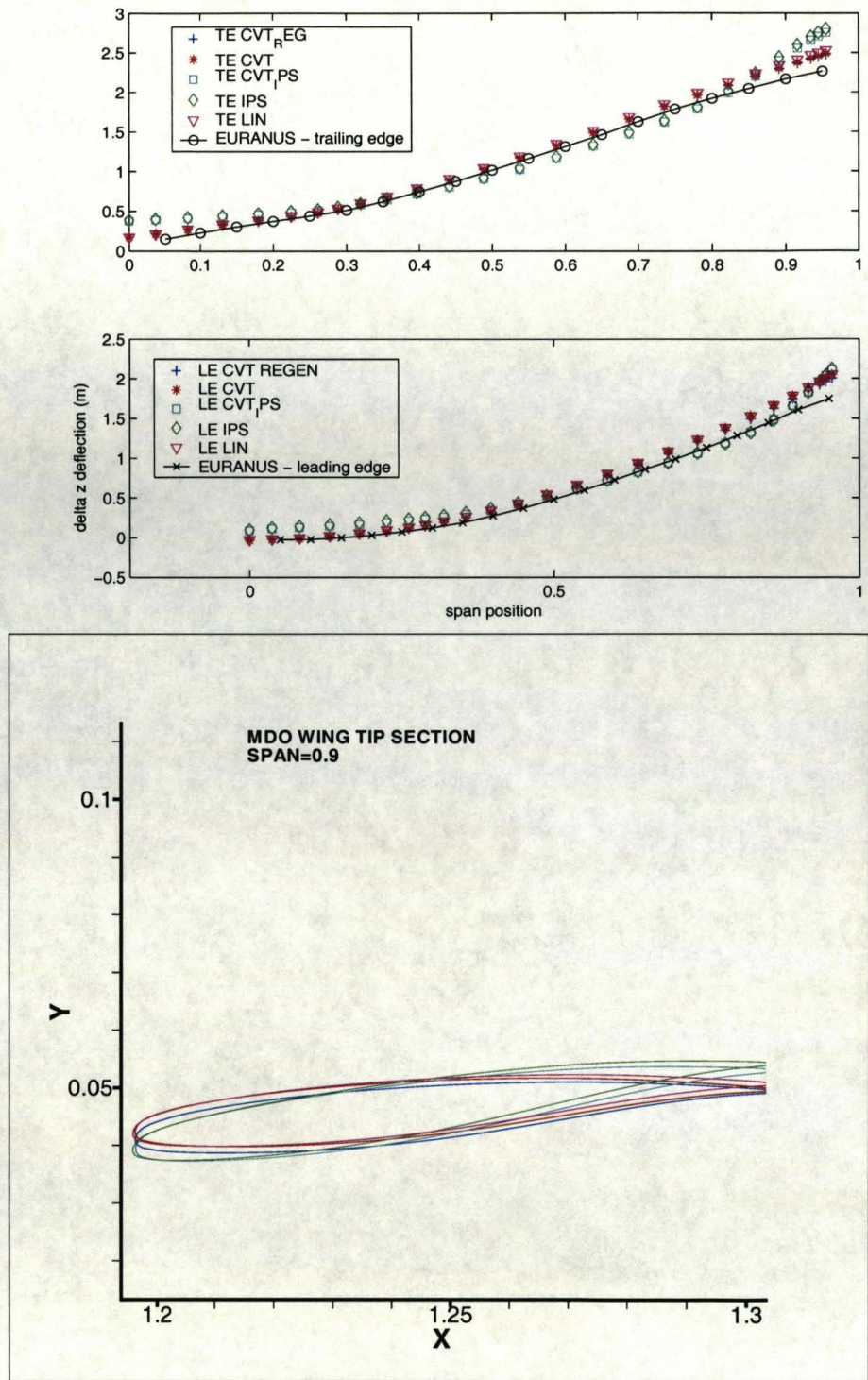


Figure 6.24: Aerostatic comparisons for case 3 for trimmed conditions.

history for case 1 is shown in figure 6.25. The convergence behaviour using the other methods is similar.

6.4.4 Dynamic Cases

We first show that the numerical parameters used for the time marching calculations give reasonably accurate solutions. This is tested for case 3 using linear transformation. The other transformation methods behave in a similar fashion. The two issues tested are the suitability of the time step (0.01) and the pseudo time tolerance (0.001). The comparison of the modal time histories when these values are reduced by half is shown in figures 6.26 and it is clear that the traces are identical. Hence the quoted values give an accurate solution. Since the only detailed comparisons of interest here are method to method comparisons and since no experimental data is available to compare with, the cost of the mesh refinement tests was not felt to be justified and we rely on the mesh refinement test for the rigid case presented above to indicate that the flow solution is reasonable.

Time marching calculations have been carried out for cases 2 and 3. These were restarted from the converged static solution with an initial velocity given to the first mode, as described above. Case 2 is expected to be stable, so the initial disturbance is damped, whereas case 3 is a flutter case in the transonic range and so a limit cycle oscillation is expected.

Comparison of the time traces using regenerated CVT with the EURANUS results are given in figure 6.27 and show good qualitative and reasonable quantitative agreement for both cases. The results from UNSI [57] show quite a spread of damping and the Saab results lie within the range.

A comparison of the influence of the transformation method is shown in figure 6.28. Considerable differences are seen. First, the constant CVT results show increased

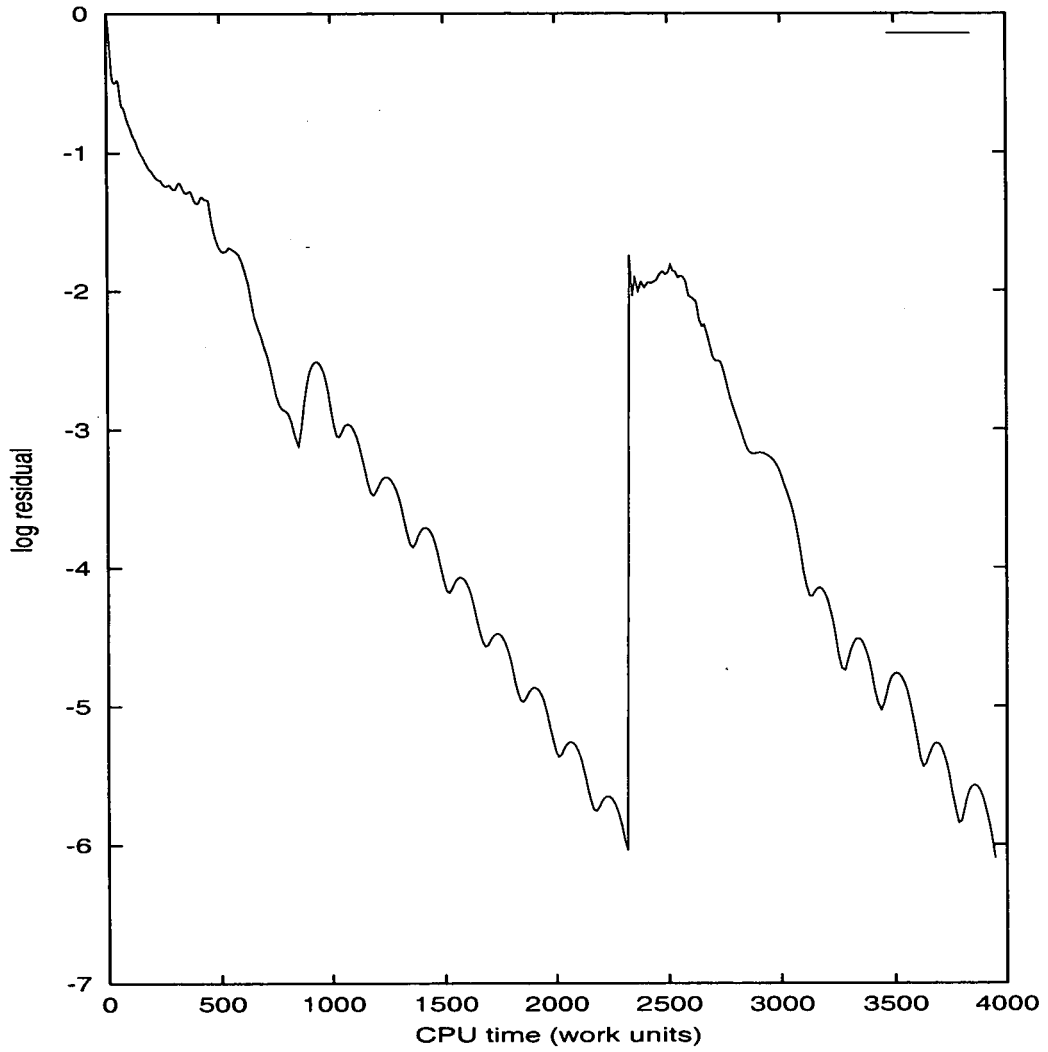


Figure 6.25: Convergence history for case 1 using linear transformation.

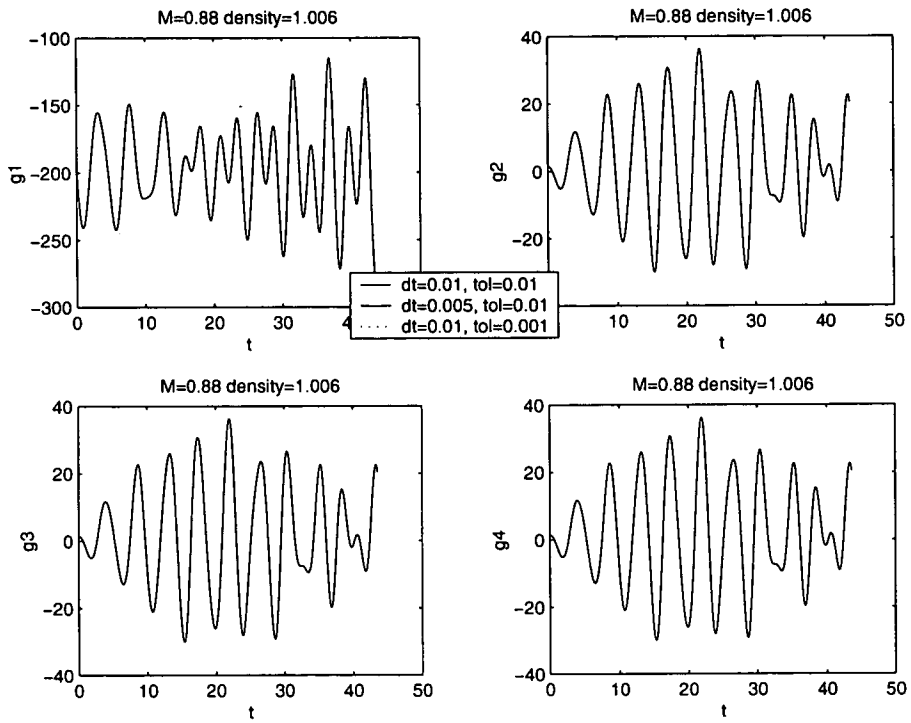


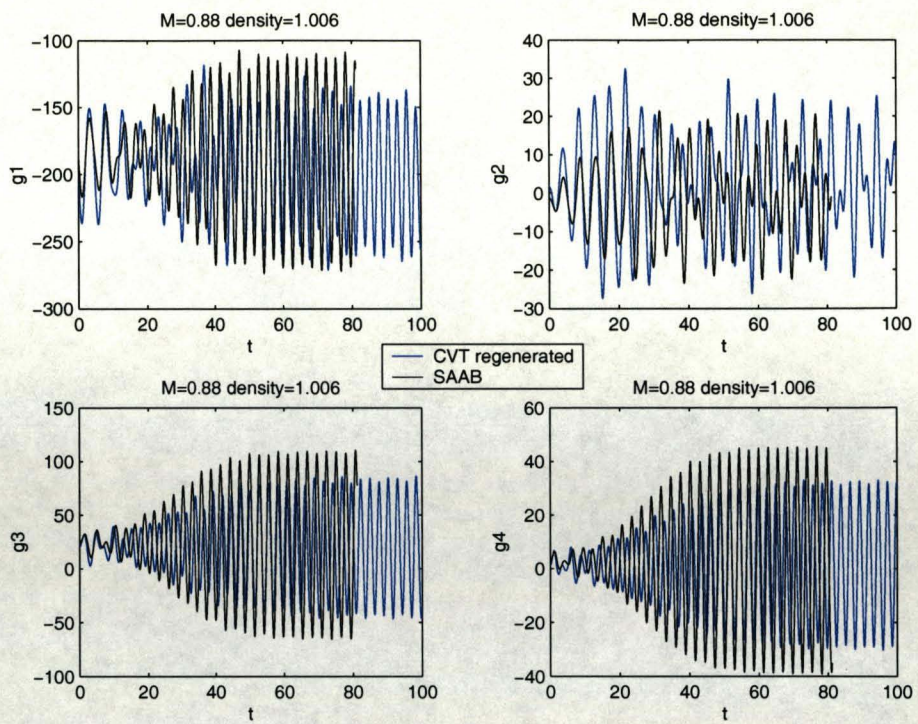
Figure 6.26: Comparisons of modal time histories for case 3 using linear transformation and various time stepping parameters.

damping, consistent with the behaviour for the 445.6 wing, leading to case 3 showing more of the features of a stable case. This is again ascribed to the fattening of the profile caused by the linearisation error incurred by the constant spline matrix.

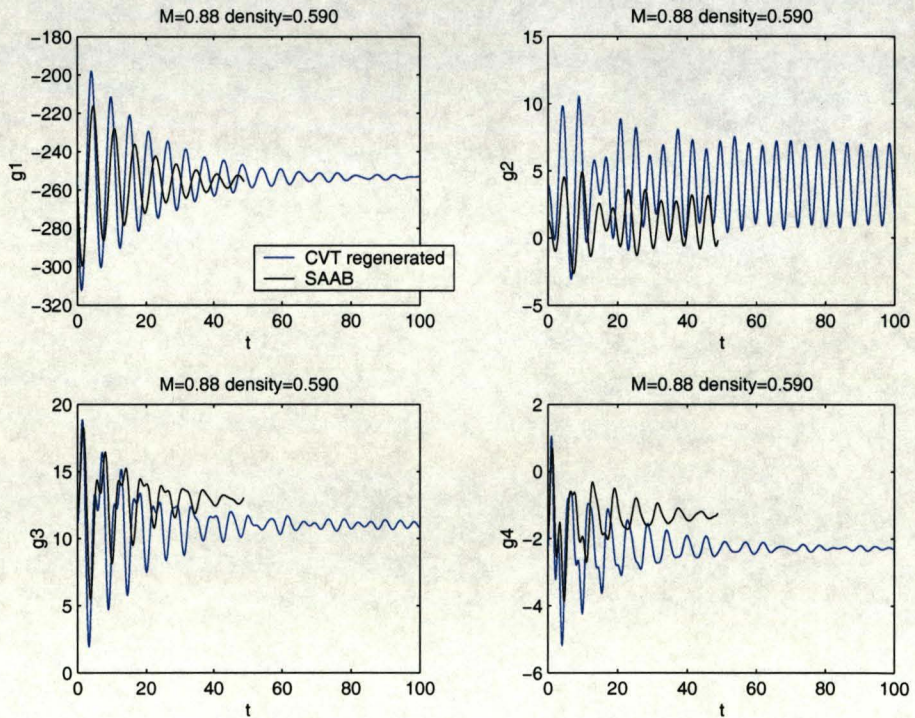
The remaining results group roughly around the in-plane treatment. Using IPS leads to a more energetic response. This is explained by the erroneous camber introduced by the transformation of torsion modes. To test this suggestion the reduced plate model was used to recompute a time response for the 445.6 wing at a Mach number of 0.96. All other details of the calculation and models were identical to those used for the full plate calculations. The comparison is shown in figure 6.29 and shows that the IPS result on the reduced plate is much more energetic than the linear result on the reduced plate, and that both are more energetic than the linear and IPS results using the full plate.

Finally, the regenerated CVT results are slightly less energetic than the linear results (i.e we are comparing the influence of the CVT and stick out-of-plane treatment here), but are close. This suggests that the in-plane treatment is more significant for the MDO test case due to the reduced planform for the structural model.

The CPU time used for these calculations was higher than for the relatively simple 445.6 wing. On average around 8-10 pseudo steps per real time step are required when 40 reduced time units have been calculated. This holds for for cases 2 and 3. For case 3, with the increasingly amplitude of the motion the number of pseudo time steps is increasing however. To time 40 the calculation takes about 92 CPU hours on an Athlon 750 MHz processor for both cases.



Case 3:altitude 2km



Case 2:altitude 7km

Figure 6.27: Comparisons of modal time histories for cases 2 and 3 using regenerated CVT and EURANUS results.

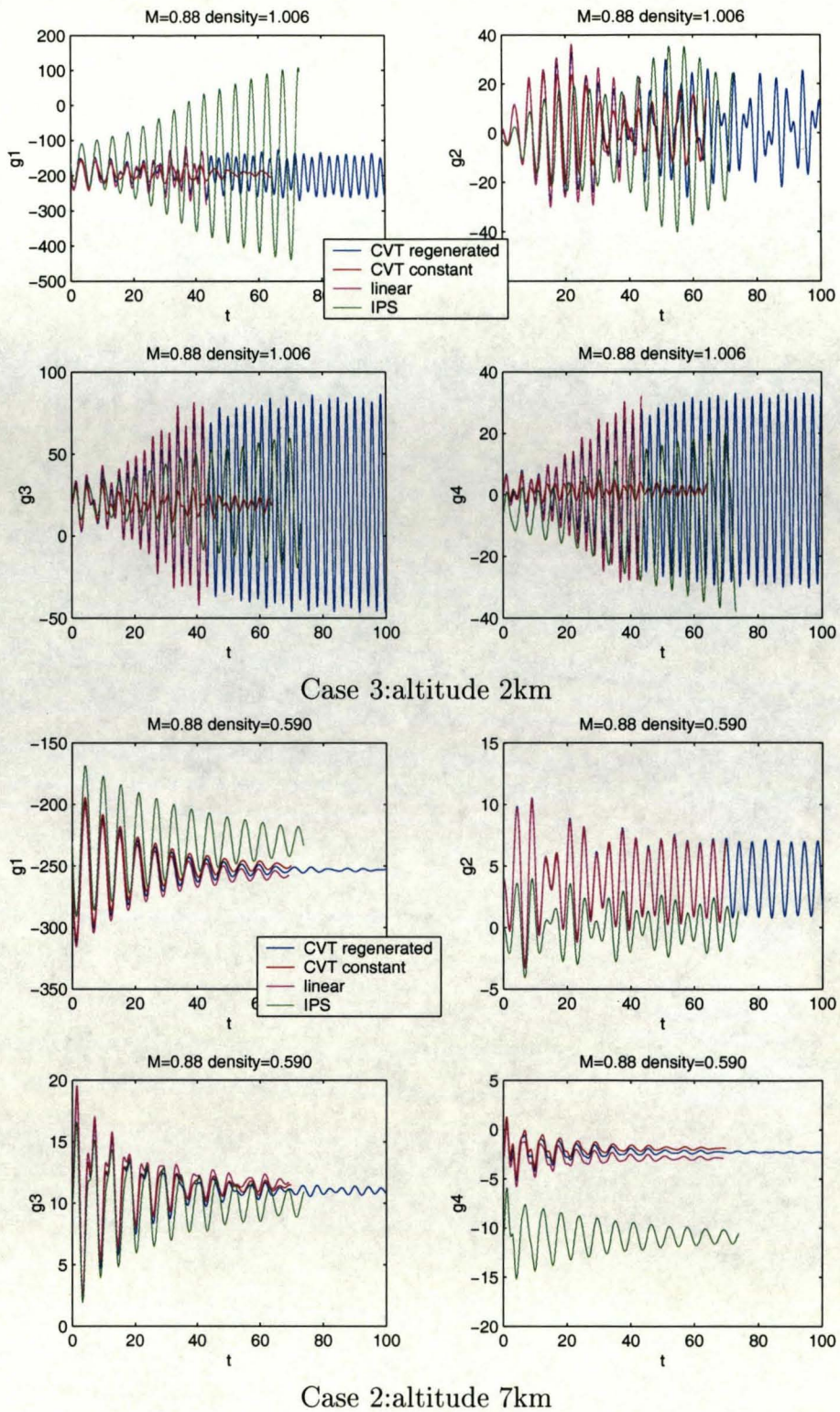


Figure 6.28: Comparisons of modal time histories for cases 2 and 3 using different transformation methods.

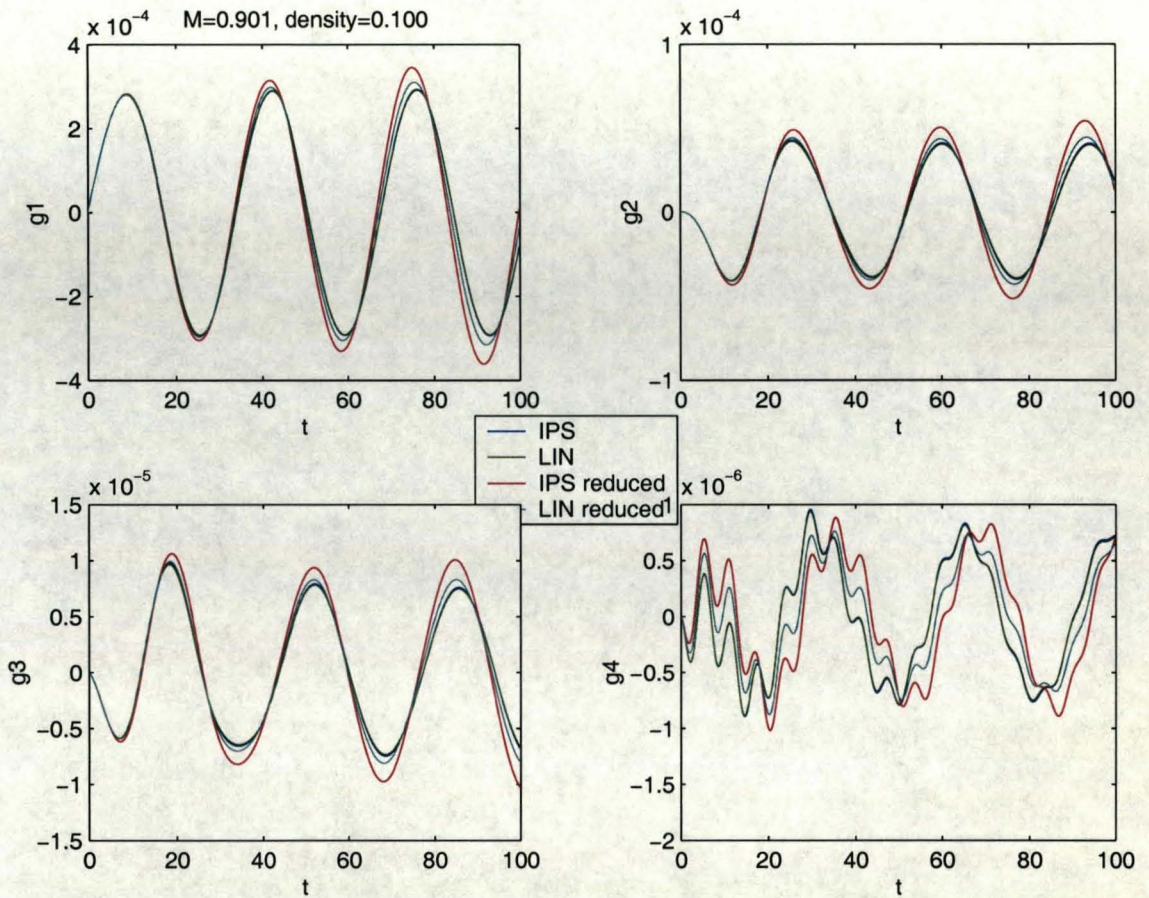


Figure 6.29: Comparisons of modal time histories for 445.6 wing at $M=0.901$, $\rho = 0.1 \text{ kg/m}^3$, using a full and reduced plate structural model. Note that the standard colour coding has not been used in this figure.

6.5 Conclusions

The results of this section have shown that the simulation of aeroelastic responses of simple wing geometries can be influenced by the transformation method used to couple the fluid and structural grids. Specifically the following conclusions can be drawn

- The efficiency of the simulations are comparable with the best published
- The constant CVT transformation thickens the profile and introduces excessive spurious damping
- This problem can be overcome by updating the CVT matrix during the calculation, an operation which is computationally cheap due to the compact form of the CVT method
- There is little difference seen between the regenerated CVT and stick out-of-plane treatment for these cases due to the fact that the wing is thin and is only ever rotated through small angles
- A significant influence of the in-plane treatment is seen when the planform of the fluid and structural models do not coincide and the aerodynamic profile must be extrapolated from the structural model. In this case the IPS method introduces an unwanted camber while the linear treatment preserves the mode shape beyond the extent of the structural model.
- The IPS method produces too energetic a response when a reduced planform structural model is used.

For the current test cases no significant advantage was seen by using the regenerated CVT transformation. However, when moving to a complete aircraft analysis

there are two components which might require the improved properties of the CVT method. A cylindrical fuselage which is modelled by a stick has a much greater out-of-plane component and hence will suffer from increased distortion due to the stick treatment. Secondly, motions of control surfaces through higher angles might introduce more out-of-plane distortion. The test cases presented in the current chapter are a necessary first step to investigate these issues on complete aircraft test cases. The properties of the CVT method will be valuable when attempting these more complex problems. The problems introduced by the IPS in-plane treatment were unexpected and illustrate how much care must be taken with aeroelastic simulations.

Chapter 7 : Conclusion

7.1 Objectives

This work started with the aim of setting up an aeroelastic (static and dynamic) solver based on the Euler solver pmb. The resulting aeroelastic solver would be able to tackle fluid-structure interaction for elastic aircraft wings without the limitations of a linear aerodynamic model in the transonic regime. The solver had to be evaluated by considering the different issues linked to such a problem, and in particular the influence of the transfer of information between the fluid and structural grids.

All of these objectives have been met. The aeroelastic code has been developed and tested for two wing test problems. The influence of time and spatial coupling has been evaluated. Reliable results for the MDO wing test case have been presented. The efficiency of the code has been compared with other published results and is competitive with the best available.

7.2 Lessons Learned

Two major errors can be introduced whilst coupling the fluid and structural codes. The first one is linked with the time sequencing of the codes. The use of the pseudo time method for iterating between the two solutions gives a simple way of removing sequencing errors. This was tested for an aerofoil case featuring significant aerodynamic induced nonlinearity. The result in accord with other published experience, is that the strong coupling in real time produces some benefits in terms of the computational cost required for a given accuracy. These benefits are much less than an order of magnitude however, but are still worth having.

The second issue, of major concern for doing three dimensional simulations, is how to transfer information between the fluid and structural grids. This problem is enhanced by the simplifications used during structural modelling, which lead to the fluid and structural surface grids not even being defined on the same surface. It was shown that previous methods, developed for linear aerodynamics, introduce distortions to the aerodynamic profile due to the way that this offset is handled.

The framework used for tackling the problem is essentially to consider the displacements in the plane of the structural model and the component out of the plane. A new method for treating the out-of-plane component, based on the idea of rotating and rescaling the component, was proposed and called the constant volume tetrahedron transformation. The method, when combined with linear in-plane interpolation, is simple to calculate and store. A linearised version was suggested for application.

It was suggested that a suitable test of transformation methods is to examine their ability to reproduce on the fluid grid applied translations and rotations on the structural grid. Some analysis showed that the linear CVT transformation satisfies this criteria to first order in the rotation angle. The application to wing test cases

showed that the effect of the linearisation error was to fatten the profile. This can be rectified simply by updating the transformation matrix regularly so that only small increments in the structural model are treated at any one time. In practice this means updating the relation at each real time step at minimal cost.

The coupled code was tested on two wing test cases. The first, the AGARD 445.6 wing, showed that the results were reliable, except when using the linearised and constant out-of-plane CVT treatment. The predicted flutter boundaries agree well with experimental data and the efficiency of the simulations is comparable with the best published results. The second case, the MDO wing, showed up an interesting influence of the in-plane treatment. Since the structural and fluid planforms are different, the displacements for the nose and trailing edge have to be extrapolated from the structural grid. Using IPS causes a spurious camber to be introduced which increases both the static and dynamic response of the wing. Linear in-plane treatment was found to preserve the aerodynamic profile better.

Finally, the BEM was considered both as a direct structural solver and as an interpolation method. It was hoped that a BEM solution defined on the fluid surface mesh would provide a way of avoiding the transformation problem. However, the results obtained with the simple BEM method used in this study were not encouraging and to model complex wing structures would require using a more complex formulation which was outside the scope of this work. The BEM based interpolation was not considered to present significant benefits over other available methods, including CVT, for geometrical test problems, and was hence not pursued into three dimensions for the final stages of the work.

7.3 Future Work

The work of this thesis can be taken forward in a number of exciting directions. First, the time marching aeroelastic code opens up opportunities for starting to evaluate nonlinear aeroelastic effects which were partly discussed in the introduction. The challenge of using the code to explain physical mechanisms for some of these problems is worthwhile and exciting.

For this to be realised the treatment of complex geometries must be addressed. The main unsolved problem is to set up the inter-grid transformation so that different components in the structural grid drive the right components in the fluid grid without holes or distortions being introduced at interfaces.

Thirdly, the work of this thesis has established test cases and transformation relationships for another PhD project within the CFD Group which is aimed at using Hopf bifurcation methodology to calculate flutter points from direct steady state calculations.

One limiting factor for future extensions is the lack of experimental data available for validation. A new dataset has been generated at NASA Langley Research Centre and is called MAVRICK. Its release for general use could allow increased confidence to be built up in aeroelastic simulations. In addition, access to flight test data is considered crucial for establishing simulations like the one developed in this thesis as a serious tool in design and certification.

Appendix A : Summary of BEM Theory

A.1 Summary of the Weighted residual method

We explain here briefly the weighted residual idea. The description follows that given in reference [38]. Assume that the equation to be solved on the domain Γ is $\mathcal{B}(\mathbf{u}) = \mathbf{0}$ with the condition on the boundary $\Gamma_1 : \mathbf{u} = \bar{\mathbf{u}}$ and $\Gamma_2 : \mathbf{p} = \bar{\mathbf{p}}$.

The method consists of finding an approximation to \mathbf{u} and \mathbf{p} by \mathbf{u}_{approx} and \mathbf{p}_{approx} . The error of the system $\boldsymbol{\varepsilon}$ is defined from

$$\mathcal{B}(\mathbf{u}_{approx}) = \boldsymbol{\varepsilon} \quad (1.1)$$

and on Γ_1

$$\mathbf{u} - \mathbf{u}_{approx} = \boldsymbol{\varepsilon}_1 \quad (1.2)$$

and on Γ_2

$$\mathbf{p} - \mathbf{p}_{approx} = \boldsymbol{\varepsilon}_2. \quad (1.3)$$

A weighting function \mathbf{w}_b is used to spread the error through the domain as

$$\int_{\Gamma} \boldsymbol{\varepsilon} \mathbf{w}_b^T d\Gamma = \int_{\Gamma_2} \boldsymbol{\varepsilon}_2 \mathbf{w}_b^T d\Gamma - \int_{\Gamma_1} \boldsymbol{\varepsilon}_1 \frac{\partial \mathbf{w}_b^T}{\partial n} d\Gamma \quad (1.4)$$

Using the functional expression of $\boldsymbol{\varepsilon}$ given above, integrating twice by parts, and taking into account the boundary conditions, the possibility of working only on the boundary arises if the weighting function \mathbf{w}_b is chosen to be solution of the problem $\mathcal{B}(\mathbf{w}_b) = \mathbf{0}$ on Γ .

A.2 Boundary integral from weighted residual statement

The first integral term in equation(3.4) can be rewritten as

$$\int_{\Gamma} \sigma_{ij,j} u_i^* d\Gamma = \int_{\Gamma} (\sigma_{ij} u_i^*)_{,j} d\Gamma - \int_{\Gamma} \sigma_{ij} \epsilon_{ij}^* d\Gamma. \quad (1.5)$$

From the divergence theorem

$$\int_{\Gamma} (\sigma_{ij} u_i^*)_{,j} d\Gamma = \int_{\Gamma} \sigma_{ij} n_j u_i^* d\Gamma = \int_{\Gamma} p_i u_i^* d\Gamma \quad (1.6)$$

Thus equation (3.4) becomes after integration by parts

$$-\int_{\Gamma} \sigma_{kj} \epsilon_{kj}^* d\Gamma + \int_{\Gamma} b_k u_k^* d\Gamma = -\int_{\Gamma_2} \bar{p}_k u_k^* d\Gamma - \int_{\Gamma_1} p_k u_k^* d\Gamma - \int_{\Gamma_1} (u_k - \bar{u}_k) p_k^* d\Gamma \quad (1.7)$$

The reciprocity principle

$$\int_{\Gamma} \sigma_{kj} \epsilon_{kj}^* d\Gamma = \int_{\Gamma} \sigma_{kj}^* \epsilon_{kj} d\Gamma \quad (1.8)$$

results from the manipulation of

$$\int_{\Gamma} \sigma_{kj} \epsilon_{kj}^* d\Gamma = \int_{\Gamma} [\lambda \delta_{ij} \epsilon_{ij}^* \epsilon_{kk} + 2\mu \epsilon_{ij} \epsilon_{ij}^*] d\Gamma \quad (1.9)$$

since $\delta_{ij} \epsilon_{ij}^* = \epsilon_{nn}^*$, $\epsilon_{kk} = \delta_{ij} \epsilon_{ij}$ and the strain-displacement relationship and the constitutive equation apply for both the approximating and weighting fields. Here λ and μ are the Lamé constants of the material.

Integrating equation(3.4) by parts again, one obtains

$$\int_{\Gamma} \sigma_{kj,j}^* u_k d\Gamma + \int_{\Gamma} b_k u_k^* d\Gamma = -\int_{\Gamma_2} \bar{p}_k u_k^* d\Gamma - \int_{\Gamma_1} p_k u_k^* d\Gamma - \int_{\Gamma_2} u_k p_k^* d\Gamma + \int_{\Gamma_1} \bar{u}_k p_k^* d\Gamma \quad (1.10)$$

A.3 Fundamental Solutions

We need the solution of the elastic problem with the same material properties as the body under consideration but corresponding to an infinite domain loaded with

	2D	3D
u_{ik}^*	$\frac{1}{8\pi G(1-\nu)} [(3-4\nu)ln(\frac{1}{r})\delta_{lk} + r_{,l}r_{,k}]$	$\frac{1}{16\pi G(1-\nu)} (\frac{3-4\nu}{r}\delta_{lk} + r_{,l}r_{,k})$
p_{ik}^*	$\frac{-1}{4\pi(1-\nu)r} (\frac{\delta r}{\delta n} [(1-2\nu)\delta_{lk} + 2r_{,l}r_{,k}] - (1-2\nu)(n_{l}r_{,k} - n_{k}r_{,l}))$	$\frac{-1}{8\pi(1-\nu)r^2} (\frac{\delta r}{\delta n} [(1-2\nu)\delta_{lk} + 5r_{,l}r_{,k}] + (1-2\nu)(n_{k}r_{,l} - n_{l}r_{,k}))$

Table A.1: Fundamental solutions of elasticity.

a concentrated unit point load. This is the fundamental solution of elastostaticity. Using the equilibrium equation, and the stress-strain relationship, and the strain displacement equation, one gets the Navier equation:

$$\frac{1}{1-2\nu} u_{j,jl} + u_{l,jj} + \frac{1}{\mu} b_l = 0. \quad (1.11)$$

The fundamental solution is obtained when a unit force is applied at point i in the direction of the unit vector in the l direction.

The problem is then to find the stress solution of

$$\frac{\partial \sigma_{jk}^*}{\partial x_j} = 0 \quad (1.12)$$

For this one solves the system:

$$\frac{\partial \sigma_{kj}^*}{\partial x_j} + \delta_i^k = 0 \quad (1.13)$$

where a unit load at the point i acts in the k direction. If this function is found then p_{ik}^* and u_{ik}^* are the tractions and displacements in the k direction due to unit forces acting in the l direction.

The expressions of the fundamental solutions used in the equations(3.8) are given for two and three dimensions in table A.1. The 2D formula holds for plane strain .

Bibliography

- [1] Collar, A. R., *Aeroelasticity- Retrospect and Prospect*. The Journal of the Royal Aeronautical Society, Jan. 1959, Vol.63 , number 557, p.4.
- [2] Bendiksen, O.O., A new approach to computational aeroelasticity, 32nd AIAA Structures, Structural Dynamics, and Materials Conference, Baltimore, April 1991, 1712-1727.
- [3] Garrick, I. E., Reed W. H., *Historical Development of Aircraft Flutter* , J. Aircraft, Vol.18, 1981, p. 898-912.
- [4] Lanchester, F.W., *Torsional Vibrations of the Tail of an Aeroplane*, AEC R & M 276, Part2, 1911.
- [5] von Baumhauer, A. G. , and Koning, C. *On the Stability of Oscillations of an Airplane Wing*, International Air Congress, 1923, London; also NACA TM 223, 1923.
- [6] Theodorsen, T., *General Theory of Aerodynamic Instability and the Mechanism of Flutter*, NACA Rept. 496,1935.
- [7] Kaynes, I. W., *Aeroelasticity Review*, DERA/MSS/MSTR2/CR010456, Feb. 2001

- [8] Dreim, D.R., Jacobson, S.B., Britt, R.T., *Simulation of Non-Linear Transonic Aeroelastic Behavior on the B-2*, CEAS/AIAA/ICASE/NASA Langley International Forum on Aeroelasticity and Structural Dynamics, 1999, Williamsburg, Virginia.
- [9] Eussen, B. J. G., Hounjet, M. H. L., Meijer, J. J., Prananta, B. B. and Tjatra, I. W., *Perspectives of NLR Aeroelastic Methods to Predict Wing/Store Flutter and Dynamic Loads of Fighter-Type Aircraft*, NLR-TP-2000-447, p.13.
- [10] Kiebling, F., Rippl, *Aeroelastic Investigations on High Altitude Research Aircraft Strato 2C*, CEAS/AIAA/ICASE/NASA Langley International Forum on Aeroelasticity and Structural Dynamics, 1999, Williamsburg, Virginia.
- [11] Neisius, D., *The Importance of Geometric Modelling of Aeroelastically Oscillating Wings in Unsteady Transonic CFD Calculations*, International Forum on Aeroelasticity and Structural Dynamics, Proceedings of the Royal Aeronautical Society, June 1995, Manchester.
- [12] Goura, G.S.L., Badcock, K.J., Woodgate, M.A. and Richards, B.E., *Implicit Method for the Time Marching Analysis of Flutter*, Aeronautical Journal, volume 105, number 1046, April, 2001.
- [13] Goura, G.S.L., Badcock, K.J., Woodgate, M.A. and Richards, B.E., *A Data Exchange Method for Fluid-Structure Interaction Problems*, Aeronautical Journal, volume 105, number 1046, April, 2001.
- [14] Badcock, K.J., Henshaw, M., Chapman, R., *Summary of Aerodynamic Methods for Flutter Analysis* Report BAE-WAE-RP-GEN-001040, 20/03/00, Unclassified.

- [15] Badcock, K.J., Richards, B.E. and Woodgate, M.A., *Elements of Computational Fluid Dynamics on Block Structured Grids using Implicit Solvers*, Progress in Aerospace Sciences, vol 36, 2000, pp 351-392.
- [16] Osher, S. and Chakravarthy, S.R., *Upwind Schemes and Boundary Conditions with Applications to Euler equations in General Coordinates*, Journal Computational Physics, vol. 50, 1983, p 447-481.
- [17] Van Leer, B., *Towards the Ultimate Conservative Conservative Difference Scheme II: Monotonicity and Conservation Combined in a Second Order Scheme*, Journal Computational Physics, 14, 361-374, 1974.
- [18] Cantariti, F., Dubuc, L., Gribben, B., Woodgate, M., Badcock, K. and Richards, B., *Approximate Jacobians for the Solution of the Euler and Navier-Stokes Equations*, University of Glasgow, Aerospace Engineering report 9704, 1997.
- [19] Henderson, J., Badcock, K.J. and Richards, B.E., *Understanding subsonic and transonic open cavity flows*, Aeronautical Journal, February 2001, pp 77-84.
- [20] Feszty, D, Richards, B.E., Badcock, K.J. and Woodgate, M.A., *Numerical Simulation of pulsating flow arising over an axisymmetric spiked blunt body at Mach 2.21 and Mach 6.00*, Shock Waves Journal, Vol 10, Issue 5, 2000, pp 323-331.
- [21] Badcock, K.J., Cantariti, F., Hawkins, I., Woodgate, M., Dubuc, L. and Richards, B.E., *Simulation of Unsteady Turbulent Flows around Moving Aerofoils using the Pseudo time method*, Int J Num Meth in Fluids, 32, No 5, 2000, 585-604.

- [22] Badcock, K.J., Woodgate, M, Cantariti, F., Richards, B., *Solution of the Unsteady Euler Equations in Three Dimensions Using a Fully Unfactored Method*, AIAA Paper 2000-0919, 2000.
- [23] Gordon, W.J. and Hall, C.A., *Construction of curvilinear coordinate systems and applications to mesh generation*, Int J Num Meth Engr, 7, 1973, pp 461-477.
- [24] Tidjeman, H. and Van Nunen, J.W.G, *Results of Transonic Wind Tunnel Measurements on an Oscillating Wing with External Store(Data Report)*, Technical Report 78030, NLR, 1978.
- [25] Van Nunen, J.W.G. and Tidjeman, H., *Transonic Wind Tunnel Tests of an Oscillating Wing with External Store(Parts i-iv)*, Technical Report 78106, NLR, 1978.
- [26] Cantariti,F, Woodgate, M., Badcock, K.J. and Richards, B.E., *Solution of the Euler Equations in Three Dimensions Using a Fully Unfactored Method*, Aerospace Engineering Report 7, Glasgow University, Glasgow, UK, 1999.
- [27] Djayapertapa, L., *A Computational Method for Coupled Aerodynamic-Structural Calculations in Unsteady Transonic Flow with Active Control Study*, Thesis, University of Bristol, Nov. 2000.
- [28] Jameson, A., *Time dependent calculations using multigrid, with applications to unsteady flows past airfoils and wings*, Technical report, AIAA 91-1596, 1991.
- [29] Kousen, K.A. and Bendiksen, O.O. *Nonlinear Aspects of the Transonic Aeroelastic Stability Problem*, 29th Structures, Structural Dynamics and Materials Conference, AIAA, 1988.

- [30] Bendiksen, O.O, *A New Approach to Computational Aeroelasticity*, 32nd Structures, Structural Dynamics and Materials Conference, AIAA, 1991.
- [31] Cantariti, F., Dubuc, L., Gribben, B., Woodgate, M., Badcock, K.J. and Richards, B.E., *Approximate Jacobians for the Solution of the Euler and Navier-Stokes Equations*, Aerospace Engineering Report, 5, Glasgow University, Glasgow, UK, 1997.
- [32] Badcock, K.J., Sim, G. and Richards, B. E. *Aeroelastic Studies Using Transonic Flow CFD Modelling*, CEAS International Forum on Aeroelasticity and Structural Dynamics, Royal Aeronautical Society, 1995.
- [33] K.J.Badcock, G.S.L.Goura and B.E.Richards, *Investigation of Sequencing Effects on the Simulation of Fluid-Structure Interaction*, in High Performance Computing, editors R.J.Allan et al, Plenum Publishing Corp, pp 385-394, 1998.
- [34] G.S.L. Goura, K.J. Badcock, B. E. Richards, *Tools for sequencing effects in fluid-structure interaction*. CEAS/AIAA/ICASE/NASA Meeting on Aeroelasticity and Structural Dynamics. Norfolk, Va, USA, June 1999.
- [35] Niku, S.M., Brebbia, C., *Implicit Implementation of rigid body rotations to boundary element formulation*, Engineering Analysis, June 1988, vol.5 , No. 2., p.108-109, Technical note.
- [36] Brebbia, C.A., *The Boundary Element Method for Engineers*, Pentech press, London, 1978.
- [37] Brebbia, C.A., and Walker, S., *Boundary Element Techniques in Engineering*, Newnes-Butterworth, London, 1980.

- [38] Partridge, P.W., Brebbia, C.A. and Wrobel, L.C., *The dual reciprocity boundary element method*, International Series on Computational Engineering, Computational Mechanics, ISBN: 0945824823, February, 1992.
- [39] Gao, Xiao-Wei, *Non-linear and Multi-Region Boundary Element Stress Analysis*, PhD Thesis, Faculty of Engineering, University of Glasgow, March, 1999.
- [40] Jaswon, and Ponter, A.R., *An integral Equation Solution of the Torsion Problem*, Proc Roy Soc London, Series A, 275, 237-246, 1963.
- [41] Symm, G.T., *Integral Equation Methods in elasticity and potential theory*, PhD thesis, University of London, 1964.
- [42] Rizzo, F.J., *An integral approach to boundary value problems of classical elastostatics*, Quart Appl Math, 25, 83-95, 1967.
- [43] Cruse, T.A., *Numerical Solutions in three dimensional elastostatics*, Int J Solids and Structures, 5, 1259-1274, 1969.
- [44] Lachat, J.C., *A further development of the boundary integral technique for elastostatics*, PhD thesis, University of Southampton, 1975.
- [45] Schmitt, A.F., *A least squares matrix interpolation of flexibility influence coefficients*. Journal of the Aeronautical Sciences, Vol.23, October 1956, p.980.
- [46] Harder, R.L. and Desmarais, R.N., *Interpolation using surface spline*, Journal of Aircraft, Vol 9, No 2., February, 1972, pp 189-191.
- [47] Hardy, R. L., *Theory and applications of the multiquadric-biharmonic method*, Computers Math. Applic., Vol 19 , No 8/9, 1990, pp 163-208.

- [48] Smith, M. J., Hodges, D. H., Cesnik, C. E. S., *An evaluation of computational algorithms to interface between CFD and CSD methodologies*, Wright-Patterson Air Force report, WL-TR-96-3055, November 1995.
- [49] Smith, M. J., Hodges, D. H., Cesnik, C. E. S., *Evaluation of computational algorithms suitable for fluid-structure interaction*, Journal of Aircraft, vol.37, No2, pp 282-295, March-April 2000.
- [50] Guruswamy, G. P. and Byun, C., *Direct Coupling of the Euler Flow Equations with Plate Finite Element Structures*, AIAA J, Vol 33, No 2, Feb 1995.
- [51] Brown, S.A., *Displacement Extrapolation for CFD and CSM Analysis*, AIAA Paper 97-1090, April, 1997.
- [52] Cebal, J.R., and Lohner, R, *Fluid-Structure Coupling: Extensions and Improvements*, AIAA Paper 97-0858.
- [53] Chen,P.C.,and Jadic,I., *Interfacing of fluid and structural models via innovative Structural Boundary Element Method*, AIAA Journal , Vol 36, No2, pp 282-287,1998.
- [54] Chen,P.C.,and Hill, L. R., *A Thre-Dimensional Boundary Element Method for CFD/CSD Grid Interfacing*, AIAA paper A99-24610.
- [55] Lohner,R., Yang,C., Cebal,J., Baum,J.D., Luo,H., Pelessone,D. and Charman,C., *Fluid-Structure interaction using a loose coupling algorithm and adaptive unstructured grids.*, AIAA paper AIAA-95-2259, 1995.
- [56] Cebal,J., *Loose Coupling Algorithms for Fluid-Structure Interaction*, PhD thesis, George Mason University, 1996.

- [57] Girodroux-Lavigne, P., Grisval, J. P., Guillemot, S., Henshaw, M., Karlsson, A., Selmin, V., Smith, J., Teupootahiti, E. and Winzell, B., *Comparative study of advanced fluid-structure interaction methods in the case of a highly flexible wing (Results from the UNSI program)*, International Forum aeroelasticity structural dynamics, June 2001, Madrid.
- [58] Smith, J., Badcock, K., Goura, L. and Henshaw, M., *Analysis of Load Transfer Methods for Dynamic Aeroelastic Simulation*. Paper 023. International Forum on Aeroelasticity and Structural Dynamics 2001 Madrid (Spain) 5-7 June 2001.
- [59] Duchon, J., *Splines minimizing rotation-invariant semi-norms in sobolev spaces*, in Constructive Theory of Functions of Several Variables, Springer Germany, pp 85-100, 1976.
- [60] Ottosen, N. and Petersson, H., *Introduction to the Finite Element Method*, Prentice-Hall, p314, 1992.
- [61] Yates, E.C., *AGARD standard aeroelastic configurations for dynamic response I: Wing 445.6*, AGARD Report 765, 1988.
- [62] ZAERO Applications Manual, Version 3.2. Zona Technology, Arizona.
- [63] da Silva, R.G.A., de Faria Mello, O.A., *Prediction of Transonic Flutter Using Nastran with Aerodynamic coefficients Tuned to Navier Stokes Computations*, CEAS/AIAA/ICASE/NASA Meeting on Aeroelasticity and Structural Dynamics. Norfolk, Va, USA, June 1999.
- [64] Batina, J.T., Bennett, R.M., Seidel, D.A., Cunningham, H.J. and Bland, S., *Recent Advances in Transonic Computational Aeroelasticity*, Computers and Fluids, Vol 30, No 172, 1988, pp29-37.

- [65] Edwards, J.T., *Calculated viscous and scale effects on transonic aeroelasticity*, AGARD SMP meeting on Numerical Unsteady Aerodynamic and Aeroelastic Simulation, Aalborg, Denmark, October 1997. AGARD R-822.
- [66] Gupta, K.K., *Development of a Finite Element Aeroelastic Analysis Capability*, J Aircraft, Vol 33, No 5, 1996, pp 995-1002.
- [67] Melville, R.B., Morton, S.A., and Rizzetta, D.P., *Implementation of a fully-implicit, aeroelastic Navier-Stokes Solver*, AIAA, Computational Fluid Dynamics Conference, 13th, Snowmass Village, CO, June 29 -July 2, 1997. AIAA Paper 97-2039.
- [68] Rausch, R.D., Batina, J.T. and Yang, H.T., *Three-Dimensional Time-Marching Aeroelastic Analyses Using an Unstructured-Grid Euler Method*, AIAA Journal, vol. 31, No 9, pp 1626-1633, 1993.
- [69] Lesoinne, M. and Farhat, C., *High order subiteration-free staggered algorithm for nonlinear transient aeroelastic problems*, AIAA Journal, vol. 36, No 9, pp 1754-1757, 1998.
- [70] Kolonay, R. M., *Unsteady aeroelastic optimization in the transonic regime*, Ph.D. Dissertation, Purdue University, Dec. 1996.
- [71] MSC/NASTRAN Quick reference guide, version 70. The MacNeal-Schwendler Corporation, Los Angeles, California, 1997.

